Multiscale Simulation Studies of Interactions of Carbon Nanotubes with Biopolymers and Lipid Bilayer

by

Edita Sarukhanyan

A Thesis submitted in partial fulfillment
of the requirements for the degree of

Doctor of Philosophy
In Chemistry

Approved Thesis Committee:

Prof. Giuseppe Milano
Thesis Supervisor, University of Salerno, Italy

_____

Prof. Danilo Roccatano
Co-supervisor, Jacobs University Bremen

_____

Prof. Jürgen Fritz
Internal committee member, Jacobs University Bremen

_____

Prof. Veit Wagner
Internal committee member, Jacobs University Bremen

_____

Prof. Vincenzo Tucci
External committee member, University of Salerno, Italy

Date of Defense: **1st August, 2013**

School of Engineering and Science

ACKNOWLEDGEMENTS

The path of my Ph.D was one of the most challenging, demanding and at the same time full of wonderful experiences. It would not be possible to accomplish my dissertation without guidance and motivation from my supervisors, help from my friends, support and encouragement from my family.

Above all, I would like to express my sincere gratitude to both my supervisors **- Professor Giuseppe Milano** and **Professor Danilo Roccatano** for providing me a great opportunity to be the part of an amazing joint Ph.D program between the University of Salerno and Jacobs University Bremen. I am deeply grateful to **Prof**. **Giuseppe Milano** for scientific support, patience and trust. He has provided me a freedom to perform a research and never made a pressure. At the same time his continuous help, professional guidance and motivation helped me to accomplish the thesis. I will never forget his support and encouragement at my hard life-times. I am sincerely grateful to **Prof. Danilo Roccatano** for his kind and patient supervision, for sharing his immense knowledge and experience, for interesting scientific discussions and ideas. He has explained difficult concepts in easy manner to make it clear and understandable. He always extended a helping hand in the time of need. Indeed, I consider myself a lucky person to have such a great opportunity to work with high level professionals.

I would like to express my respectful gratitude to dissertation committee members – **Professor Jürgen Fritz**, **Professor Vincenzo Tucci** and **Professor Veit Wagner** for the revision of my PhD thesis, for their valuable comments and discussions.

I am deeply grateful to the MOLNAC research group at the University of Salerno:

Special thank I would like to express to my friend and colleague **Mr. Antonio De Nicola**. I am indebted to this person for his great help and support. Antonio helped me to learn how to handle with Linux, run commands of GROMACS to perform simulations, as well as, to accomplish one part of my thesis work. My heartfelt gratitude goes to **Dr. Anna Vangone** for her friendship. She is the one who had created for me friendly environment by organizing many events and invitations. Anna made me feel at home being away from home. I would like to thank my other

ACKNOWLEDGEMENTS

colleagues from the University of Salerno - **Dr. Andrea Correa, Dr. Francesco Ragone**, **Dr. Raffaele Credendino**, **Dr. Naimeh Bahri Laleh**, **Dr. Ying Zhao** and **Dr. Susana Figueroa** for their kind help and nice company.

I would like to thank **Prof. Luigi Cavallo** from the University of Salerno for covering the expenses for my summer school participation at Queen's University of Belfast in July 2010.

I am deeply grateful to my friends and colleagues from the research group at Jacobs University Bremen:

I warmly thank **Dr. Samira Hezaveh** for being supportive, helpful and a reliable person, as well as, **Dr. Susruta Samanta**, **Dr. Rajni Verma** and **Dr. Kadga Karki** for sharing their knowledge and experience.

I would like to acknowledge *"Borsa di Studio di Dottorato"* for the financial support.

I would like to thank **Dr. Achim Gelessus** from Jacobs University of Bremen for technical support and the computational resources at CLAMV, as well as, computational resources of Centro computazionale di RicErca sui Sistemi COmplessi (CRESCO) in Italy.

I am very grateful to **Sabine Meier** from Jacobs University for her technical assistance.

I would like to thank ***Bella Italia*** and ***sunny Salerno***, ***Wunderland Deutschland*** and ***friendly Bremen*** for hosting me. I am thankful to *College Nordmetall* at Jacobs University, especially, the College Masters and inhabitants of the graduate floor, where I am living, for the nice memories.

Finally, I would like to thank my parents, grandparents and my sister for their tremendous and unconditional love.

Edita Sarukhanyan

July, 2013

FUNDING

The joint Ph.D program between the University of Salerno and Jacobs University Bremen was carried out with the financial support from the **"Borsa di Studio di Dottorato" (University of Salerno)** for the project titled *"Multiscale Simulation Studies of Interactions of Carbon Nanotubes with Biopolymers and Lipid Bilayer"*.

LIST OF PUBLICATIONS

1. ***Edita Sarukhanyan****, Antonio De Nicola, Danilo Roccatano, Toshihiro Kawakatsu, Giuseppe Milano.* Spontaneous Insertion of Carbon Nanotube Bundles inside Biomembranes: A Hybrid Particle-Field Coarse-Grained Molecular Dynamics. **(manuscript under preparation)**

2. ***Edita Sarukhanyan****, Giuseppe Milano, Danilo Roccatano*. Atomistic Simulations of Cecropin A – Magainin 2 Hybrid Peptide in Water Solutions. **(manuscript under preparation)**

LIST OF CONFERENCES AND PRESENTATIONS

1. **Edita Sarukhanyan**, Giuseppe Milano and Danilo Roccatano, *"Atomistic Simulations of Carbon Nanotubes in Aqueous Mixtures of Surfactants",* Poster Presentation, Molecular Life (MOLIFE) Center Jacobs University Bremen, **Bad Bavensen, Germany**, *March 2013*

2. **Edita Sarukhanyan**, Giuseppe Milano and Danilo Roccatano, *"Atomistic Simulations of Carbon Nanotubes in Aqueous Mixtures of Surfactants",* Poster Presentation, Treffen der Norddeutschen Biophysicker, **Borstel, Germany**, *January 2013*

3. **Edita Sarukhanyan**, Danilo Roccatano and Giuseppe Milano, *"Coarse-Grain Simulation Studies of Spontaneous Insertion of Double-walled Carbon Nanotube Bundles Inside DPPC Lipid Bilayer",* Oral Presentation, Workshop on research at interface between biomedicine and nanoscience, University of Salerno, **Salerno, Italy**, *June 2012*

4. **Edita Sarukhanyan**, Giuseppe Milano and Danilo Roccatano, *"Atomistic Simulations of Carbon Nanotubes in Aqueous Mixtures of Surfactants",* Poster Presentation, NanoFun Center and NanoMol Graduate Program Retreat, Jacobs University Bremen, **Germany,** *May 2012*

5. Attended the CCP5/CECAM *"Methods in Molecular Simulation Summer School 2010"* at Queen's University Belfast, **Belfast, U. K,** *July, 18th-27th*

ABSTACT

Ever since their discovery, carbon nanotubes (CNTs) have grabbed attention of the researchers from different fields of science and industry. In fact, their excellent physicochemical properties together with an ability to cross biological membranes provide innumerable possibilities for diverse applications, including biomedical and pharmacological applications. Surface modification of CNTs by biological molecules will create a new series of bioactive nanotubes which will lead to the direction of specific cell targeting. The main principles of CNT interactions with biological interfaces are still under active investigation. Experimental data suggest various ways of CNT surface modification, as well as, their pathways of internalization through the cellular membrane. Nowadays, the availability of both large computational resources and powerful computational methods, as Molecular Dynamics (MD) simulation, provides an opportunity to study these interactions at atomic level with high order of accuracy.

The goal of the research work for this thesis is the multi-scale simulation study of CNTs with various biological interfaces. Initially, the study of the CNT coating mechanism by surfactants at both atomistic and coarse-grained levels has been carried out. Linear polymeric ether – based surfactants are known to coat the surface of the nanotubes and, thus, make them soluble in water. In this simulation study the distribution of the polymers of different length around CNT, as well as, the numbers of aggregated chains are found to be compatible with experimental data results. Further, investigation of the orientation and aspect ratio dependent interaction of CNT bundles with the DPPC lipid bilayer has been performed by a recently developed MD-SCF approach. The simulations have provided a molecular model of the perturbation in the structure of the lipids bilayer induced by the CNT bundles insertion process. The results have shown that strong perturbations occur only when the CNT bundles are oriented perpendicularly respect to the bilayer plane. The pore formation has also been observed with the longest CNT bundle.

Finally, the atomistic MD simulations have been performed to study the structural behavior of antimicrobial hybrid peptide CA-MA in aqueous solutions under different physiological conditions. This specific hybrid peptide is of great interest to be explored, because

ABSTRACT

of its bactericidal and tumoricidal abilities. The results of this study have shown that the peptide receives random coil conformation in water, which is in accordance with experimental results. Partial stabilization of the α-helix structure was found in the case of simulation in salty environment and the irreversible loss of the α-helical content was observed at the physiological temperature of 310 K. The peptide concentration plays a stabilizing role on secondary structure of the peptide. However, at these concentrations, peptide aggregation takes place. The studies of the CA-MA peptide have been further extended for the case of interactions with CNT and graphene sheet. In both cases the rapid loss of α-helical content has been observed at the time of the peptide's contact with the solid carbon – based nanosurfaces.

ABBREVIATIONS

CNT	Carbon Nanotube
SWCNT	Single-walled Carbon Nanotube
DWCNT	Double-walled Carbon Nanotube
MD	Molecular Dynamics
AMD	Atomistic Molecular Dynamics
VMD	Visual Molecular Dynamics
SCF	Self-Consistent Field
CG	Coarse-grained
GROMACS	GROningen MAchine for Chemical Simulation
MARTINI	MARrink's Toolkit INItiative
LJ	Lennard-Jones
SPC	Simple Point Charge
DME	1,2-dimethoxyethane
DMP	1,2-dimethoxypropane
PEO	Polyethylene oxide
PPO	Polypropylene oxide
RDF	Radial Distribution Function
SDF	Spatial Distribution Function
DPPC	Dipalmitoylphosphatidylcholine
CA-MA	Cecropin A – Magainin 2

CONTENTS

CONTENTS

CONTENTS

CONTENTS

CHAPTER 1:

INTRODUCTION

CHAPTER 1

The science and technology of nanoscale materials, devices, and their applications in molecular-electronics, nanocomputers, sensors, actuators, and molecular machines form the core of nanotechnology.[1] The prefix "nano" comes from Greek "nanos" which means "dwarf"[2] and corresponds to a basic unit on a length scale, meaning 10^{-9} meters, which is a hundred to a thousand times smaller than a typical biological cell or bacteria.[1] The initial idea to combine individual atomic and molecular building blocks in order to develop useful materials, devices and applications was given by the Nobel prize winner physicist - Richard Feynman in lecture "There's a Plenty of Room at the Bottom" at Cal Tech in 1959 in which he said *"The problems of chemistry and biology can be greatly helped if our ability to see what we are doing, and to do things on an atomic level, is ultimately developed – a development which I think cannot be avoided"*.[1] Indeed, development of devices such as scanning probe microscopes and similar techniques has given opportunities to manage the processes at atomic level, which shed light on growth of nanotechnology of past decades.[1] The huge progress in nanotechnology has been achieved by the discovery of nanoscale materials, such as fullerenes in the mid – 1980s and carbon nanotubes, discovered by Iijima[3] in the early 1990s.

Nowadays, computer simulation tools and molecular modeling provide innumerable possibilities to study interactions of nano – sized objects at atomic level.

1.1 CARBON NANOTUBES

Carbon nanotubes (CNTs) are graphitic nanomaterials that possess many outstanding properties.[4-6] They are known as the stiffest and strongest fibers with remarkable electronic properties and many other unique characteristics. These are the reasons CNTs have become the most attractive subject for many branches of science and industry. CNTs can be single walled (SWNT) or multiple walled (MWNT), varying in diameter and length, with closed capped section or open ends. The diameter of nanotube can be in the range between 0.4 up to 100 nm and the length – from several nanometers up to centimeters. The tubes present by themselves a rolled up graphene sheets (graphene is an individual graphite layer). Depending on the way of

how these sheets will be rolled up, different structures with different properties of the nanotubes can be obtained.[7] The structure of the nanotube can be specified by a vector C_n ($C_n = m\mathbf{a1}+n\mathbf{a2}$), that determines the direction of rolling a graphene sheet, in which a lattice point (m, n) is superimposed with the origin, defined as (0, 0). This can be understood with the reference to the Figure1.1. To produce a nanotube, for example, with the indices (7, 3), the sheet is rolled up so that the atom labeled (0, 0) is superimposed with the one labeled (7, 3). In the case if n=0, the zig-zag nanotube is obtained, when m = n – arm-chair and, finally, when m ≠ n, the nanotube is called chiral. Figure 1.2 represents the three structures of CNTs.

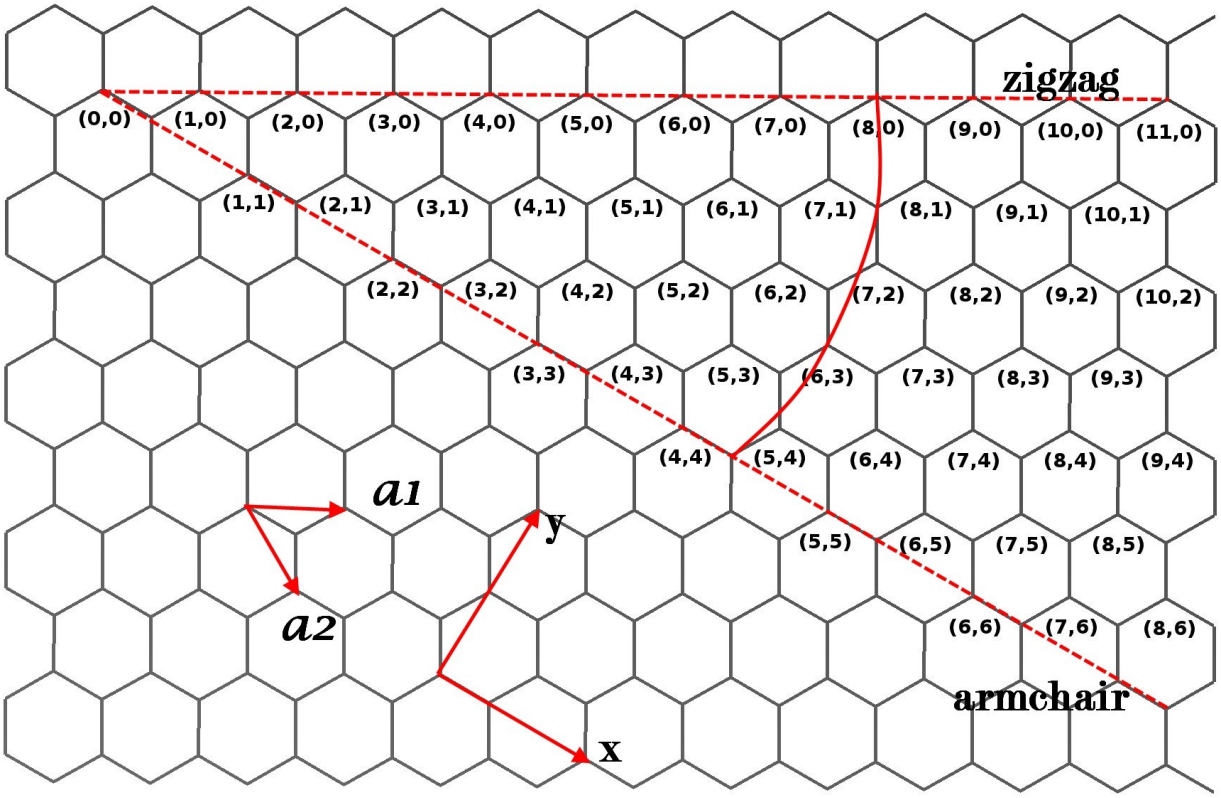

Figure1.1: Graphene sheet. Unitary vectors ***a1*** and ***a2*** are necessary to determine the rolling direction expressed by vector ***Cn***.

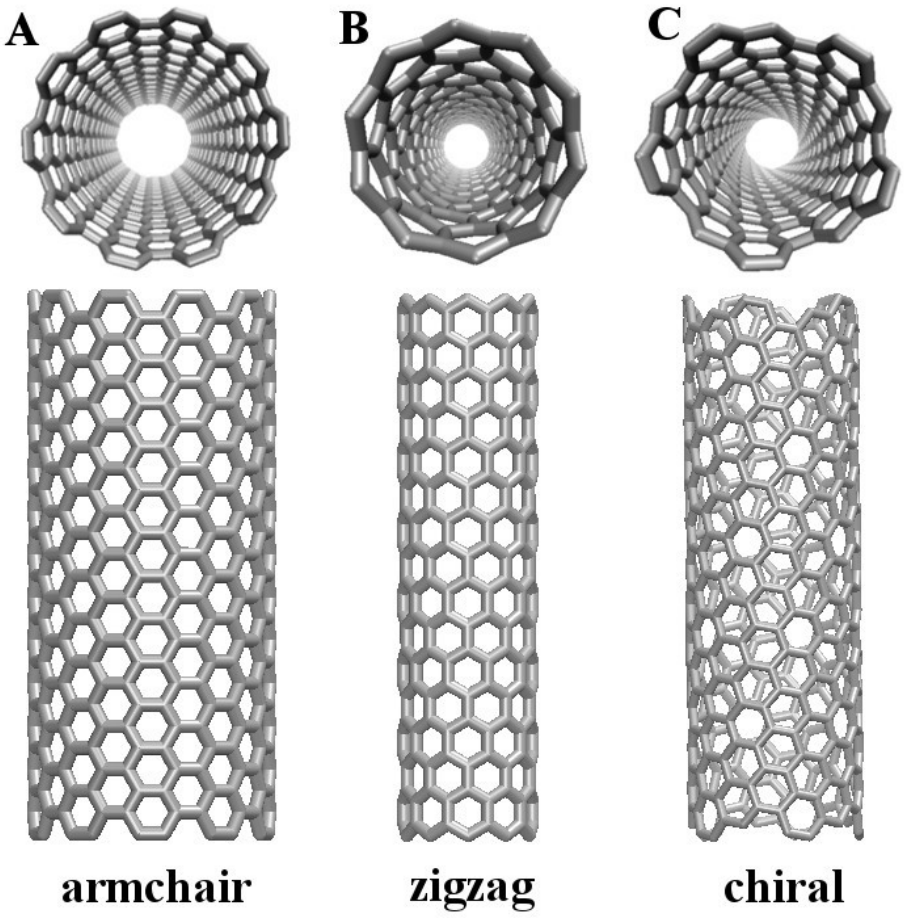

Figure 1.2: Molecular models of SWCNT exhibiting different chiralities: a) arm-chair configuration, b) zig-zag arrangement and c) chiral conformation.

1.2 BIOMEDICAL APPLICATION OF CARBON NANOTUBES

Since their discovery, various biological and biomedical applications[8-9] of CNTs have been proposed by researchers leading towards new field in diagnostics and therapeutics.[10] Some of the examples of biomedical application of CNT are reported here.

Development of pressure sensors, based on CNT incorporation is extremely efficient and of great demand in biomedicine. Such sensors can be applied in eye surgery, respiratory devices, patient monitors, inhalers as well as kidney dialysis machines.[9] Another attracting application of CNTs is their exploitation as atomic force microscopy (AFM) probes. Usually, AFM generated image

is highly dependent on the shape of AFM tips and surface structure of the investigated sample. An optimal radius of the tip should be commensurable with atomic proportions. Compared to silicon probes, the probes made of CNTs have high resolutions. Because of their cylindrical shape and small diameter it is possible to image narrow and deep cavities of a sample. Using CNTs as AFM tip, the research group of Stevens was able to reproduce an image of a protein filament.[11]

Quantum dots are biological labels having size of 2 - 10 nm and very useful for imaging and spectroscopy of cancer cells, disease diagnostics, targeted therapeutics and drug screening. It has been shown that CNTs can be used as quantum dots.[9,12-13]

One of the best features of CNTs is the ability to cross cell membranes.[14-15] Hence, CNTs can be used as nano-containers for drug delivery.[14,16-18] They have large inner space that can be filled with desired drug or any other molecule of interest. The outer surface of the nanotube can be modified with biocompatible materials in order to reduce cytotoxicity. This point will be described more in detail in the following part related to Functionalization of Carbon Nanotubes. In addition, CNTs have open ends, which allow insertion of required material inside the nanotube.[19] The encapsulation of a drug or other bioactive molecules inside the nanotube is mostly governed by van der Waals and hydrophobic forces. Drug delivery systems based on CNTs open new opportunities for treatment of diseases like cancer, HIV/AIDS, malaria and metabolic diseases[18,20-21] as well as gene therapy.

Furthermore, CNTs can be used as implantable nanosensors and nanorobots.[9] CNT based nanosensors have the advantages that they are thousand times smaller than microelectromechanical systems sensors and consume less power. Therefore, they are highly suitable as implantable sensors. Implanted sensors can be used for monitoring pulse, temperature, blood glucose and diagnosing diseases.[9,22] Implantable nanosensors can also monitor heart's activity level and regulate heartbeats by communicating with an implantable defibrillator. Implanted nanorobots[23] may do several functions, such as treatment of skin diseases, protection of immune system by identification and neutralization of unwanted bacteria, deactivation of pathogenic bacteria in mouth cavity, thus protecting teeth against plaque and tartar.

It has been shown that CNTs can act as actuators.[24] CNT actuators are able to work under physiological environment, low voltages, and temperatures as high as 350˚C. Nanotube based polymer composites have promise as possible artificial muscle devices[25] because of their incredible strength and stiffness.

These are just a few out of the huge amount of varieties of CNT applications. In Figure 1.3 one can see some example pathways of CNT applications.

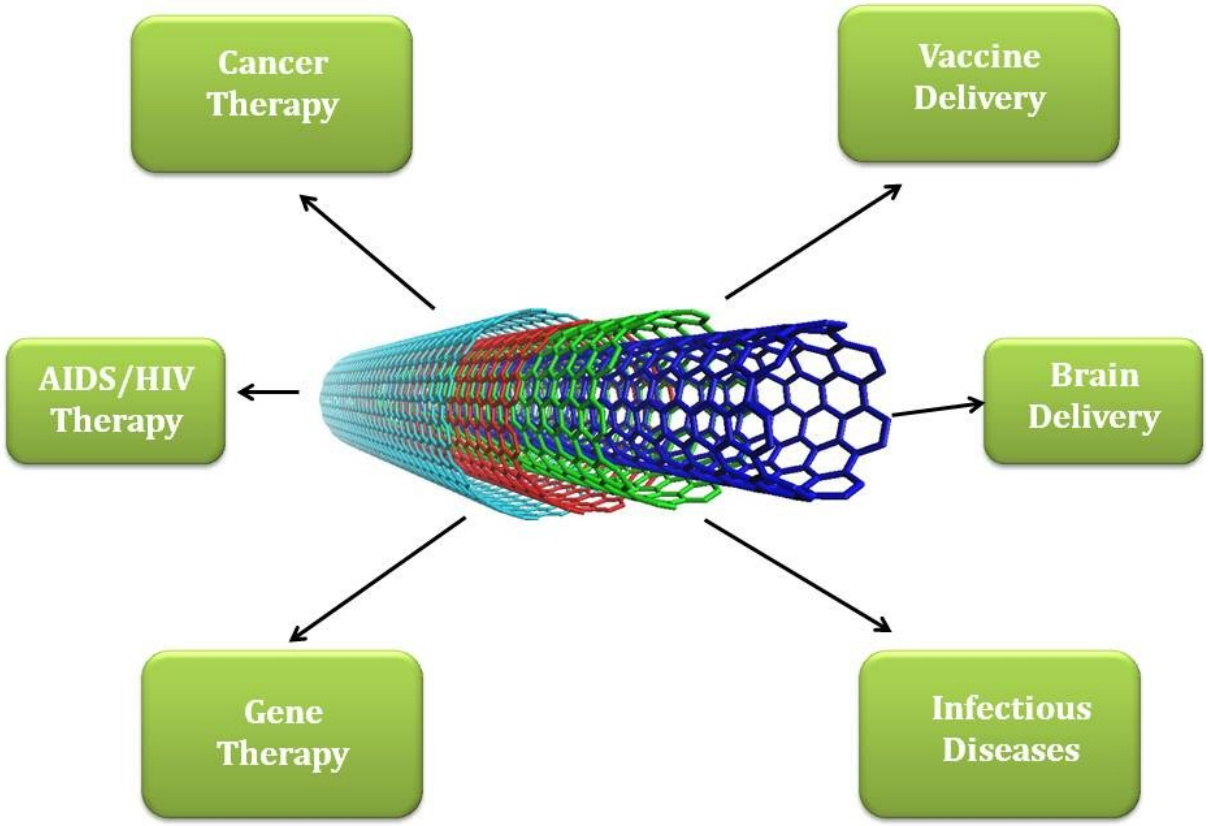

Figure 1.3: Various application of CNTs in delivery of bioactives.

1.3 FUNCTIONALIZATION OF CARBON NANOTUBES

Due to their hydrophobicity and tendency to aggregate, CNTs are very harmful for living cells.[26-28] Cell studies related to CNT cytotoxicity have shown that CNTs, in general, are very toxic. However, this factor mainly depends on the size, surface chemistry and aspect ratio of the nanotube.[29] For further biomedical applications their surface must be modified in order to make them biocompatible and soluble in water. Several solutions have been proposed to overcome these problems. One of the solutions is surface modification, which can support biocompatibility and low toxicity. CNTs can be functionalized with different functional groups, useful for targeting, imaging or therapy.[20] Attachments of functional groups to the surface of the nanotube may be covalent or non-covalent.[20,30-33] Covalent modification is mostly associated with functionalization of nanotube surface by various chemical groups that can be bonded to nanotube surface covalently, while non-covalent implies coating of the nanotube surface with amphiphilic molecules like lipids and polymers.[20] It should be noted that an ideal non-covalent functionalization for biological application must be, first, biocompatible and nontoxic and, second, the coating should be sufficiently stable to resist detachment from the nanotube surface in biological solutions, like serum with high concentration of salt and protein.[30]

1.3.1 Covalent functionalization

Covalent modification by functionalization of end-groups and side walls of CNTs[33] produces a significant increase of the solubility of CNTs in a range of solvents, including water.[34-35] Some of the examples of covalent surface modifications include side wall halogenation of CNT, adding cyclo-additions, radical additions, addition of inorganic compounds and ozonolysis.[32] Such modifications of CNT surface provides multiple sites for the covalent attachments of drugs, amino acids, sugars, DNA, oligonucleotides, peptides, proteins or enzymes.[14] The main disadvantage of this method is that the defects of the CNT side-walls has place in this case.

1.3.2 Non-covalent functionalization

Non-covalent functionalizations are often used in medical applications of CNTs. These modifications do not disrupt electronic structure of nanotubes and physical properties of CNTs can be saved. There are two paths by which the nanotube can be functionalized non-covalently. First implies the wrapping of the polymer around the CNT surface [36] and the second is performed through π-π stacking interaction between aromatic rings of the loaded materials and π electrons on the surface of CNTs.[37-38] Non-covalent surface modifications will prevent CNTs from aggregation into bundles and favor their water solubility.

1.4 INTERACTIONS OF CARBON NANOTUBE WITH BIOLOGICAL INTERFACES: EXPERIMENTAL AND THEORETICAL STUDIES.

Since the importance of nanotechnology grows every day and application of CNTs in nanomedicine is highly promising, it is useful to understand the interactions of CNTs with biological interfaces. Understanding of principles based on physicochemical interactions, kinetics and thermodynamic exchanges between the CNT surface and the surfaces of biological components, such as proteins, membranes, phospholipids, endocytic vesicles and organelles will open new opportunities for better design of nano-transporters, aimed for treatment of diseases. Several studies have been performed in order to understand the pathways of CNT internalization through the membranes of various cells.[15,39-44] Direct imaging of SWCNT in cells has been carried out by Porter[39] by confocal microscopy and transmission electron microscopy (TEM) techniques. The studies have been performed on human monocyte-derived macrophages (HMMs) *in vitro*. It was shown that SWCNT were able to enter cells and even reach the cell nucleus, causing lethal outcome in a dose-dependent manner.[39] The study suggests two possible pathways of internalization: energy-dependent phagocytosis or endocytosis and passive diffusion

across lipid bilayer.[39] Later, by the same author – by Porter[41] it was demonstrated cellular uptake of acid treated SWCNTs. Raman spectroscopy and TEM were used in this case. The acid treated SWCNTs showed to be more frequent in crossing cell membrane and less cytotoxic rather than untreated ones. Group of Zhou[42] using confocal laser scanning microscopy has studied translocation of SWCNT, functionalized with phospholipid-polyethylene glycol (PL-PEG), inside healthy, tumor and macrophage cells. Observance of PL-PEG-SWCNT in mitochondria of both healthy and cancerous cells and, mainly, lysosomal distribution for macrophage cells had place. Not the passive membrane transection, but energy-dependent endocytosis is the only path by which SWCNT enters the cell and is suggested by Yaron et al.[44] In the study F127 pluronic coated SWCNT was found in endosomes while entering the HeLa cells.

One of the most powerful methods for investigation of CNT interaction with lipid bilayer, as a model of biological membrane, is molecular dynamics (MD) method. Preliminary studies, implementing MD approach have been reported in a research of Wallace and Sansom.[45] With the usage of Steered Molecular Dynamics (SMD) methods investigation of interactions between SWNT of various diameters (1.4-6.1nm) and dipalmitoylphosphatidylcholine (DPPC) lipid bilayer at different pulling velocities (0.5 and 50 nm/ns) was carried out. It was shown that during penetration of carbon nanotube through bilayer deformation of the last one was occurred, that, in turn, had been depended on the pulling velocity.

The perspective of CNT application as nanovectors depends on their ability to porate the cellular membrane. Non equilibrium all-atom SMD simulations have been performed by Gangupomu and Capaldi[46] to study the forces and the free energy required to puncture the membrane and form a pore by CNT. The presence of 30 % cholesterol in a Palmitoyl, 2-Oleyoyl, Phosphatidylcholine (POPC) lipid membrane has been considered, as well. The results obtained by the authors suggest that the force needed to rupture the membrane depends on pulling velocity of the CNT, namely, the lower is the speed lower is the penetration force. The presence of cholesterol did not significantly change the rupture forces or free energies, but it favored membrane poration by the nanotube.[46]

1.5 AIM AND THE OUTLINE OF THE THESIS

The aim of the thesis is focused on understanding of the mechanisms of interactions of CNTs with biological interfaces using different levels of simulation techniques. In particular, the study comprises interactions of CNTs with linear ether – based polymers; phospholipid bilayer and peptides. One of the methods used to perform simulations is atomistic molecular dynamics (AMD) approach. AMD simulations reproduce the data in accurate manner, which allow the understanding of the interactions at atomic level. However, this method does not allow investigation of large systems (> 100 nm) for a long computational time interval (> 1 μs). One way to speed up calculations is to simplify the molecular model by unification of several atoms into one, so called coarse-grained (CG) models, and reduction of the degrees of freedom. Such model, which is used in the present work, is MARTINI[47] model. The other way is to simplify the most computationally expensive part of the simulation, i.e. the potential of interaction between the particles. New approach based on combination of self-consistent field theory (SCF) and molecular dynamics (SCF-MD) has been developed by Prof. Giuseppe Milano[48] in our research group at the University of Salerno for this purpose.

The thesis is organized as follows. In **Chapter 2** computational methods, used to perform simulations are explained. **Chapter 3** describes the coating mechanism of SWCNT by poloxamers based surfactant. In particular, the study includes the distribution of one monomer (1, 2 dimethoxyethane (DME) and 1, 2 – dimethoxypropane (DMP)), PEO/PPO pentamers and L64 triblock copolymer respect to SWCNT surface. Since CNTs represent insoluble aggregates in aqueous media, the idea of the study was driven due to the purpose to use surfactants for CNT solubilisation. The studies has been extended for longer polymer chains using MD-SCF method and in the **Chapter 4** adsorption of F127 and F108 pluronics on the surface of CNT bundles of different length is reported. The results are compared with available experimental data.

CNTs are able to cross biological membranes. This unique feature of CNTs can be applied for pharmaceutical purposes for CNT based drug delivery. The exact pathways of CNT internalization are still under investigation. In order to understand the principles of CNT interaction with cell membranes, it is important, first, to clarify how CNTs interact with pure

lipid bilayer. For this purpose, one part of the PhD thesis was dedicated to the study of interactions of CNTs with lipid bilayer. In particular, in the **Chapter 5** orientation and aspect ratio dependent interactions of double-walled carbon nanotube (DWCNT) bundles with the DPPC lipid bilayer, as a model of cellular membrane is described.

Chapters 6 and **7** are containing information related to simulations of antimicrobial hybrid peptide Cecropin A – Magainin 2. Antimicrobial peptides are found to play an important role for the fight against new antibiotic resistant bacteria and cancer. For this reason it is vital to understand their structural behavior under physiological conditions. **Chapter 6** is dedicated to the study of the behavior of antimicrobial Cecropin A – Magainin 2 (CA-MA) hybrid peptide in aqueous solutions under different conditions. Mainly, understanding the influence of the factors such as temperature, ionic strength and peptide concentration on the secondary structure of the peptide is the focus of this chapter.

The ability of CA-MA hybrid peptide to lyse bacterial cells can be used against bacterial contamination of materials. Understanding the structural behavior of CA-MA peptide during the interaction with solid surfaces will provide an opportunity for their better future applications. In **Chapter 7** the curvature dependence interaction of CA-MA peptide with carbon – based surfaces, such as CNT and graphene, is considered.

The main results and future perspectives are summarized in the **Summary and Outlook** part of **Chapter 8**.

1.6 REFERENCES

(1) Meyyappan, M. *Carbon nanotubes: science and applications*; CRC press, **2004**.

(2) Ramakrishna, S. *An introduction to electrospinning and nanofibers*; World Scientific, **2005**.

(3) Iijima, S. *Nature* **1991**, *354*, 56.

(4) Lu, J. P. *Physical review letters* **1997**, *79*, 1297.

(5) Salvetat, J.-P.; Bonard, J.-M.; Thomson, N.; Kulik, A.; Forro, L.; Benoit, W.; Zuppiroli, L. *Applied Physics A* **1999**, *69*, 255.

(6) Odom, T. W.; Huang, J.-L.; Kim, P.; Lieber, C. M. *The Journal of Physical Chemistry B* **2000**, *104*, 2794.

(7) Terrones, M. *Annual review of materials research* **2003**, *33*, 419.

(8) Yang, W.; Thordarson, P.; Gooding, J. J.; Ringer, S. P.; Braet, F. *Nanotechnology* **2007**, *18*, 412001.

(9) Sinha, N.; Yeow, J.-W. *NanoBioscience, IEEE Transactions on* **2005**, *4*, 180.

(10) Lacerda, L.; Bianco, A.; Prato, M.; Kostarelos, K. *Advanced drug delivery reviews* **2006**, *58*, 1460.

(11) Stevens, R. M.; Frederick, N. A.; Smith, B. L.; Morse, D. E.; Stucky, G. D.; Hansma, P. K. *Nanotechnology* **2000**, *11*, 1.

(12) Tans, S. J.; Devoret, M. H.; Dai, H.; Thess, A.; Smalley, R. E.; Geerligs, L.; Dekker, C. *Nature* **1997**, *386*, 474.

(13) Bockrath, M.; Cobden, D. H.; McEuen, P. L.; Chopra, N. G.; Zettl, A.; Thess, A.; Smalley, R. E. *Science* **1997**, *275*, 1922.

(14) Lacerda, L.; Raffa, S.; Prato, M.; Bianco, A.; Kostarelos, K. *Nano Today* **2007**, *2*, 38.

(15) Lamprecht, C.; Liashkovich, I.; Neves, V.; Danzberger, J.; Heister, E.; Rangl, M.; Coley, H. M.; McFadden, J.; Flahaut, E.; Gruber, H. J. *Nanotechnology* **2009**, *20*, 434001.

(16) Pastorin, G. *Pharmaceutical research* **2009**, *26*, 746.

(17) Prato, M.; Kostarelos, K.; Bianco, A. *Accounts of chemical research* **2007**, *41*, 60.

(18) Bhirde, A. A.; Patel, V.; Gavard, J.; Zhang, G.; Sousa, A. A.; Masedunskas, A.; Leapman, R. D.; Weigert, R.; Gutkind, J. S.; Rusling, J. F. *ACS nano* **2009**, *3*, 307.

(19) Gao, H.; Kong, Y.; Cui, D.; Ozkan, C. S. *Nano letters* **2003**, *3*, 471.

(20) Kostarelos, K.; Bianco, A.; Prato, M. *Nature Nanotechnology* **2009**, *4*, 627.

(21) Kesharwani, P.; Ghanghoria, R.; Jain, N. K. *Drug discovery today* **2012**, *17*, 1023.

(22) Shults, M. C.; Rhodes, R. K.; Updike, S. J.; Gilligan, B. J.; Reining, W. N. *Biomedical Engineering, IEEE Transactions on* **1994**, *41*, 937.

(23) Bhargava, A. *Short Circuit* **1999**, *1*, 1999.

(24) Baughman, R. H.; Cui, C.; Zakhidov, A. A.; Iqbal, Z.; Barisci, J. N.; Spinks, G. M.; Wallace, G. G.; Mazzoldi, A.; De Rossi, D.; Rinzler, A. G. *Science* **1999**, *284*, 1340.

(25) Vohrer, U.; Kolaric, I.; Haque, M.; Roth, S.; Detlaff-Weglikowska, U. *Carbon* **2004**, *42*, 1159.

(26) Buzea, C.; Pacheco, I. I.; Robbie, K. *Biointerphases* **2007**, *2*, MR17.

(27) Monteiro-Riviere, N. A.; Nemanich, R. J.; Inman, A. O.; Wang, Y. Y.; Riviere, J. E. *Toxicology letters* **2005**, *155*, 377.

(28) Cui, D.; Tian, F.; Ozkan, C. S.; Wang, M.; Gao, H. *Toxicology letters* **2005**, *155*, 73.

(29) Magrez, A.; Kasas, S.; Salicio, V.; Pasquier, N.; Seo, J. W.; Celio, M.; Catsicas, S.; Schwaller, B.; Forró, L. *Nano letters* **2006**, *6*, 1121.

(30) Liu, Z.; Tabakman, S.; Welsher, K.; Dai, H. *Nano research* **2009**, *2*, 85.

(31) Zhang, Y.; Bai, Y.; Yan, B. *Drug discovery today* **2010**, *15*, 428.

(32) Tasis, D.; Tagmatarchis, N.; Bianco, A.; Prato, M. *Chemical Reviews* **2006**, *106*, 1105.

(33) Hirsch, A. *Angewandte Chemie International Edition* **2002**, *41*, 1853.

(34) O'Connell, M. J.; Boul, P.; Ericson, L. M.; Huffman, C.; Wang, Y.; Haroz, E.; Kuper, C.; Tour, J.; Ausman, K. D.; Smalley, R. E. *Chemical Physics Letters* **2001**, *342*, 265.

(35) Sano, M.; Kamino, A.; Okamura, J.; Shinkai, S. *Langmuir* **2001**, *17*, 5125.

(36) Star, A.; Stoddart, J. F.; Steuerman, D.; Diehl, M.; Boukai, A.; Wong, E. W.; Yang, X.; Chung, S. W.; Choi, H.; Heath, J. R. *Angewandte Chemie International Edition* **2001**, *40*, 1721.

(37) Petrov, P.; Stassin, F.; Pagnoulle, C.; Jérôme, R. *Chemical Communications* **2003**, 2904.

(38) Chen, J.; Liu, H.; Weimer, W. A.; Halls, M. D.; Waldeck, D. H.; Walker, G. C. *Journal of the American Chemical Society* **2002**, *124*, 9034.

(39) Porter, A. E.; Gass, M.; Muller, K.; Skepper, J. N.; Midgley, P. A.; Welland, M. *Nature Nanotechnology* **2007**, *2*, 713.

(40) Bussy, C.; Cambedouzou, J.; Lanone, S.; Leccia, E.; Heresanu, V.; Pinault, M.; Mayne-l'Hermite, M.; Brun, N.; Mory, C.; Cotte, M. *Nano letters* **2008**, *8*, 2659.

(41) Porter, A. E.; Gass, M.; Bendall, J. S.; Muller, K.; Goode, A.; Skepper, J. N.; Midgley, P. A.; Welland, M. *ACS nano* **2009**, *3*, 1485.

(42) Zhou, F.; Xing, D.; Wu, B.; Wu, S.; Ou, Z.; Chen, W. R. *Nano letters* **2010**, *10*, 1677.

(43) Al-Jamal, K. T.; Nerl, H.; Muller, K. H.; Ali-Boucetta, H.; Li, S.; Haynes, P. D.; Jinschek, J. R.; Prato, M.; Bianco, A.; Kostarelos, K.; Porter, A. E. *Nanoscale* **2011**, *3*, 2627.

(44) Yaron, P. N.; Holt, B. D.; Short, P. A.; Losche, M.; Islam, M. F.; Dahl, K. N. *J Nanobiotechnology* **2011**, *9*, 45.

(45) Wallace, E. J.; Sansom, M. S. *Nano letters* **2008**, *8*, 2751.

(46) Gangupomu, V. K.; Capaldi, F. M. *Journal of Nanomaterials* **2011**, *2011*.

(47) Marrink, S. J.; Risselada, H. J.; Yefimov, S.; Tieleman, D. P.; de Vries, A. H. *Journal of Physical Chemistry B* **2007**, *111*, 7812.

(48) Milano, G.; Kawakatsu, T. *The Journal of chemical physics* **2009**, *130*, 214106.

CHAPTER 2:

COMPUTATIONAL METHODS

CHAPTER 2

2.1 MOLECULAR DYNAMICS SIMULATIONS

2.1.1 Algorithm

Molecular dynamics (MD) simulation is a tool to calculate the physicochemical properties of the real system in specific thermodynamic conditions. Under thermodynamic conditions is implied constant temperature, pressure, surface tension and so on. Based on this method it is possible to study the structure of solids, liquids and gases. The principle of MD is following: similarly as in experiments, the sample should be prepared at the first point. It means that the basic parameters, such as temperature, number of particles, density, time step, initial positions and velocities must be set.[1] Since the system of *N* particles is selected, the program computes the forces, acting on all particles and solves Newton's equation of motion (Eq. 2.1.1) for this system until the properties of the system do not change any more (equilibrium state):

$$m_i \frac{d^2 r_i(t)}{dt^2} = \boldsymbol{F}_i(r_1 \dots r_N) \tag{2.1.1}$$

Here r_i are the positions of the particles with the mass m_i and $\boldsymbol{F_i}$ is the force depending on the positions of all *N* particles in the system. The force acting between the particles is calculated using the potential energy function $V(r_1 \dots r_N)$. Mathematically this is given by the negative of the first derivative of the function:

$$\boldsymbol{F}_i = -\frac{\partial}{\partial r_i} V(r_1 \dots r_N) \tag{2.1.2}$$

If the force is known, we can predict the next position of the atom in the time interval δt (time step). Usually this is done by one of the simplest algorithm, the so-called Leap-Frog[2] algorithm, which is performed by the following integration scheme:

$$\boldsymbol{v_i}\left(t + \frac{1}{2}\delta t\right) = \boldsymbol{v_i}\left(t - \frac{1}{2}\delta t\right) + \frac{\boldsymbol{F_i}}{m_i}(\delta t) \tag{2.1.3}$$

$$\boldsymbol{r_i}(t + \delta t) = \boldsymbol{r_i}(t) + \delta t \boldsymbol{v_i}(t + \frac{1}{2}\delta t) \tag{2.1.4}$$

Where $\boldsymbol{v_i}$ is the velocity of i-th particle, $\boldsymbol{F_i}$ is the force acting on the particle i with the mass m_i, $\boldsymbol{r_i}$ is the position of i-th particle.

This is repeated for several thousands of time steps until the properties of system do not change any more, and the equilibrium state is reached. Then analysis can be performed based on methods of statistical mechanics to explore the bulk properties of the material (e.g. secondary structure, temperature, pressure, viscosity, diffusion etc.).

2.1.2 Interaction Potentials

In MD simulation the potential of interaction which characterizes the force field includes two parts of interactions. These are bonded and non – bonded interactions:

$$V(r_1, r_2, r_3, \dots, r_N) = E_{tot} = E_{bonded} + E_{non-bonded} \quad (2.1.5)$$

Where further is defined as,

$$E_{bonded} = E_{bond} + E_{angle} + E_{dihedral} \quad (2.1.6)$$

$$E_{non-bonded} = E_{van-der-Waals} + E_{electrostatic} \quad (2.1.7)$$

Bonded interactions

The bonded interactions are usually described by the function dependent on two body interactions. The form of the function is expressed as a harmonic potential function:

$$E_{bond} = \sum_{bonds} \frac{1}{2} K_b (b - b_0)^2 \quad (2.1.8)$$

Where K_b is a force constant for bond usually obtained from experimental crystallographic and spectroscopic data, b is the bond length and b_0 is an equilibrium bond length.

The bond-angle vibrations are three body interactions which describe the deviation from the initial bond angle geometry due to the motional deformations and defined again as harmonic expression as,

$$E_{angle} = \sum_{angle} \frac{1}{2} K_\theta (\theta - \theta_0)^2 \quad (2.1.9)$$

Where K_θ is a force constant for angle, θ is the angle, θ_0 is an equilibrium angle.

Torsional interactions involve four atoms (*i, j, k* and *l*) and define the dihedral angle Φ as the angle between two planes that pass through the triplet of atoms (*i, j* and *k*) and (*j, k* and *l*).

$$E_{dihedral} = \sum_{dihedral} K_{\phi} \left(1 + \cos(n\phi - \phi_s)\right) \quad (2.1.10)$$

Where K_{ϕ} is the rotational constant for the dihedral angle energy, n is the periodicity of the rotational barrier, ϕ is the dihedral angle between the two planes, formed by the triplets of atoms (i, j, k) and (j, k, l) and ϕ_s is the phase factor.

Improper dihedrals are used to define the planarity of the four atoms (i, j, k and l) and are expressed by harmonic interaction potential

$$E_{improper\ dih.} = \sum_{improper\ dih.} \frac{1}{2} K_{\xi} \left(\xi - \xi_0\right)^2 \quad (2.1.11)$$

Where K_{ξ} is the force constant and ξ is the dihedral angle on four atoms (i, j, k and l) to keep them in special configuration. For example, ξ_0 will be equal to 0˚to keep the four atoms in planar configuration.

Non-bonded interactions

The molecular non-bonded interactions as in equation 2.1.5 are consisting of van der Waals (vdW) and electrostatic interactions. The vdW interactions are presented by Lennard-Jones (LJ) potential function and it expresses the interaction energy between two atoms. The LJ potential is a short range potential defined as,

$$E_{van-der-Waals} = \sum_i \sum_{j>i} 4\varepsilon_{ij} \left(\frac{\sigma_{ij}^{12}}{r_{ij}^{12}} - \frac{\sigma_{ij}^{6}}{r_{ij}^{6}}\right) \quad (2.1.12)$$

Where r is the distance between particles, ε_{ij} is the well depth and σ_{ij} is the distance at which the inter potential is zero. This potential contains an attractive part and a repulsive part. Attractive forces are due to dipole-dipole interactions and the repulsive part is due to Pauli-exclusion principle and inter-nuclear repulsion.

The electrostatic interactions are defined as simple coulombic potential function,

$$E_{electrostatic} = \sum_i \sum_{j>i} \left(\frac{q_i q_j}{4\pi\varepsilon_0 r_{ij}} \right) \quad (2.1.13)$$

Where r is the distance between particles, q_i and q_j are the partial charges on the atoms i and j, respectively, and ε_0 is the dielectric constant in vacuum.

2.1.3 Temperature and Pressure Control

The temperature of the system can be calculated using the average kinetic energy of the N particles with N_f degrees of freedom,

$$\frac{1}{2} k_b N_f T = \sum_{i=1}^{N} \frac{1}{2} m_i v_i^2 \quad (2.1.14)$$

Where v_i is the velocity of particle i with mass m_i.

The pressure expression of the system is based on virial theorem.[3] Thus, the pressure is expressed as summation of ideal part ($PV=NkT$) and the summed product of forces (F_{ij}) acting on particles at distances (r_{ij}) between the centers of mass of the molecules,

$$PV = NkT + \frac{1}{3} \sum_{i<j}^{N} \langle r_{ij} * F_{ij} \rangle \quad (2.1.15)$$

In order to control the temperature of the system and the pressure one can use weak temperature and pressure coupling to an external bath i.e. Berendsen method.[4] In this approach, at each integration step, the atomic velocities, v, are scaled to λv, to change the temperature of the system $T(t - \frac{1}{2}\delta t)$ to the reference temperature, T_0. λ is a constant and defined as,

$$\lambda = \left[1 + \frac{\delta t}{\tau_T} \left(\frac{T_0}{T\left(t - \frac{1}{2}\delta t\right)} - 1 \right) \right]^{\frac{1}{2}} \quad (2.1.16)$$

Where τ_T is the coupling parameter and T_0 is the thermostat fixed temperature. The coupling to the reference pressure, P_0 is performed by scaling of coordinates r to ηr as,

$$\eta = \left[1 + \frac{\Upsilon \delta t}{\tau_p}(P(t) - P_0)\right]^{\frac{1}{2}} \quad (2.1.17)$$

Where *P(t)* is the system pressure at time *t* and Υ is the compressibility of the system. τ_p is the coupling parameter or strength of coupling.

Another method to maintain the temperature constant is based on Andersen's thermostat.[1,5] In this thermostat the system is coupled to heat bath of desired temperature. The coupling to the heat bath is performed by stochastic collisions that act occasionally on randomly selected particles. In the Andersen's thermostat collisions are not performed at each MD step but it is described by in advance chosen collision frequency *v*. The distribution of time intervals between the two stochastic collisions can be expressed by Poisson formula:

$$P(t; \nu) = \nu exp[-\nu t] \quad (2.1.18)$$

Where $P(t; \nu)dt$ is the probability that the next collision will take place within the time interval $[t, t + dt]$.

The idea of the Andersen's thermostat is based on the following principle:

Once initial positions and momenta $\{\boldsymbol{r}^N(0), \boldsymbol{p}^N(0)\}$ are set, Hamiltonian equation of motions are integrated for a time Δt. The probability that a particle selected in interval Δt will undergo a collision with heat bath is νΔt. For the particle that undergoes collision, the new velocity will be described by Maxwell-Boltzmann distribution with a desired temperature T.

CHAPTER 2

2.2 HYBRID PARTICLE-FIELD MD SIMULATIONS

Despite the computational power and the methods based on acceleration of calculations, hence, saving computational time, is improving every year, it is still difficult to study large systems, consisting of huge number of atoms. For example, calculation of atomic forces in MD simulation is usually the most expensive operation. The forces, acting between atoms are pair forces. So, the force calculation will be performed for each non-bonded atom pairs. For this purpose, coarse-grained models (CG) of molecules were adopted in order to reduce the degrees of freedom, keeping just those ones that are important for a particular task. In order to study large systems, a technique that allows going beyond the CG particle-particle time scales is required. For this purpose, one of the tested and approved tools is a combination of Self-Consistent Field (SCF) and Molecular Dynamics (MD) methods (MD-SCF).[6]

In hybrid MD-SCF method intermolecular interactions are not calculated by pair potentials as in classical MD simulations. Interactions between different molecules are replaced by interactions between single molecules with external density fields. Such external fields depend on the statistical average of the spatial density distribution of the particles which are generated by the separate molecules interacting only with the external fields. These external fields and the particle density distributions must be determined self-consistently. Intramolecular interactions such as bonds, bond angles and intramolecular non-bonded interactions are treated with usual potentials and force fields of classical molecular simulations.

As mentioned, a molecule in SCF model is interacting with surrounding molecules through a mean field. Based on this, the Hamiltonian of the system consisting of M molecules is divided into two parts,[7]

$$\hat{H}\left(\Gamma\right) = \hat{H}_0\left(\Gamma\right) + \hat{W}\left(\Gamma\right) \tag{2.2.1}$$

Where Γ indicates a point in a phase space and is used to describe a set of positions of all atoms in the system. $\hat{H}_0(\Gamma)$ is the Hamiltonian of the reference system, where all the intramolecular interactions, such as bond and bond angle interaction are considered. $\hat{W}(\Gamma)$ is the deviation

from the reference system and considers intermolecular non bonded interactions. Thus, the partition function of the system can be written as,

$$Z = \frac{1}{M!}\int d\Gamma exp\{-\beta[H_0(\Gamma) + \widehat{W}(\Gamma)]\} \quad (2.2.2)$$

Where $\beta = \frac{1}{k_B T}$, k_B is Boltzmann's constant, T is the temperature.

The deviation $\hat{W}(\Gamma)$ from the reference state $\hat{H}_0$ originates from the interactions between the molecules. It is assumed that $\hat{W}(\Gamma)$ depends on Γ through $\varphi(\boldsymbol{r};\ \Gamma)$,

$$\widehat{W}(\Gamma) = \widehat{W}(\varphi(\boldsymbol{r};\ \Gamma)) \quad (2.2.3)$$

Referring to saddle point approximation one can obtain,

$$V(\boldsymbol{r}) = \frac{\delta W[\varphi_K(r)]}{\delta \varphi_K(r)} = k_b T \sum_{K'} \chi_{KK'} \varphi_{K'}(\boldsymbol{r}) + \frac{1}{k}\left(\sum_K \varphi_K(\boldsymbol{r}) - \varphi_0\right) \quad (2.2.4)$$

Taking into consideration a mixture of two components A and B, the potential can be calculated as,

$$V_A(\boldsymbol{r}) = k_B T[\chi_{AA}\varphi_A(\boldsymbol{r}) + \chi_{AB}\varphi_B(\boldsymbol{r})] + \frac{1}{k}(\varphi_A(\boldsymbol{r}) + \varphi_B(\boldsymbol{r}) - \varphi_0) \quad (2.2.5)$$

$$V_B(\boldsymbol{r}) = k_B T[\chi_{BB}\varphi_B(\boldsymbol{r}) + \chi_{AB}\varphi_A(\boldsymbol{r})] + \frac{1}{k}(\varphi_A(\boldsymbol{r}) + \varphi_B(\boldsymbol{r}) - \varphi_0)$$

Where $\varphi_A(\boldsymbol{r})$ is a density of the particle A at a distance $\boldsymbol{r}$ from a given point, $\varphi_B(\boldsymbol{r})$ is a density of the particle B at a distance r from a given point, φ_0 is total number density of segments, k is the compressibility of the system that is supposed to be sufficiently small, χ is the Flory-Huggins parameter which can be calculated based on the formula

$$\chi_{AB} = \frac{z_{CN}}{k_B T}\left[\frac{2u_{AB} - (u_{AA} + u_{BB})}{2}\right] \quad (2.2.6)$$

Here u_{AB} is pairwise interaction energy between a pair of neighbor lattice sites occupying by bead types of ***A*** and ***B***, z_{CN} is the coordination number, which is equal to 6 for the three-dimensional lattice. The interaction energies were set as $u_{AB} = -\varepsilon_{AB}$, where ε_{AB} is the Lennard-Jones parameter of interaction between the pair of the particles.

In order to obtain a coarse-grained density *φ(r),* the simulation box is divided into *ncell=nx*ny*nz* cells (where *nx, ny, nz* are number of cells in *x, y* and *z* directions). All the particles are distributed among these cells in the simulation box depending on their positions. According to the position of a given particle inside a cell, a fraction of it is assigned to the mesh points at the vertices of this cell (see Figure 2.1). The fraction of a particle assigned to a given vertex is proportional to the area of a rectangle whose diagonal is the line connecting the particle position and the mesh point on the opposite side of the cell. For instance, a fraction $(l-x)*(l-y)/l^2$ will be assigen to a mesh point **1**, and a fraction of $x*y/l$ at mesh point **4**, where *l* is a length of a side of the cell.

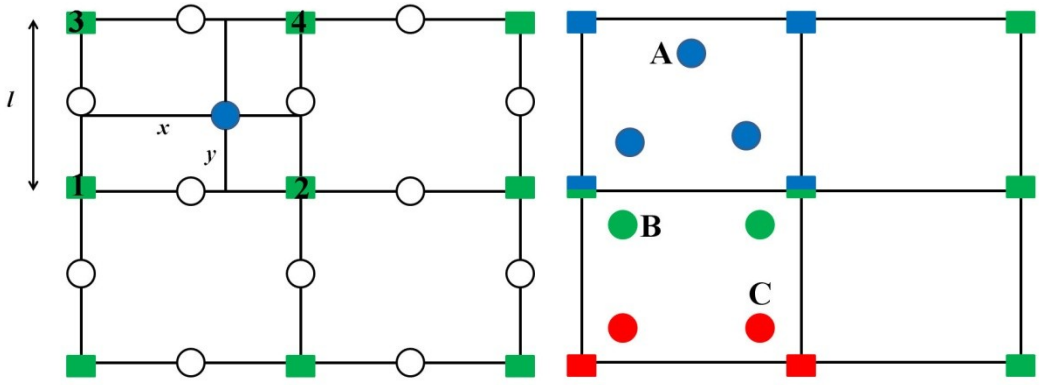

Figure 2.1: Particle fraction assignment for two-dimensional case (left); schematic representation of coarse-grained density in a box with a cell side length equal to *l*. The density of each bead is assigned to a mesh point in vertices of a cell (right). In blue are marked densities related to particles of type **A**, in green – densities for particles of type **B**, and in red – for particles of type **C**.

CHAPTER 2

2.3 MOLECULAR DYNAMICS AND HYBRID MD-SCF METHOD: SUMMARY

Classical MD simulation is the most widespread method used to perform calculations in order to predict the properties of materials. As mentioned before, this method is accurate and provides data considering all atom interactions. This is very useful tool to perform simulations at conditions that are not possible to perform by experiments. For example, to measure freezing point of water at 1 atmosphere is easy, but this becomes difficult to measure properties of real system at extreme conditions (high temperatures and pressures).[1] Classical MD simulations are very useful tool to perform qualitative analysis of the system. In particular, estimation of diffusion coefficient, calculation of radial distribution function, minimum distances between specific groups of atoms, analysis of secondary structure of the protein (peptide) can be performed by atomistic MD with high accuracy. This method is computationally expensive and requires more computational resources to investigate large scale systems (>100 nm) for a long computational time interval (>1μs). In this case particle-filed approach, based on combination of MD and SCF theory is a very useful and powerful tool. There are numerous applications of this approach for the study of block copolymers,[8-12] proteins,[13] polymer composites[14] and colloidal particles.[15-16] MD-SCF method, developed by Prof. Giuseppe Milano[7,17] in our research group at the University of Salerno, has already been successfully applied to study interactions and self-assembly of soft matters, as well as CNTs.

2.4 REFERENCES

(1) Frenkel, D.; Smit, B. *Understanding molecular simulation: from algorithms to applications*; Academic press, **2001**.

(2) Hockney, R. W.; Eastwood, J. W. *Computer Simulation Using Particles*; CRC Press, **1988**.

(3) Allen, M. P.; Tildesley, D. J. *Computer Simulation of Liquids*; Clarendon Press; Oxford University Press: Oxford [Oxfordshire], New York, **1987**.

(4) Berendsen, H. J. C.; Postma, J. P. M.; Vangunsteren, W. F.; Dinola, A.; Haak, J. R. *Journal of Chemical Physics* **1984**, *81*, 3684.

(5) Andersen, H. C. *The Journal of chemical physics* **1980**, *72*, 2384.

(6) Milano, G.; Kawakatsu, T. *The Journal of chemical physics* **2009**, *130*, 214106.

(7) Milano, G.; Kawakatsu, T. *Journal of Chemical Physics* **2009**, *130*.

(8) Drolet, F.; Fredrickson, G. H. *Physical review letters* **1999**, *83*, 4317.

(9) Matsen, M. W.; Schick, M. *Physical review letters* **1994**, *72*, 2660.

(10) Fredrickson, G. H.; Ganesan, V.; Drolet, F. *Macromolecules* **2002**, *35*, 16.

(11) Lauw, Y.; Leermakers, F.; Cohen Stuart, M. *The Journal of Physical Chemistry B* **2006**, *110*, 465.

(12) Ly, D. Q.; Honda, T.; Kawakatsu, T.; Zvelindovsky, A. V. *Macromolecules* **2008**, *41*, 4501.

(13) Dickinson, E.; Pinfield, V. J.; Horne, D. S.; Leermakers, F. A. *Journal of the Chemical Society, Faraday Transactions* **1997**, *93*, 1785.

(14) Balazs, A. C.; Singh, C.; Zhulina, E. *Macromolecules* **1998**, *31*, 8370.

(15) Roan, J.-R.; Kawakatsu, T. *The Journal of chemical physics* **2002**, *116*, 7283.

(16) Roan, J.-R.; Kawakatsu, T. *The Journal of chemical physics* **2002**, *116*, 7295.

(17) Milano, G.; Kawakatsu, T. *The Journal of chemical physics* **2010**, *133*, 214102.

CHAPTER 3:

Theoretical Study of the Coating Mechanisms of Single-walled Carbon Nanotube by Poloxamer based Surfactants

CHAPTER 3

THEORETICAL STUDY OF THE COATING MECHANISM OF SINGLE-WALLED CARBON NANOTUBE BY POLOXAMER BASED SURFACTANTS

3.1 ABSTRACT

The coating mechanism of single – walled carbon nanotube (SWCNT) by poloxamer based surfactants has been studied by molecular dynamics (MD) simulations. Aqueous solutions, consisting of the mixture of 1,2 – dimethoxyethane (DME) and 1,2 – dimethoxypropane oxide (DMP), pure polyethylene oxide (PEO) and polypropylene oxide (PPO) pentamers and their mixtures, as well as, L64 triblock copolymer were considered in this study. The results of the simulation suggest the preferential bindings of the DMP/PPO with respect to the DME/PEO onto the surface of the SWCNT. Binding of L64 triblock copolymer to CNT occurs, mainly, by PPO blocks, while PEO blocks tend to remain into water. Interestingly, it was found that CNTs coated by L64 do not prevent the formation of CNT aggregates. This result is in agreement with experimental observations on the poor capability of L64 polymers to disperse CNT in solution.

CHAPTER 3

3.2 INTRODUCTION

Carbon nanotubes show a peculiar ability to cross biological membrane and cumulate in the cell.[1] This characteristic, together with other properties of this material, offers interesting alternatives for developing novel delivery system in therapy and in diagnostics.[2-3] However, this potential use is mainly limited by their poor solubility in water. In fact, new synthesized single-walled carbon nanotubes aggregate in bundles that are difficult to separate.[4] Different solutions based on the CNT surface modification have been proposed to overcome this problem. For possible biomedical applications, these CNT derivatives should not only improve the CNT solubility, but also sustain biocompatibility and low toxicity. The surface modifications of CNTs can be accomplished by covalently bound functional groups[5] and/or by non-covalently coating the surface with surfactants or, in general, amphipathic molecules like lipids and polymers.[6] In particular, block copolymers have been successfully utilized for modifying the solution behaviour of these nanomaterials. In fact, these amphipathic polymers are able to disperse nanostructures and colloidal moieties in different media in order to induce their assembly into mesostructures.[7-9] Nevertheless, the details of this process are not yet clarified. In a recent study on the adsorption of block copolymers to SWCNTs and MWCNTs, a non-wrapping mechanism - which means that interactions between the polymer and the nanotube are nonspecific[10] - was proposed. In particular, the more hydrophobic PPO blocks are adsorbed onto nanotube surface, while more hydrophilic PEO parts are extending into aqueous media, providing steric repulsion, which results on dispersion of the CNT. Granite et al.[11] investigated interactions between block copolymers and SWCNTs in aqueous solutions, using small-angle neutron scattering studies. In this study, two types of block copolymer-CNT interaction models have been suggested. The first one implies core-chain model, where polymer chains are adsorbed onto the small bundle surface and there is no difference between PEO and PPO components. The second one, more detailed, describes core-shell-chains model. In this model the core is the CNT bundle, the shell is region in contact with the CNT surface in which the PPO part of the polymer is adsorbed and chains are constituted by the PEO part of the polymer extending in the solvent. More recently, Frise and coworkers[12] have studied the interaction between the block copolymer F127 and CNT in aqueous dispersion by pulsed-field gradient (PFG) ^{1}H NMR spectroscopy. Their study confirmed the previous hypothesis showing that the polymer binds the nanotube by its central hydrophobic block, while the two hydrophilic PEO terminal parts extend into water phase.

CHAPTER 3

Different theoretical study using MD simulations was also performed to investigate the "wrapping" mechanism of the nanotube by polymer chains. Yang *et al.*[13] has studied the interaction of different polymers with CNT. The polymers considered in the work were polystyrene (PS), poly(phenylacetylene) (PPA), poly(p-phenylvinilene) (PPV), and poly(m-phenylenevinilene-co-2.5-dioctyloxy-p-phenylenevinilene) (PmPV). "Zig-zag" CNTs with the length of 10.38 nm and diameters ranging from 0.39 to 5.36 nm were used for the study. The results evidenced for all the polymers the tendency to coat the CNT surface. However, the strength of the interactions is very dependent by the structure of polymer monomers. In particular, polymers as PPV and PmPV, consisting of monomers with aromatic groups in the backbone, tend to bind the CNT surface stronger than those, containing the aromatic groups in their side chains, such as PS and PPA.

To the best of our knowledge, no theoretical studies have been performed to specifically study the interaction mechanism of linear ether based polymers with SWCNT in aqueous solutions. In this chapter a theoretical study, based on atomistic MD simulations, of SWCNT in the presence of surfactants is reported. In particular, the coating mechanism of SWCNTs by polyethylene oxide (PEO) and polypropylene oxide (PPO) based polymers and block copolymers has been studied. The study is divided in two parts. In the first part, simulations of DME/ and DMP/water mixtures with SWCNTs of different chiral indices are analyzed. Since DME and DMP represent one monomer of the PEO and PPO polymers, respectively, these simulations can provide a detailed model of the interactions between the single polymeric units and the CNT. The SWCNTs of different chiral indices are used to understand the effect of the surface curvature and tube diameters on the bindings and permeations of the polymer into the nanotube. In the second part, the influence of the polymer length on the preferential solvation has been investigated with pentameric PEO and PPO chains and with the triblock co-polymer L64 (see Scheme 1). Finally, the effect of L64 on CNT bundle formation has been studied.

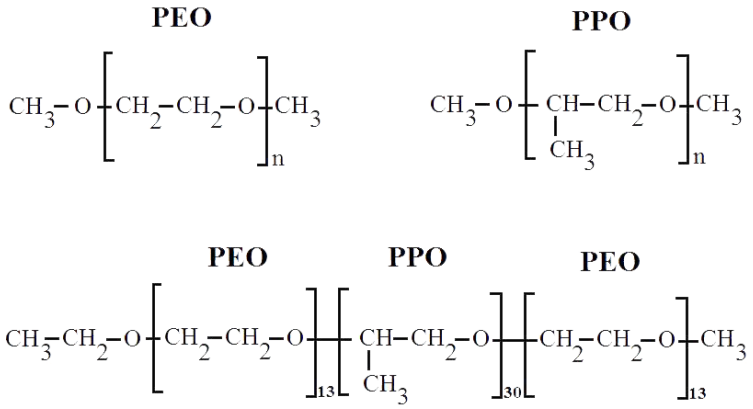

Scheme 1: Chemical formulas for PEO, PPO pentamers (n=5) and L64 triblock copolymer (bottom) used in this study.

3.3 COMPUTATIONAL METHODS

3.3.1 CNT Models.

Carbon nanotubes of different length and chiral indices (m, n) have been used to perform simulations. Namely, nanotube with chiral indices m=10, n=5 (chiral), m=7, n=7 (arm-chair), m=5, n=5 (arm-chair) and m=5, n=0 (zig-zag). The length was chosen to be equal to 3 nm for all simulations. The SWCNTs used in these simulations are without explicit hydrogens at the edges. Since CNTs, described in experimental work are quite long (about 500 nm[11]), the charges at both edges of CNT should not affect the interactions. Table 3.1 contains a list of SWCNTs used in this study with the corresponding diameters and chiral indices.

3.3.2 CNT Force Field.

The CNT force field is based on the model proposed by Walther et al.[14] The carbon atoms were considered uncharged. The Lennard-Jones (LJ) parameters for carbon-carbon interaction of nanotube ε_{cc} was chosen to be 0.4396 kJmol^{-1} and σ_{cc} – 0.3851 nm[14], LJ parameters of interaction between the carbon of the nanotube and oxygen of the water are ε_{co} = 0.392 kJmol^{-1} and σ_{co} = 0.319 nm.[15] The mixed Lennard-Jones parameters for the interaction of the CNT carbon with other atoms were obtained using the combination rules[16]:

$$C_{ij}^{(6)} = \sqrt{C_{ii}^{(6)} * C_{jj}^{(12)}} \qquad C_{ij}^{(12)} = \sqrt{C_{ii}^{(12)} * C_{jj}^{(12)}} \tag{3.1}$$

Where symbols *i* and *j* are related to particle types. Here $C_{ij}^{(6)}$is the LJ parameter of interaction between the particles of type *i* with the particle of type *j*. The parameters $C_{ii}^{(6)}$and $C_{jj}^{(12)}$are the LJ parameters of interactions between the particles of type *i* with a particle of type *i*, and the particle of type *j* with the particle of type *j*, respectively.

3.3.3 Polymers Force Field.

The models of DME, DMP, PEO, PPO and Pluronics were developed in our research group and the detail of the model have been recently published[17].

Table 3.1: Chiral indices of SWCNT and corresponding diameters.

Chiral indices (m,n) of CNT	Diameter, nm
10, 5	1.2
7, 7	0.94
5, 5	0.6
5, 0	0.4

3.3.4 Simulation System Setup.

The systems were prepared centring the solute, the SWCNT, in a box of suitable size and filling the empty space with the surfactants and the water molecules. In Table 3.2, detailed information of simulated systems is reported.

3.3.5 MD Simulations.

All the simulations were performed at constant temperature and pressure (NPT conditions). The integration time step was chosen to be 2 fs. The temperature and pressure were maintained to the reference value (T=298 K, P=1bar) using the Berendsen thermostat and barostat with coupling time constant of τ_T=0.1 ps for temperature and τ_p=0.5 ps for pressure, respectively. Simple Point Charge (SPC/E) model was used as water model.[18] Electrostatic interactions were maintained by applying a cutoff of 1.4 nm. The Lennard-Jones interactions were calculated using a cutoff of 1.4 nm. All the systems were energy minimized using the steepest descent algorithm and subsequently simulated

for a minimum of 25 ns for the DME/DMP mixtures up to 100 ns for the three CNTs wrapped by L64 triblock copolymers.

Table 3.2: Summary of the simulated systems. In the system name S corresponds to SWCNT and the numbers in parenthesis indicate the chirality.

System	Simulation length, ns	Box side size, nm^3	Water mol.	DME/ PEO chains	DMP/ PPO chains	L64 chains
S(10,5)DME:DMP	25	5.5	5196	23	24	-
S(7,7)DME:DMP	25	5.5	5202	23	24	-
S(5,5)DME:DMP	25	5.5	5196	23	24	-
S(5,0)DME:DMP	25	5.5	5212	23	24	-
S(5,5)PEO_5	75	10.0	32864	15	-	-
S(5,5)PPO_5	75	10.0	32773	-	15	-
S(5,5)PEO_5:PPO_5	75	10.0	32846	7	7	-
S(5,5)L64	75	10.0	32192	-	-	6
3S(5,5)	60	4.5	2751	-	-	-
3S(5,5)L64	100	10.0	31716	-	-	12

3.3.6 Analysis of the Trajectories.

The distribution of the solvent and surfactants around the CNT was analysed using cylindrical radial distribution function (cRDF), cumulative coordination numbers and spatial density distribution functions (SDF). The last one was used to provide a tridimensional representation of the averaged distribution of the surfactant and solvent molecules around the CNT. The SDF distributions were calculated as follows. The simulation box along the trajectories was centred on the solute using translational-rotational fit to the first configuration of the MD trajectory and by unfolding the trajectory to remove the periodic boundary conditions. Finally, the atomic positions of the selected atoms of the solvent or surfactant molecules were mapped on a cubic grid centred on the geometric centre of the reference solute and averaged with respect to the number of frames analysed. A cubic grid with 0.1 nm grid spacing was used for all calculations. The averaged volumetric density data obtained was visualized and analysed using program VMD.[19]

cRDF of the solvent or surfactant molecules with respect to the surface of the SWCNT was calculated with a program developed in the group of Prof. Roccatano at Jacobs University Bremen. cRDF's were calculated using cylindrical coordinate system (r, φ, z), with origin at the center of

mass of the SWCNT. Here r is a radial distance from the center of the nanotube, φ azimutal angle; z is z axis of the nanotube. The interior region of the CNT is defined as the volume V_0 of a cylinder of height h given by the nanotube length, and with a base of diameter d_0 equal to $V_0 = \frac{\pi}{4} d_0^2 h$. The volume of the CNT shell is defined by the volume of the hallow cylinder of radius r around the CNT external surface equal to $V_{hc} = \frac{\pi}{4} r^2 h - V_0$. Solute molecule is considered to be inside the nanotube or in the shell region if its center of mass is located inside the one of the above-defined volumes. The cRDF function is, hence, defined as

$$cRDF(r) = \frac{N(r+\Delta r, h/2) - N(r, h/2)}{2\pi r h \Delta r} = \frac{1}{2\pi n r h} \frac{\partial}{\partial r} N(r, h/2) = \frac{1}{n} \langle \rho(r, \varphi, z) \rangle_{\varphi, z}, \qquad (3.2)$$

Where Δr is a small increment of the radial distance, $\langle \dots \rangle_{\varphi,z}$ is and average over φ $(0 \leq \varphi < 2\pi)$ and z $(-h/2 \leq z \leq h/2)$ at given r. Similarly with the spherical radial distribution function in our case $cRDF(r)$ is normalized in such a way that $cRDF(r) \to 1$ as $r \to \infty$.

Finally, the number of molecules inside the cylindrical volume $N(r, z)$, extending form $z' = -z$ to $z' = z$, with a base of radius r is related to local number density of solute molecules, $\rho(r, \varphi, z)$, through the formula

$$N(r, z) = \int_0^r \int_0^{2\pi} \int_{-z}^{z} r' dr d\varphi dz' \rho(r', \varphi', z') \qquad (3.3).$$

The diffusion coefficient was calculated using the Einstein's relation:

$$\lim_{t \to \infty} \langle \| \boldsymbol{r_i}(t) - \boldsymbol{r_i}(0) \|^2 \rangle = 6Dt \qquad (3.4).$$

Where D is the diffusion coefficient, $\boldsymbol{r_i}(t)$ is the position of the center of mass of i-th molecule, taken at time t, and $\boldsymbol{r_i}(0)$ the position at time 0.

MD simulations and analysis of the trajectories were performed using GROMACS (version 4.5.5) software package and the visualization software VMD.[19]

CHAPTER 3

3.4 RESULTS AND DISCUSSION

3.4.1 SWCNT in DME and DMP Mixture.

The coating effect of DME and DMP on the CNT surface was analysed using the cRDF of the solvent molecules with respect the CNT surface. In Figure 3.1 the cRDFs for the DME and DMP molecules, multiplied for the distance, are reported. The curves have two peaks located at the distance of 0.05 nm and the second one at 0.3 nm from the surface of CNT in both cases. The first peak is due to the molecules inside the carbon nanotubes. The second peak represents the molecules cumulated on the external surface of the CNT.

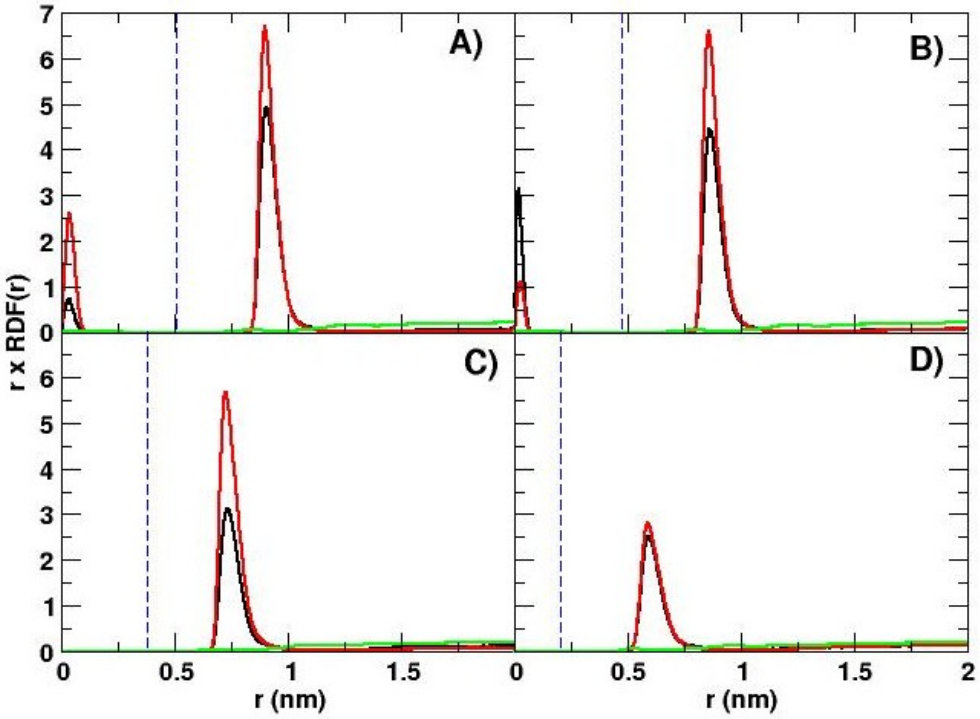

Figure 3.1: cRDF (multiplied by r) for DME (black), DMP (red) and water (green) molecules respect to the surface of SWCNT with chiral indices A) (10,5), B) (7,7), C) (5,5) and D) (5,0). The dashed vertical lines indicate the radius of the SWCNT.

For all the cases, the higher peaks for the DMP indicate its larger local density on the surface of the CNT with respect to DME molecules. Furthermore, the rapid decrease of the cRDF curves with the increase of the distance from the CNT indicates that most of the molecules of DME and DMP aggregate around the SWCNT.

In Figure 3.2, plots of cumulative coordination numbers as function of the distance from the CNT surface and, in Table 3.3, the numbers of DME and DMP molecules within 1.0 nm from the surface of the SWCNT are reported. As expected, from the more hydrophobic nature of the DMP than DME,[17] the number of DMP molecules at different distances from the CNT surface is larger (see Figure 3.2). In particular, at 1.0 nm from the CNT axes, the ratio DMP/DME varies from 1.1 to 1.8 depending on the size and the chirality of the CNT. The larger ratios is observed for (10,5) and (5,5) CNTs.

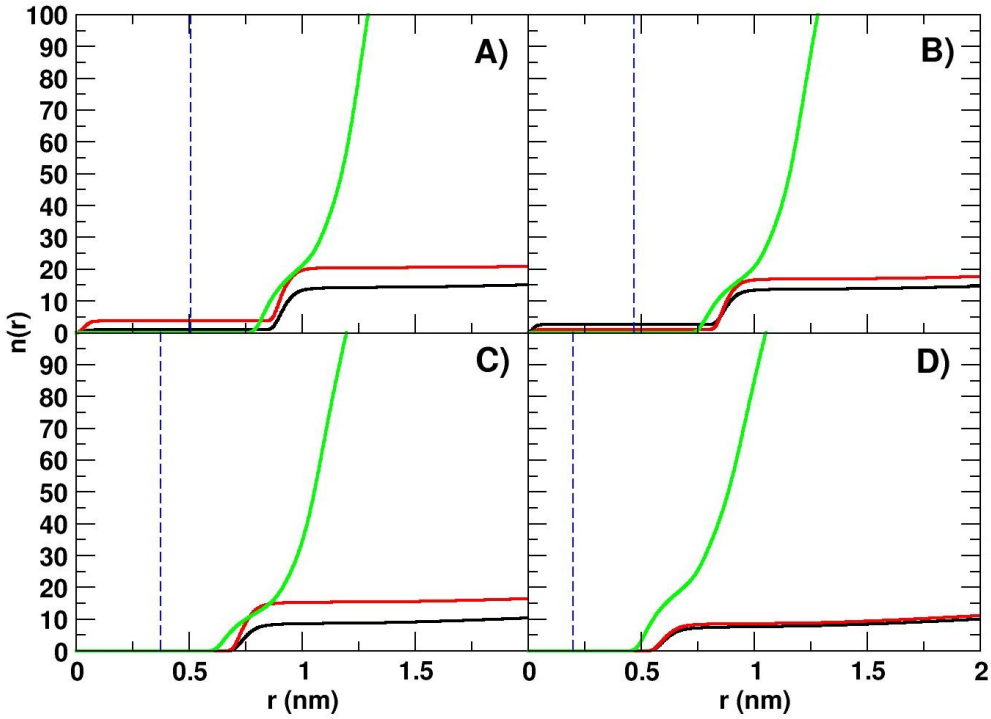

Figure 3.2: Plots for the cumulative numbers of molecules of DME (black), DMP (red) and water (green) from the surface of the SWCNT with chiral indices A) (10, 5), B) (7,7), C) (5,5) and D) (5,0), respectively. The dashed vertical lines indicate the radius of the SWCNT.

The change of the number of DMP molecules within 1.0 nm vs. the CNT diameter is less rapid (see Table 3.3). The CNT (10,5) and (7,7) show the presence of both DME and DMP in the interior of the CNT. For the (10,5), an average of 4.6 molecules are present in the CNT and the number of DMP is larger than DME. The CNT (7,7) contains an average of 3.6 molecules but in this case DME molecules are more abundant than DMP (DMP/DME=0.34 in Table 3.3). Water molecules do not diffuse inside the CNTs in all the four cases.

Table 3.3: Cumulative numbers for DME and DMP inside the CNT (**In**) and within a distance of 1.0 nm (**Out**) from the CNT axes.

CNT chirality	N° DME		N° DMP		DMP/DME	
	In	Out	In	Out	In	Out
(10,5)	0.9 ± 0.9	13.3 ± 3.6	3.7 ± 1.9	19.7 ± 4.4	3.9	1.5
(7,7)	2.6 ± 1.5	13.4 ± 3.6	1.0 ± 0.9	16.6 ± 4.0	0.4	1.2
(5,5)	0	8.6 ± 2.9	0	15.3 ± 3.8	/	1.8
(5,0)	0	7.6 ± 2.7	0	8.6 ± 2.6	/	1.1

In Figure 3.4 the normalized distributions of the molecules inside the CNT (10,5) and (7,7) are reported. Both DME and DMP molecules distribute with regular patterns. For the CNT (10,5) 2 DME peaks are observed inside the CNT and other 4 on both ends. DMP distribution shows 5 peaks inside the CNT and 2 small one outside the borders. The peak position is similar to the DME ones. An additional peak at R=0 is observed in this case but for the DME. As from the values in Table 3.3, the density of DME molecules is lower than DMP. For the CNT (7,7) the peaks for DME and DMP are in the same number (4 inside and 2 outside the CNT) and at the same locations, but situation is the opposite, and the density is higher for the DME than DMP as expected from the average number of molecules observed in the CNT (see Table 3.3).

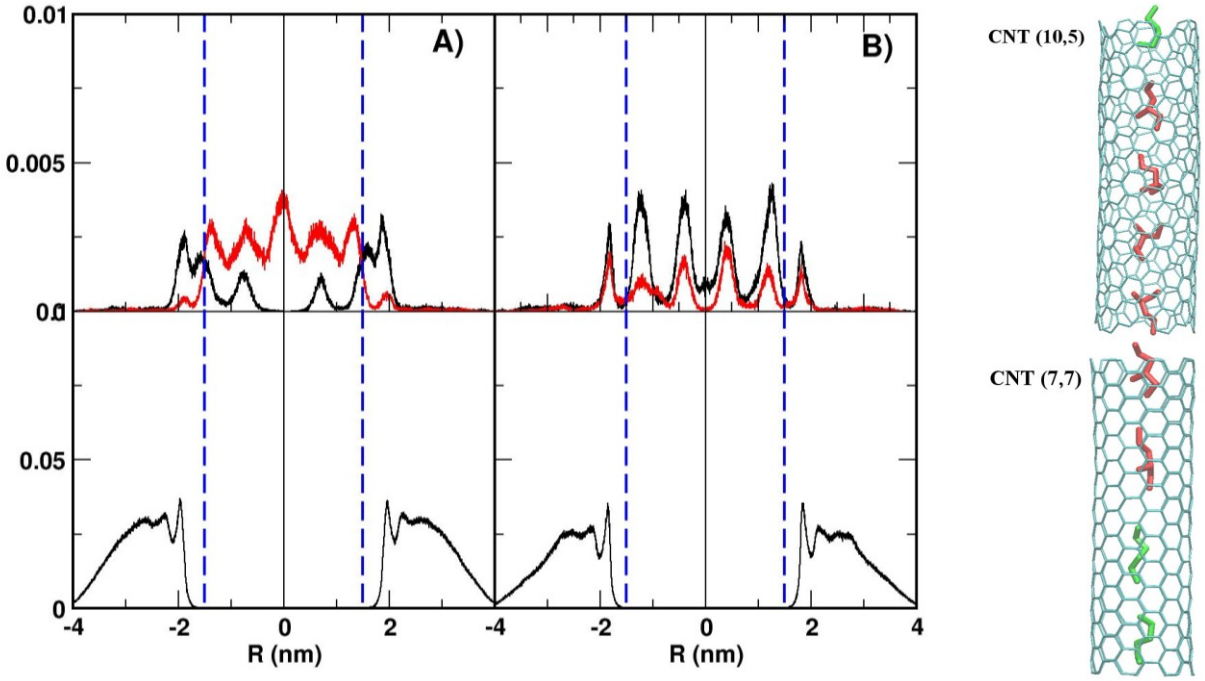

Figure 3.3: Longitudinal distribution of DME, DMP (top graphs, black and red lines, respectively) and water (bottom graph) molecules distributed inside the CNT with chiral indices A) (10, 5) and B) (7,7), respectively. The dashed lines indicate the CNT boundaries. At the right side are shown DME (green) and DMP (red) molecules inside the CNT (10, 5) and CNT (7, 7).

In Figure 3.4 A the SDFs for DME and DMP for the chiral CNT (10,5) are reported. The averaged distributions are coloured in green, red and blue for DME, DMP water, respectively. As it can be noticed from the picture, most of the DMP densities are distributed around the surface of nanotube, with blobs inside the CNT.

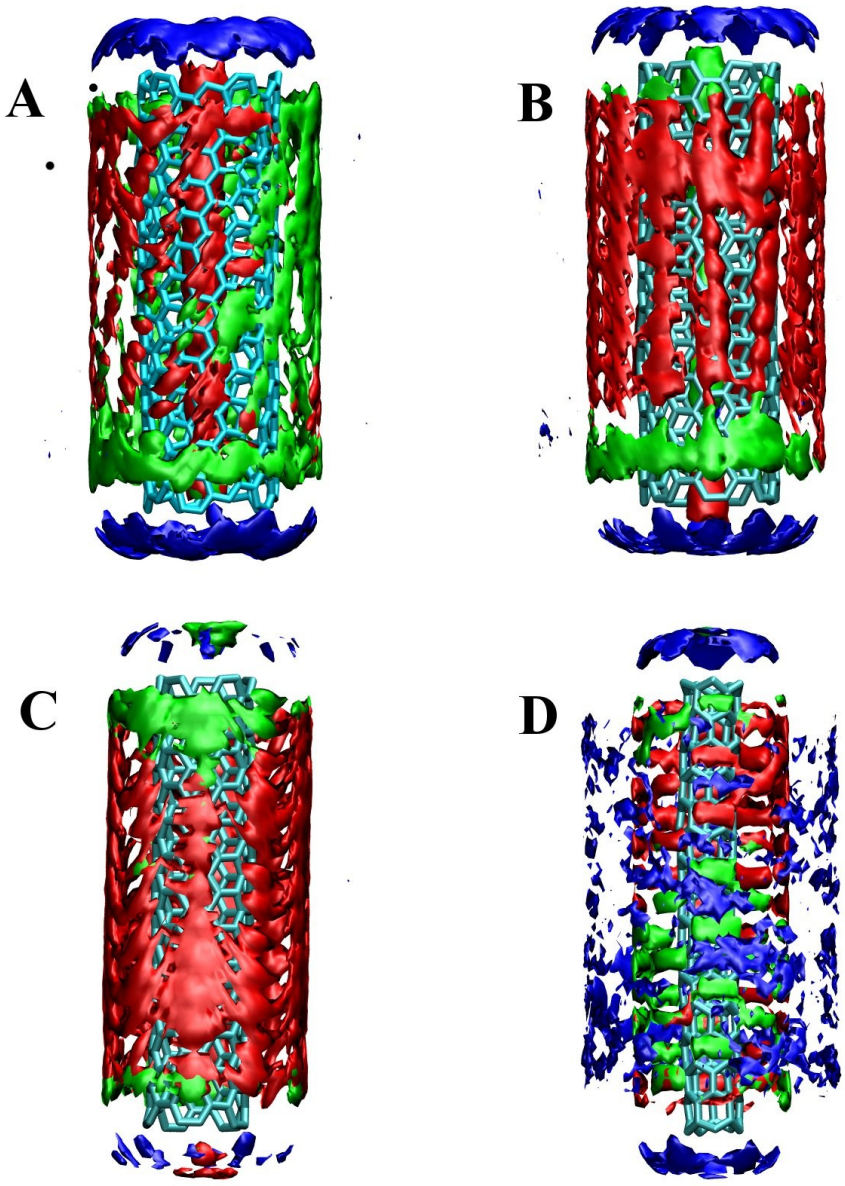

Figure 3.4: SDF for DME and DMP distribution around the CNTs A) (10,5), B) (7,7), B) (5,5) and D), (5,0), respectively. Density distributions are shown in green for the DME, in red for the DMP, and in blue water molecules.

As for water molecules, they are mostly accumulated at both edges of the nanotube. The arm-chair CNT (7,7) surface (see Figure 3.4 B) is tightly wrapped by the DMP molecules that reduce the access to both DME and water molecules. The DME and DMP molecules distribute only outside the arm-chair CNT (5,5) and zig-zag (5,0) (see Figure 3.4 C and D) and, as before, the DMP molecules are closer to the surface than DME.

The values of diffusion coefficients (D) calculated for DME, DMP and water molecules in the simulation box are presented in Table 3.4. For comparison, diffusion coefficients for water, DME and DMP without presence of CNT are given.[17] It is evident from the values that the diffusion coefficients for DME and DMP are lower in the presence of the CNT than in its absence. As expected, the binding of the DMP and DME on the surface of the CNT decreases their diffusion coefficients. Furthermore, the values of DMP are lower than DME. The lowest values for both DME and DMP are observed for the CNT (10,5). With the exception of the CNT (5,0) the value of DMP remains lower as for the CNT (10,5) while for the DME the value remains close to 0.85×10^{-5} cm^2/s. The D values for the water molecules are very similar to the pure solvent.

Table 3.4: Diffusion coefficients for DME, DMP and water molecules with and without presence of SWCNT

D, $cm^2/s \times 10^{-5}$	No CNT	CNT (10,5)	CNT (7,7)	CNT (5,5)	CNT (5,0)
D_{DME}	1.68 ±0.13	0.33±0.18	0.83±0.02	0.90±0.08	0.83±0.05
D_{DMP}	1.54±0.29	0.23±0.07	0.23±0.20	0.33±0.09	0.78±0.001
Water	3.31±0.06	3.35±0.03	3.32±0.01	3.23±0.06	3.2±0.03

3.4.2 Coating of the SWCNT by PEO and PPO pentamers.

In Figure 3.5, the cumulative numbers for PEO and PPO molecules as function of the distance from central axes of CNT are reported. The curves of the cumulative numbers increase with the distance for pure PEO (Figure 3.5 A) and pure PPO (Figure 3.5 B), as well as, PEO/PPO mixtures (Figure 3.5 C). The curves reach their first maximum ~0.6 nm and then keep increasing slowly. In Table 3.5 the cumulative numbers for pure PEO and PPO, as well as, for PEO/PPO mixtures, calculated within the distance of 1 nm from the central axes of CNT, are reported. These numbers for pure

PPO is slightly higher than for the pure PEO. However, for 50:50 PEO and PPO mixture (see Figure 3.5 C) the behaviour of curves is in vice-versa, compared to the pure liquids.

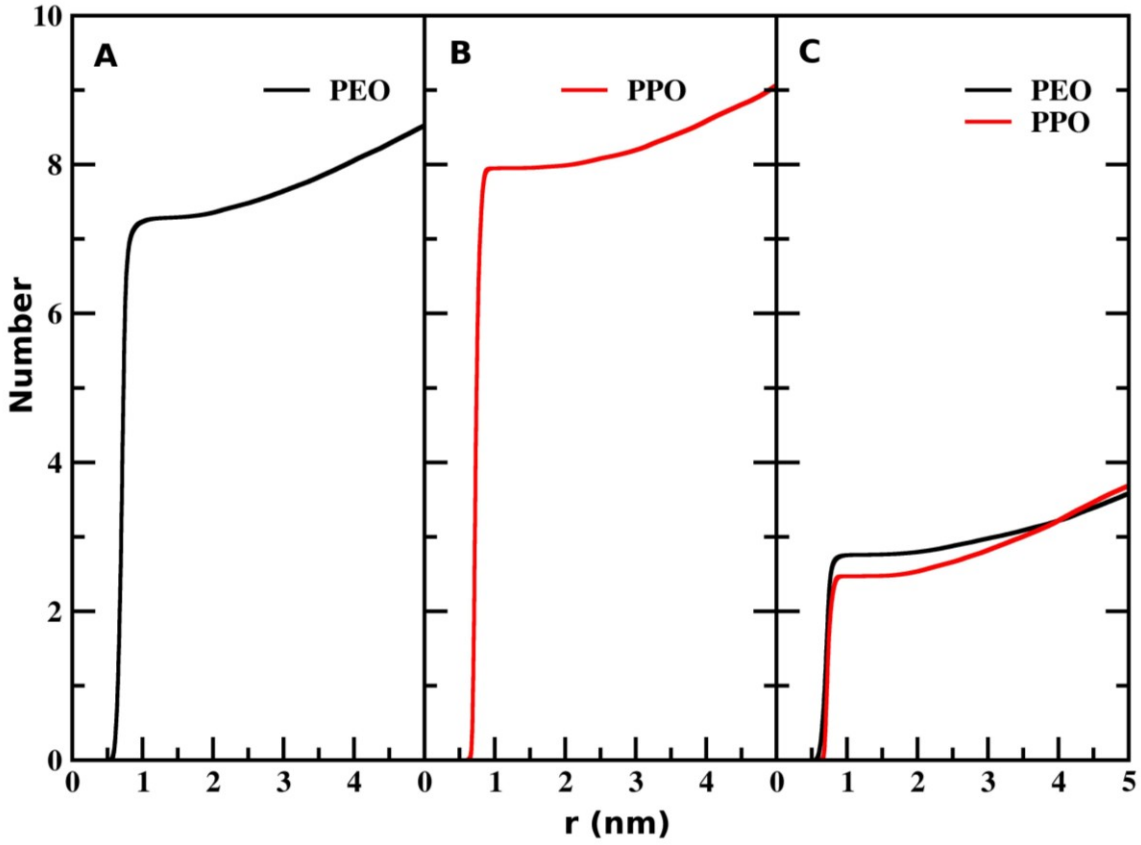

Figure 3.5: Plots for the cumulative numbers of molecules as function of the distance for A) pure PEO, B) pure PPO pentamers and for their C) 50:50 PEO:PPO mixture.

Table 3.5: Cumulative numbers for PEO, PPO and PEO/PPO mixtures within 1 nm from the central CNT axes.

N^o PEO	N^o PPO	N^o PEO/ N^o PPO
7.2±2.6	8±3	2.7±1.7/2.4±1.6

Figure 3.6 shows the spatial density distributions around the CNT (5,5) for the pentamers of PEO, PPO and 50% mixture of PEO:PPO chains in water. For both, pure PEO and PPO chains solutions, pentamers are coating the nanotube surface, preventing the water molecules to be in contact with a surface of CNT with slightly higher preferential bindings of PPO compared to PEO chains. As for the mixture of PEO:PPO chains, the there are no significant preferences between the PEO and PPO chains in terms of binding mode to the CNT surface. Similarly with the case of simulation of DME

and DMP containing aqueous solutions, here water molecules are also cumulated at the edges of the nanotube, thus, minimizing the contact with hydrophobic surface of CNT.

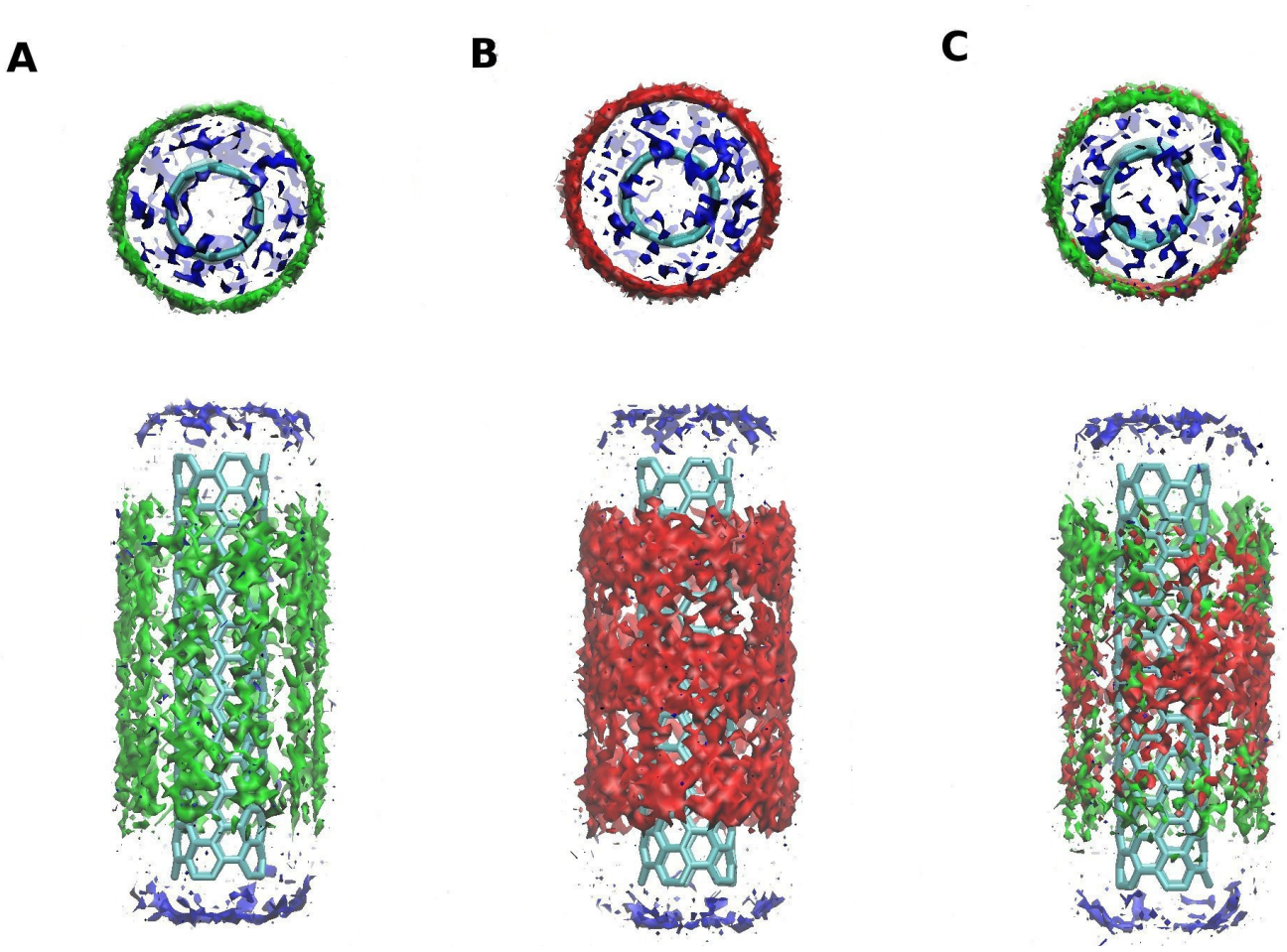

Figure 3.6: Different views of the SDF for PEO and PPO pentamers wrapping the surface of CNT (5,5) with PEO – A, PPO - B and 50:50 PEO:PPO mixture – C. PEO is shown in green, PPO in red, and water in blue.

3.4.3 Interaction of L64 triblock copolymer with SWCNT

In Figure 3.7, snapshots of the simulation of L64 triblock copolymer in the presence of SWCNT (5,5) at initial configuration (A) and configuration at 75 ns (B and C) are reported. For clarity, water molecules are omitted. The hydrophilic blocks of L64 (PEO) are shown in green, the hydrophobic

blocks (PPO) – in red. During the simulation four L64 chains out of six have been wrapped around the CNT by their hydrophobic PPO block, while hydrophilic PEO blocks were extending into water (Figure 3.7, B and C). This result is in a good qualitative agreement with experimental data, indicating that amphiphilic molecules, like polymers, are coating the surface of nanotube by their hydrophobic PPO parts and extending the hydrophilic PEO chains into the aqueous media.[11-12]

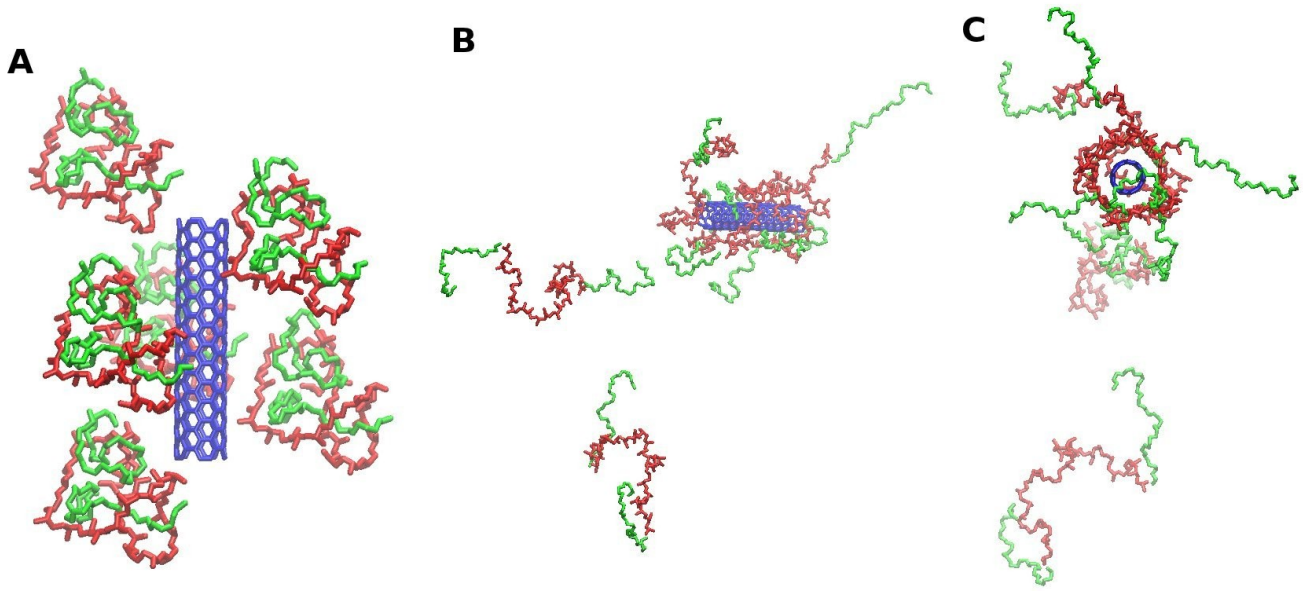

Figure 3.7: L64 triblock copolymer wrapping around SWCNT (5,5). A- initial configuration. B and C - different views of the configuration at 75 ns.

3.4.4 Effect of Polaxamers on the CNT Bundle Formation

Bundle consisting of three SWCNT of 3 nm has been obtained after 80 ns placing nanotubes into simulation box, filled with water molecules (see Figure 3.8 A and B). In Figure 3.9 are shown minimum distances between the first, second and third nanotube for the last 10 ns – at which the bundle is stably aggregated. Three CNTs form a triangularly arranged bundle with an average minimum distance of 0.36 nm, corresponding to the equilibrium carbon-carbon LJ contact.

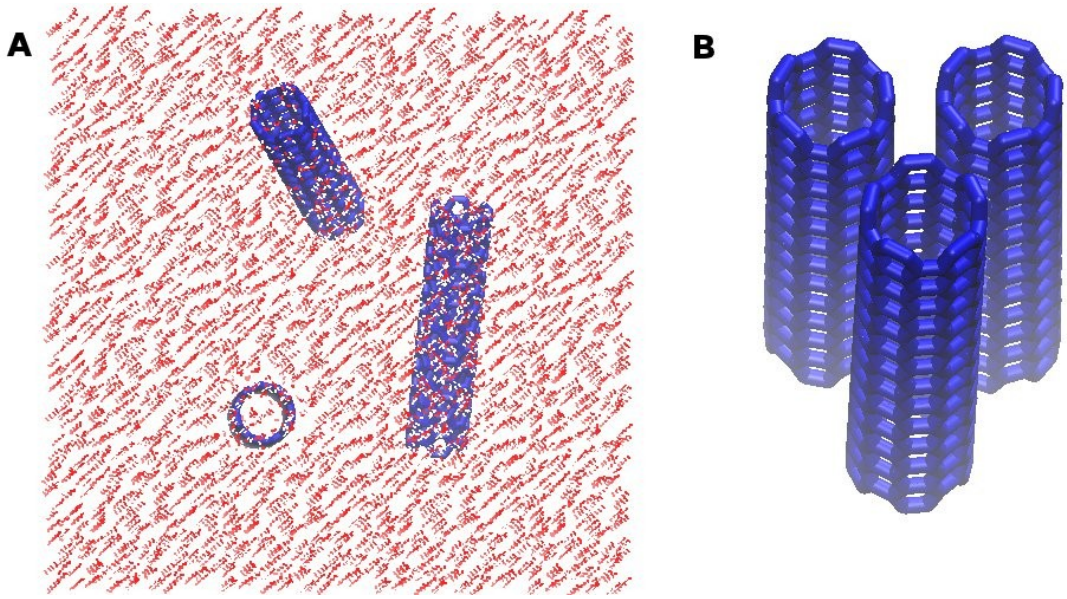

Figure 3.8: SWCNT bundle formation. A- initial configuration; B- configuration after 80 ns.

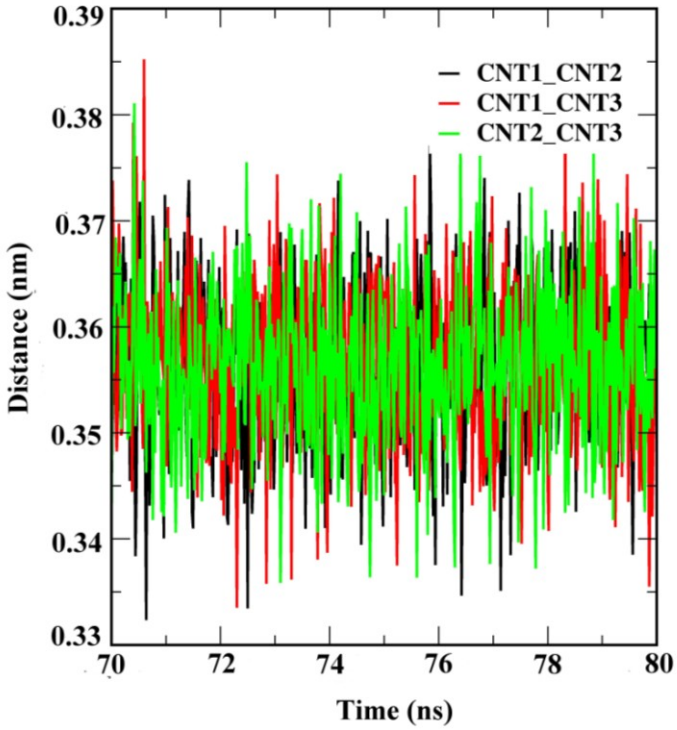

Figure 3.9: Minimum distances between CNT1, CNT2 and CNT3 for the last 10 ns. Bundle formation.

Since block copolymers are known to disperse CNTs in aqueous solutions,[10-11,20-21] a simulation study was carried out to understand if L64 triblock copolymers affect the aggregation processes observed for the uncoated CNTs. Figure 3.10 A shows the starting configuration of the simulation with three CNTs having the surface covered by triblock copolymers into a water box. After 1 ns of simulation, two out of three CNT start to aggregate and remained aligned for the rest of the simulation (see Figure 3.10 B). This phenomenon may become clear if one refers to the minimum distances between the nanotubes, shown in Figure 3.11. It is evident from Figure 3.11 that CNT1 and CNT2 start to aggregate at the beginning of simulation, the distance between these two nanotubes becomes ~0.3 nm, which corresponds to the distance between the nanotubes in aggregated (bundle) state (see Figure 3.9). CNT3 starts to be in contact with CNT1 at 10 ns till the end of the simulation, however, the distance between CNT2 and CNT3 fluctuates with a contact corresponding to 57-72 ns. In addition, from Figure 3.10 it is observable that some chains of L64 are detached from the CNT surfaces permitting their contact and alignment. This result is in accordance with experimental work performed by the group of Xin.[22] In particular, they have studied the dispersion of the nanotube by different amphiphilic block copolymers, such as F127, the starlike block copolymer AP432 and L64, using by UV-VIS-NIR measurements and Raman spectroscopy techniques.[22] In their work, it was observed that F127 (and AP432) has good capabilities to disperse CNTs, while L64 was unable to produce a good dispersion. They have explained this phenomenon with the shorter hydrophilic (PEO) chains of L64 in comparison to the F127 (and AP432 one), which accounted for the weak steric repulsion between the individual nanotubes in the CNT bundles.

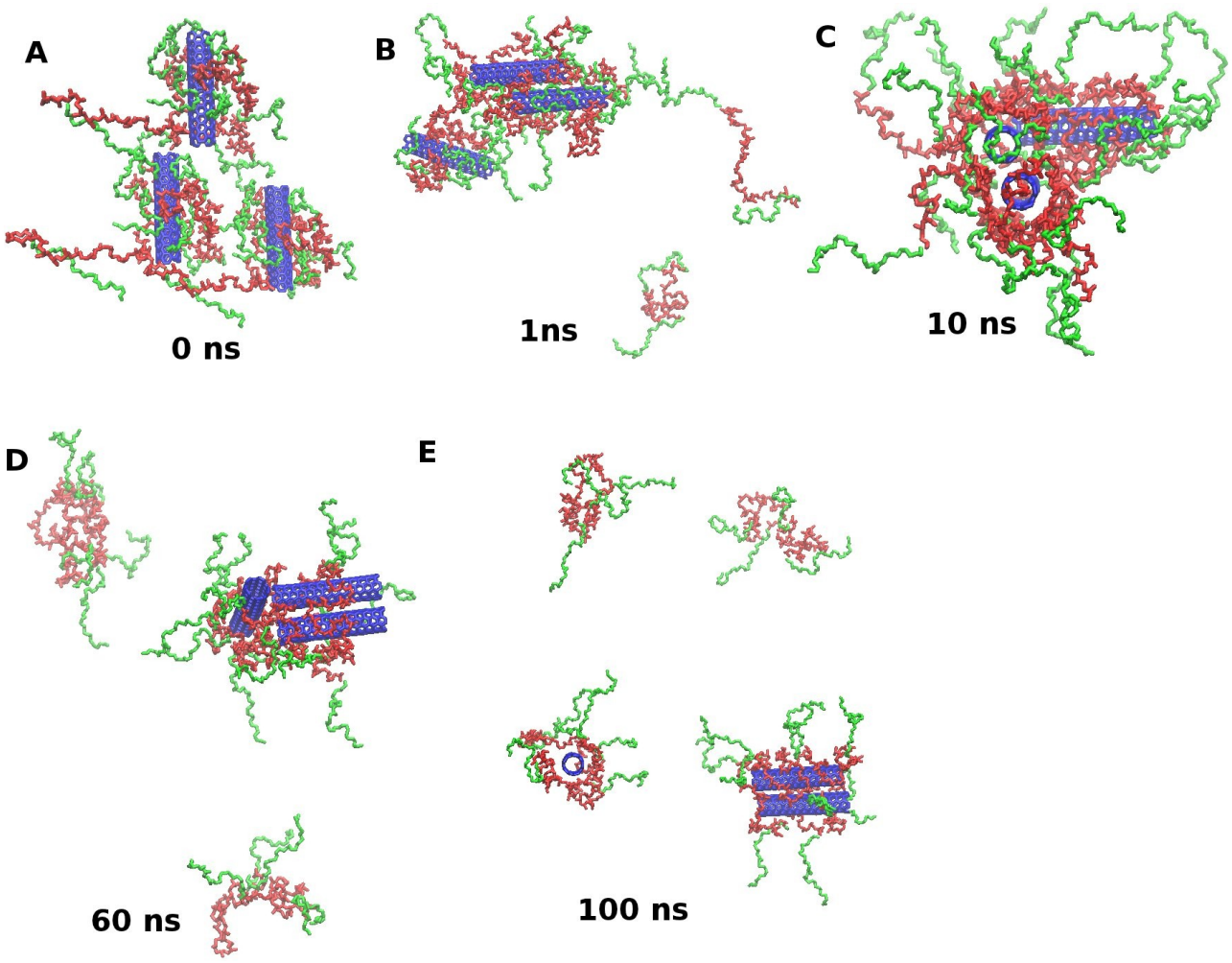

Figure 3.10: Solvation of three SWCNT (5, 5), wrapped by L64 triblock copolymer in a water (water molecules are omitted for clarity). A- initial configuration; B, C, D and E configurations at 1, 10, 60 and 100 ns, respectively.

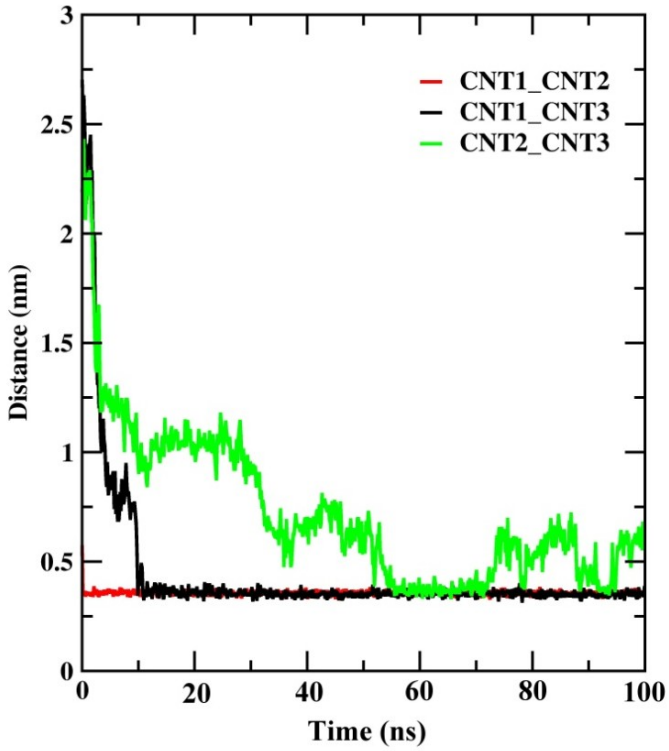

Figure 3.11: Minimum distances between the CNT1, CNT2 and CNT3, surface of which is coated by pluronic L64.

CHAPTER 3

3.5 CONCLUSIONS

Atomistic MD simulations have been performed to study the interaction of the linear ether based polymers with SWCNT. Based on the results of simulations, it has been found that DMP molecules tend to distribute closer to the surface of CNT rather than DME molecules. This effect seems not depending by the chirality of nanotube, but by the size. In particular, both DMP and DME (but not water) diffuse and organize inside the larger CNT (10,5) and (7,7). No molecule was observed in the smaller CNTs used in this study. Similar to DMP molecules, PPO pentamers preferentially coat the CNT surface compared to the PEO pentamers in pure solutions, whereas, in their mixtures the binding mode is slightly higher for PEO rather than for PPO chains. The results of simulation with triblock copolymer L64 had shown that the polymer chains wrapped the nanotube by the part consisting of PPO blocks, while the part, consisting of PEO blocks were extending in a water phase. And finally, it was shown that coating by L64 the surface of SWCNT is not stable in water solution. The detachments of the chains takes place, which results in aggregation of the nanotubes. This last result is in agreement with experimental one that shows weaker capability of the Pluronic L64 to disperse CNT bundles.

3.6 REFERENCES

(1) Porter, A. E.; Gass, M.; Muller, K.; Skepper, J. N.; Midgley, P. A.; Welland, M. *Nature Nanotechnology* **2007**, *2*, 713.
(2) Prato, M.; Kostarelos, K.; Bianco, A. *Accounts of chemical research* **2007**, *41*, 60.
(3) Bhirde, A. A.; Patel, V.; Gavard, J.; Zhang, G.; Sousa, A. A.; Masedunskas, A.; Leapman, R. D.; Weigert, R.; Gutkind, J. S.; Rusling, J. F. *ACS nano* **2009**, *3*, 307.
(4) Thess, A.; Lee, R.; Nikolaev, P.; Dai, H.; Petit, P.; Robert, J.; Xu, C.; Lee, Y. H.; Kim, S. G.; Rinzler, A. G. *Science-AAAS-Weekly Paper Edition* **1996**, *273*, 483.
(5) Liu, Z.; Tabakman, S.; Welsher, K.; Dai, H. *Nano research* **2009**, *2*, 85.
(6) Kostarelos, K.; Bianco, A.; Prato, M. *Nature Nanotechnology* **2009**, *4*, 627.
(7) Gong, H.; Xu, G.; Liu, T.; Pang, J.; Dou, W.; Xin, X. *Colloid and Polymer Science* **2011**, *289*, 933.
(8) Blanch, A. J.; Lenehan, C. E.; Quinton, J. S. *The Journal of Physical Chemistry B* **2010**, *114*, 9805.
(9) Nagarajan, R.; Bradley, R. A.; Nair, B. R. *The Journal of chemical physics* **2009**, *131*, 104906.
(10) Nativ-Roth, E.; Shvartzman-Cohen, R.; Bounioux, C. l.; Florent, M.; Zhang, D.; Szleifer, I.; Yerushalmi-Rozen, R. *Macromolecules* **2007**, *40*, 3676.
(11) Granite, M.; Radulescu, A.; Pyckhout-Hintzen, W.; Cohen, Y. *Langmuir* **2011**, *27*, 751.
(12) Frise, A. E.; Pagès, G.; Shtein, M.; Pri Bar, I.; Regev, O.; Furó, I. n. *The Journal of Physical Chemistry B* **2012**, *116*, 2635.
(13) Yang, M.; Koutsos, V.; Zaiser, M. *The Journal of Physical Chemistry B* **2005**, *109*, 10009.
(14) Walther, J. H.; Jaffe, R.; Halicioglu, T.; Koumoutsakos, P. *The Journal of Physical Chemistry B* **2001**, *105*, 9980.
(15) Werder, T.; Walther, J. H.; Jaffe, R.; Halicioglu, T.; Koumoutsakos, P. *The Journal of Physical Chemistry B* **2003**, *107*, 1345.
(16) van der Spoel, D.; Lindahl, E.; Hess, B.; Kutzner, C.; van Buuren, A. R.; Apol, E.; Meulenhoff, P. J.; Tieleman, D. P.; Sijbers, A. L. T. M.; Feenstra, K. A.; van Drunen, R.; Berendsen, H. J. C. *Gromacs User Manual version 4.0*, **2005**.
(17) Hezaveh, S.; Samanta, S.; Milano, G.; Roccatano, D. *Journal of Chemical Physics* **2011**, *135*, 164501.
(18) Berendsen, H. J. C.; Grigera, J. R.; Straatsma, T. P. *Journal of Physical Chemistry* **1987**, *91*, 6269.
(19) Humphrey, W.; Dalke, A.; Schulten, K. *Journal of Molecular Graphics* **1996**, *14*, 33.
(20) Pang, J.; Xu, G.; Tan, Y.; He, F. *Colloid and Polymer Science* **2010**, *288*, 1665.
(21) Granite, M.; Radulescu, A.; Cohen, Y. *Langmuir* **2012**, *28*, 11025.
(22) Xin, X.; Xu, G.; Zhao, T.; Zhu, Y.; Shi, X.; Gong, H.; Zhang, Z. *The Journal of Physical Chemistry C* **2008**, *112*, 16377.

CHAPTER 4:

Coarse-Grained Simulation Studies of Adsorption Phenomena of F127 and F108 Triblock Copolymers to DWCNT Bundle

CHAPTER 4

COARSE-GRAINED SIMULATION STUDIES OF ADSORPTION PHENOMENA OF F127 AND F108 TRIBLOCK COPOLYMERS TO DWCNT BUNDLE

4.1 ABSTRACT

Amphiphilic block copolymers are found to be good dispersants for CNTs. In the current chapter a theoretical study of the adsorption phenomena of F127and F108 triblock copolymer chains on the surface of DWCNT bundles is described. Combined MD-SCF tool and CG models for pluronics and CNT have been used for the study. It has been observed an adsorption for both types of pluronics on the surface of the bundles. The tight interactions with CNTs have shown hydrophobic PPO blocks, while PEO blocks were interacting in weaker manner. The numbers of polymers aggregated on the surface of the bundles were found to be 21, 8/10 and 6 for the considered bundle lengths of 20, 10 and 4.7 nm, respectively.

CHAPTER 4

4.2 INTRODUCTION

Carbon nanotubes (CNTs) have attracted a great interest after being discovered in 1991 by Iijima[1] because of their outstanding properties and wide spectra of different applications.[2-5] The main obstacle of CNT utilization is associated with their poor solubility in water. Because of the strong van der Waals forces acting between the nanotubes, they usually do not exist as single tubes, but form aggregates – bundles.[6] Compared to covalent modification of CNTs, non-covalent approaches do not cause side defects for the CNTs and, thus save their unique properties, are able to disperse them in aqueous solutions. Several studies have been performed focused on non-covalent attachment of surfactants or polymers,[7-10] as well as macromolecules, [11-13] for CNT dispersion.

Triblock copolymers, known as pluronics, are good solubilizing agents for CNT.[14-16] They are composed of hydrophobic poly (propylene oxide) (PPO) in the middle and two hydrophilic poly (ethylene oxide) (PEO) at the ends. The solvation of the nanotube by pluronics occurs due to the attraction of hydrophobic blocks to the nanotube surface when hydrophilic blocks are extending into water phase, hence, creating a steric repulsion between the nanotubes.

Adsorption of block copolymers to single-walled carbon nanotubes (SWCNTs) and multi-walled nanotube has been studied by the group of Nativ-Roth.[16] The poly (styrene) - poly (metahcryl acid) diblock copolymer and poly (ethylene oxide-*b*- polydimethylsoloxane –*b* - ethylene oxide) triblock copolymer were considered for the experimental studies. Pluronic F88 $(PEO)_{100}(PPO)_{64}(PEO)_{100}$ and CNT (10, 10) of 21 nm in length were used to perform molecular dynamics simulation by the same group.[16] A non-wrapping mechanism, by which hydrophobic parts are non-specifically adsorbed on CNT and hydrophilic parts were extending into solutions, was suggested. Interaction of F127 $(PEO)_{106}(PPO)_{70}(PEO)_{106}$ and F108 $(PEO)_{132}(PPO)_{50}(PEO)_{132}$ triblock copolymers with SWCNTs in aqueous solutions has been investigated by Granite using small-angle neutron scattering method.[14] As mentioned in the previous chapter, two models by which polymers adsorb onto CNT surface were introduced. The first is core – chain model, where the core represents a CNT bundle and chains are the adsorbed polymers, without any differentiation between the PEO and PPO units. The second one is core –

shell – chains model. In this model the shell is represented by hydrophobic PPO units, while the chains are PEO parts, emanating into aqueous solutions, core consists of the CNT bundle. Number of aggregated polymer chains is indicated to be ~ 9 per nanotube length of 100 A.[14]

In this chapter the study of adsorption of F127 and F108 triblock copolymers onto double-walled (DWCNT) bundle surface of different length is introduced. Since, the system presented here is larger compared to the one described in the previous chapter, more powerful technique to perform simulations is required. The coarse-grained (CG) approach, based on MD-SCF combination[17] has been applied for the study. The purpose of the work represents the understanding of the mechanism of adsorption at CG level of longer polymer chains, rather than the one presented in the previous chapter.

4.3 COMPUTATIONAL METHOD

4.3.1 Models and Parameters

The CG models for F127 and F108 has been constructed in the same manner like the one proposed by Hezaveh et al.[18-19] In particular, each bead of CG model includes three (C-O-C) and four ($C(CH_3)$-O-C) heavy atoms for PEO and PPO, respectively.[19]

CG model for CNT was constructed according to the method suggested by Lopez.[20] DWCNT model was used to perform simulations. The reason of DWCNT choice is driven due to the incompressibility condition (see second addend of eq. 2.2.4, Chapter 2) which tries to keep the density in the system homogeneous. In the case of simulation with single-walled nanotubes, interpenetration of CNT layers occurred due to the hallow cores present in the structure of the last ones. To avoid interpenetration of the CNT walls, DWCNTs has been chosen to perform simulations. In Figure 4.1 is shown the comparison between the atomistic and CG models of DWCNT. The outer wall, depending on length of the nanotube, consists of different numbers of octagonal rings, which means eight coarse-grained carbon atoms are represented in each ring. The inner wall consists of triangular layers that correspond to three coarse-grained carbon atoms in each triangular layer. 6.6 to 1 mapping was performed in order to obtain the CG CNT model. This means that each CG bead of carbon consists of 6.6 real carbon atoms. The CG model of

DWCNT corresponds to the zig-zag atomistic nanotube with chiral indices m=16, n=0 for the outer wall and m=6, n=0 for the inner wall. As for the model of water, Marrink [21] CG approach was implemented, where four to one mapping is performed to describe the model. Mass of each united atom is 72 a.m.u.

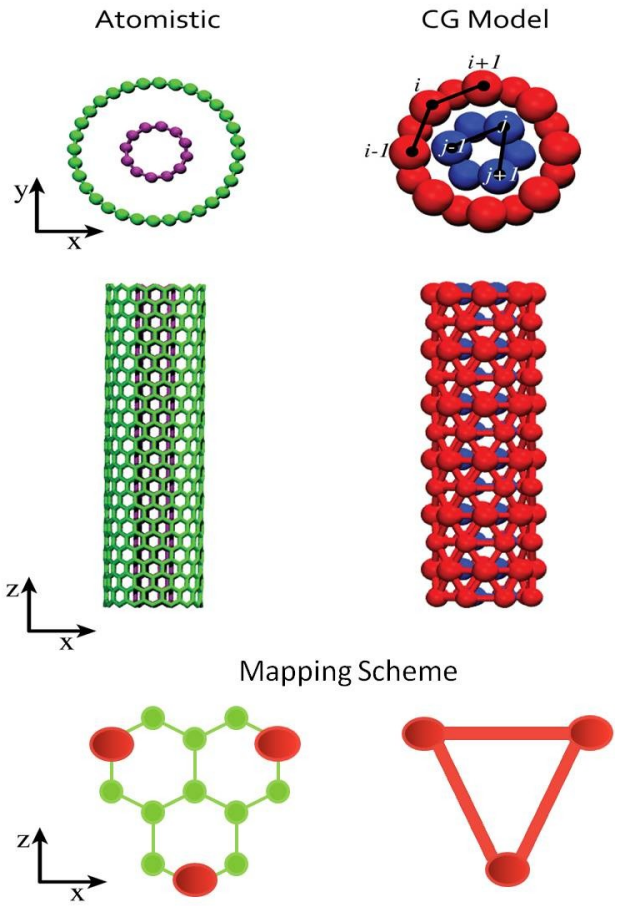

Figure 4.1: Comparison between atomistic (left side) and coarse-grained (right side) models of DWCNT. Outer wall consists of CNTs with chiral indices m = 16, n = 0, inner wall with indices m=6, n=0. In the bottom of the figure the correspondence between atoms and effective beads is schematized.

Table 4.1 contains the labels used in the simulations for real molecule types. Detailed information related to bond lengths, angles and corresponding force constants are reported in Tables 4.2 and 4.3.

Table 4.1: *Labels of the particles used in simulations and corresponding molecule types.*

Labels for particles used in simulations	Real molecule types
O	PEO
J	PPO
S	C - carbon atoms for the outer wall of DWCNT
K	C - carbon atoms for the inner wall of DWCNT
W	Water

Table 4.2: *Parameters for bonds' energetic terms.*

Bond Type	b_o (nm)	K_b (kJ mol^{-1} nm^{-2})
O-O	0.28	8000
O-J	0.28	6500
J-J	0.28	5000
S-S	0.47	1250
S-K	0.45	2500
K-K	0.47	1250

Table 4.3: *Parameters for angles' energetic terms*

Angle Type	θ_o (deg)	K_θ (kJ mol^{-1})
O-O-O	155	40
O-J-J	140	30
J-O-O	140	30
J-J-J	140	40
S-S-S	135	2500
K-K-K	60	2500

4.3.2 System Setup

DWCNT bundles consisting of three nanotubes were centered in cubic boxes. Chains of Pluronics F108 and F127 were added in order to keep the same concentration as in experimental work performed by Granite.[14] In particular, 0.5% DWCNT + 5 % F108 and 0.5% DWCNT + 4 % F127 are the concentrations considered in the simulations. The box was filled with water to keep the concentration of 1g/cm^3. The superimposed water molecules were removed from the system. In Table 4.4 is described the size and composition of the simulated systems.

Table 4.4: *Details about simulated system*

System	**Box Size** (nm)	**Composition**					
	x=y=z	**No. of Particles**	**No. of F127 chains**	**No. of F108 chains**	**No. of Water**	**Length of CNT bundle, nm**	**Simulation length, μs**
1	33.0163	319188	72		297300	20	2.22
2	33.0316	322146		84	294186	20	2.30
3	26.2123	1597230	36		148779	10	3
4	26.2243	161199		42	147219	10	3
5	22.8187	104830	18		99358	4.7	2.5

4.3.3 Simulation Details

The parallel molecular dynamics program OCCAM[22] was used to execute combined MD-SCF simulations. MD-SCF simulations have been performed using a time step of 0.03 ps with the *NVT* ensemble by keeping the temperature constant using Andersen's thermostat[23] with a collision frequency of 5 ps^{-1}. The grid size considered in the simulations is 0.705 nm. In Table 4.5 are reported particle-field interaction parameters $\chi_{KK'}$ needed to calculate the interactions between a particle of type *K* and the density fields due to particles of type *K*'.

Table 4.5: *Particle-Field Interaction parameters $\chi_{KK'} \times RT$ (kJ/mol).*

	O	J	S	K	W
O	0.00	16.00	7.80	7.80	1.50
J	16.00	0.00	-1.60	-1.60	4.60
S	7.80	-1.60	0.00	0.00	27.9
K	7.80	-1.60	0.00	0.00	27.9
W	1.50	4.60	27.9	27.9	0.00

4.3.4 Calculation of Aggregation Number N_{agg}

Number of aggregated chains (N_{agg}) of pluronics on the surface of the bundle has been calculated. The chain is considered to be adsorbed on the surface of the bundle, first, if the distance D between the nanotube and the chain of pluronic is less than assigned in advance the value of the radius *r*. Second, if N_{agg} is constant during the time.

$$D = \sqrt{(x - x_1)^2 + (y - y_1)^2 + (z - z_1)^2} \qquad (4.1).$$

Where D is the distance between the nanotube and the chain of pluronic; (*x, y* and *z*) and (x_1, y_1 and z_1) are the cartesian coordinates for the nanotube and for the chain of pluronic, respectively.

If D < r, then chain is considered adsorbed on the surface of the bundle. Here *r* is in advance assigned radius. N_{agg} represents the sum for all the chains that satisfy this condition.

4.4 RESULTS AND DISCUSSION

In Figure 4.2 are shown snapshots of simulations, where chains of F127 and F108 pluronics are adsorbed on the surface of the DWCNT bundle of different lengths. Similarly, as described in experiment[14], due to hydrophobic interactions the chains of triblock copolymers are in contact with the bundles by their hydrophobic PPO part, while more hydrophilic PEO blocks are extending into water. For clarity in Figure 4.2 water molecules are omitted. The mechanism of wrapping of DWCNT bundles by the chains of the polymers is in accordance with the so called core-shell-chain model proposed by Granite et al.[14] As an example, in Figure 4.3 is presented a bundle of DWCNT of 20 nm coated by pluronic F108. It is shown that the shell is formed by PPO parts (labeled in green), PEO chains are protruding in water phase (shown in red) and the core is presenting the bundle (marked in yellow and orange).

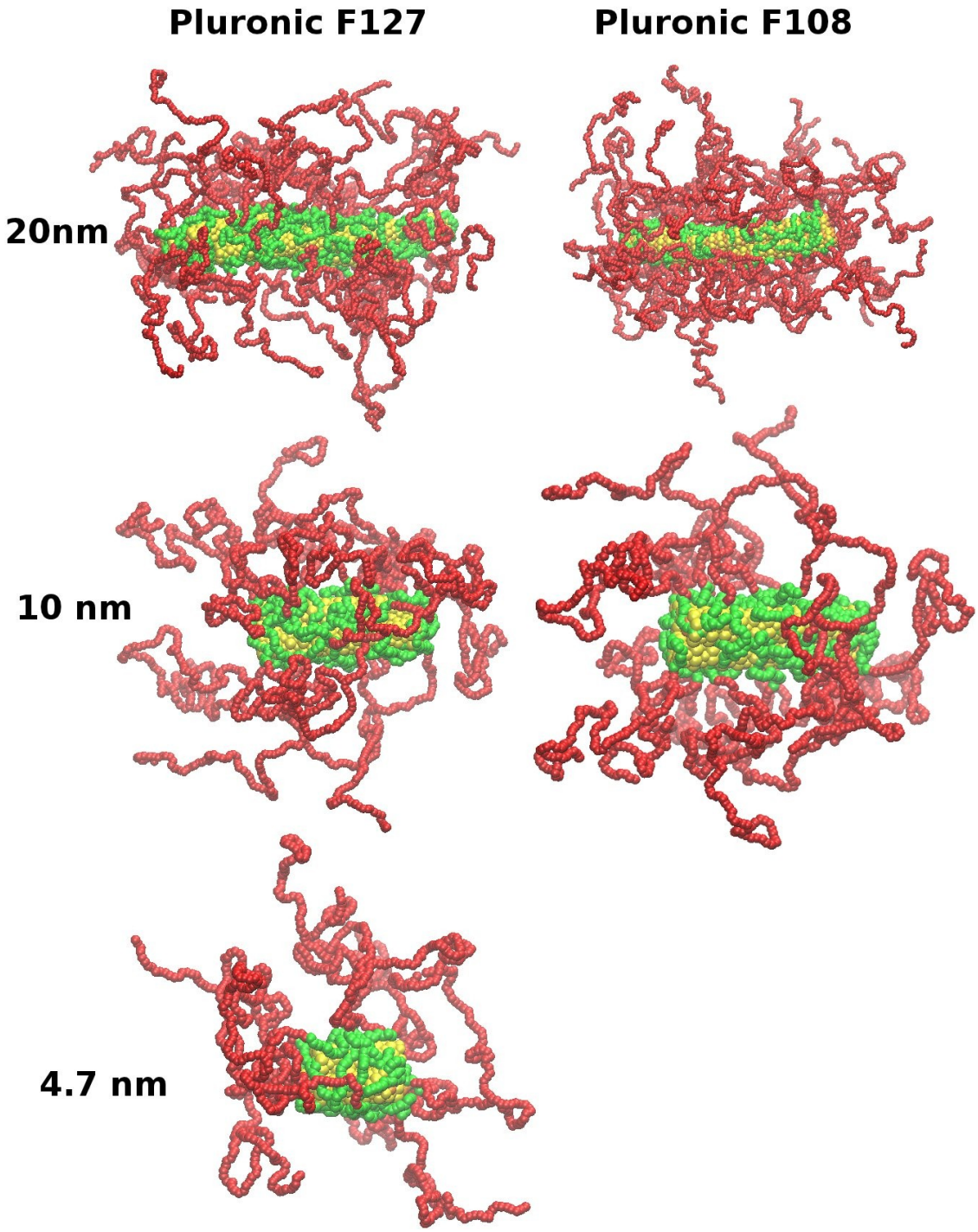

Figure 4.2: Adsorption of F127 and F108 onto the surface of DWCNT bundle with the length of 20 nm, 10 nm and 4.7 nm. PEO part is shown in red, PPO in green and DWCNT in yellow (outer layer) and orange (inner layer).

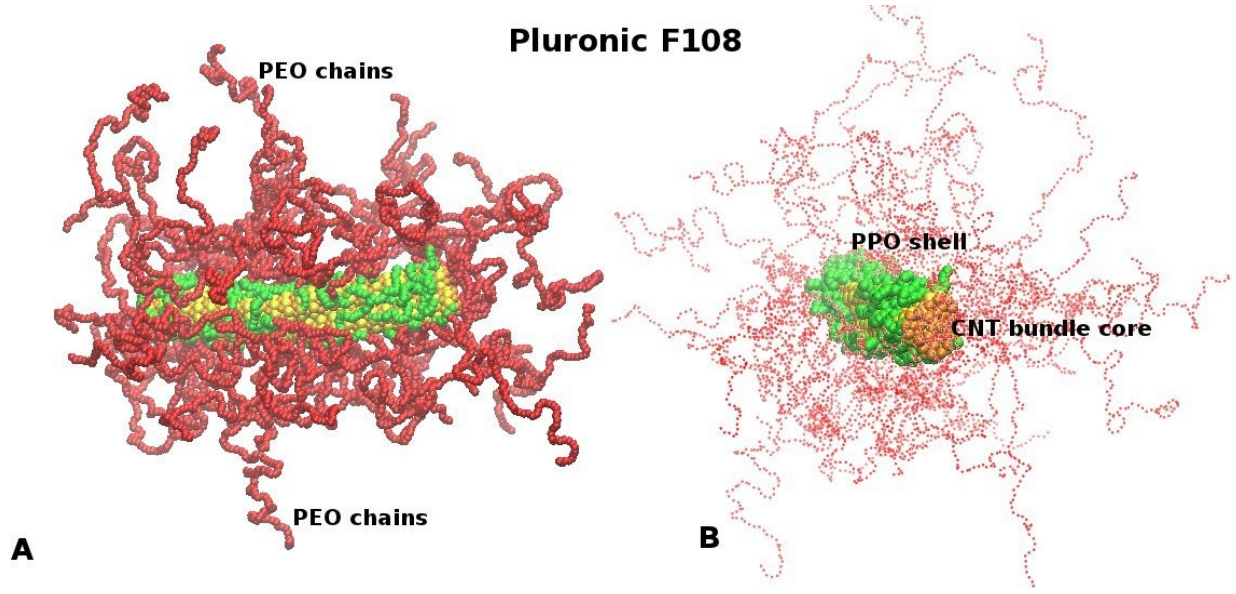

Figure 4.3: Adsorption of pluronic onto the bundle is in accordance with core-shell-chains model, where core represents the bundle (marked in yellow for the outer layer and in orange – for inner) (**B**), shell – PPO part (shown in green) (**B**) and chains are presented by PEO (red) (**A**).

Number of chains aggregated to the bundle has been estimated. It was found that number of aggregated chains N_{agg} of F108 and F127 consists of 21 chains for the bundle of 20 nm in length. These numbers are equal to 8 for F108 and 10 for F127 in the case of adsorption on the surface of 10 nm length bundle. For the shortest length bundle, namely for 4.7 nm, N_{agg} is equal to 6 chains. These results are fitting with experimental data well,[14] where 9 chains of polymers per length of 10 nm of the bundle were observed. Table 4.6 contains the data related to N_{agg} for each pluronic and the bundles of DWCNT of different length.

Table 4.6: N_{agg} for *pluronic F108 and F127 onto the surface of the bundle of 20, 10 and 4.7 nm in length.*

N_{agg}	Length of the bundle, nm		
	20	**10**	**4.7**
F108	21	8	
F127	21	10	6

CHAPTER 4

4.5 CONCLUSIONS

CG simulations have been performed based on hybrid MD-SCF method. Results obtained out of the simulations are in a good accordance with experimental data. In particular, it was found that the manner of adsorption of pluronics is based on attachment of pluronic chains by hydrophobic PPO part to hydrophobic surface of the bundle and extension of hydrophilic PEO part into water phase. N_{agg} per 20 nm length bundles are 21 for both, F127 and F108; N_{agg} per 10 nm length bundles is 8 for F108 and 10 for F127 which fits very well the value of 9, obtained out of the experimental data. And, finally, N_{agg} for the shortest CNT bundle of 4.7 nm length is found to be 6. These are preliminary results describing that MD-SCF method can reproduce the data compatible with experimental results. Further studies could be interesting to be applied to investigate an interaction of the pluronics+bundle complex with the lipid bilayer, as a model of cellular membrane.

4.6 REFERENCES

(1) Iijima, S. *Nature* **1991**, *354*, 56.

(2) Yang, W.; Thordarson, P.; Gooding, J. J.; Ringer, S. P.; Braet, F. *Nanotechnology* **2007**, *18*, 412001.

(3) Sinha, N.; Yeow, J.-W. *NanoBioscience, IEEE Transactions on* **2005**, *4*, 180.

(4) Zhang, Y.; Bai, Y.; Yan, B. *Drug discovery today* **2010**, *15*, 428.

(5) Lacerda, L.; Bianco, A.; Prato, M.; Kostarelos, K. *Advanced drug delivery reviews* **2006**, *58*, 1460.

(6) Thess, A.; Lee, R.; Nikolaev, P.; Dai, H.; Petit, P.; Robert, J.; Xu, C.; Lee, Y. H.; Kim, S. G.; Rinzler, A. G. *Science-AAAS-Weekly Paper Edition* **1996**, *273*, 483.

(7) Blanch, A. J.; Lenehan, C. E.; Quinton, J. S. *The Journal of Physical Chemistry B* **2010**, *114*, 9805.

(8) Frise, A. E.; Pagès, G.; Shtein, M.; Pri Bar, I.; Regev, O.; Furó, I. n. *The Journal of Physical Chemistry B* **2012**, *116*, 2635.

(9) Pang, J.; Xu, G.; Tan, Y.; He, F. *Colloid and Polymer Science* **2010**, *288*, 1665.

(10) Xin, X.; Xu, G.; Zhao, T.; Zhu, Y.; Shi, X.; Gong, H.; Zhang, Z. *The Journal of Physical Chemistry C* **2008**, *112*, 16377.

(11) Zheng, M.; Jagota, A.; Semke, E. D.; Diner, B. A.; McLean, R. S.; Lustig, S. R.; Richardson, R. E.; Tassi, N. G. *Nature materials* **2003**, *2*, 338.

(12) Star, A.; Steuerman, D. W.; Heath, J. R.; Stoddart, J. F. *Angewandte Chemie International Edition* **2002**, *41*, 2508.

(13) Bandyopadhyaya, R.; Nativ-Roth, E.; Regev, O.; Yerushalmi-Rozen, R. *Nano letters* **2002**, *2*, 25.

(14) Granite, M.; Radulescu, A.; Pyckhout-Hintzen, W.; Cohen, Y. *Langmuir* **2011**, *27*, 751.

(15) Granite, M.; Radulescu, A.; Cohen, Y. *Langmuir* **2012**, *28*, 11025.

(16) Nativ-Roth, E.; Shvartzman-Cohen, R.; Bounioux, C. l.; Florent, M.; Zhang, D.; Szleifer, I.; Yerushalmi-Rozen, R. *Macromolecules* **2007**, *40*, 3676.

(17) Milano, G.; Kawakatsu, T. *The Journal of chemical physics* **2009**, *130*, 214106.

(18) Hezaveh, S., Jacobs University Bremen, 2012.

(19) Hezaveh, S.; Samanta, S.; De Nicola, A.; Milano, G.; Roccatano, D. *Journal of Physical Chemistry B* **2012**, *116*, 14333.

(20) Lopez, C. F.; Nielsen, S. O.; Ensing, B.; Moore, P. B.; Klein, M. L. *Biophysical journal* **2005**, *88*, 3083.

(21) Marrink, S. J.; Risselada, H. J.; Yefimov, S.; Tieleman, D. P.; de Vries, A. H. *Journal of Physical Chemistry B* **2007**, *111*, 7812.

(22) Zhao, Y.; De Nicola, A.; Kawakatsu, T.; Milano, G. *Journal of Computational Chemistry* **2012**, *33*, 868.

(23) Frenkel, D.; Smit, B. *Understanding molecular simulation: from algorithms to applications*; Access Online via Elsevier, 2001.

CHAPTER 5:

Spontaneous Insertion of Carbon Nanotube Bundles inside Biomembranes: a Hybrid Particle-Field Coarse-Grained Molecular Dynamics Study

CHAPTER 5

SPONTANEOUS INSERTION OF CARBON NANOTUBE BUNDLES INSIDE BIOMEMBRANES: A HYBRID PARTICLE-FIELD COARSE-GRAINED MOLECULAR DYNAMICS STUDY

5.1 ABSTRACT

Due to the ability to cross cellular membranes, CNTs have been proposed to be exploited as nano-transporters for drugs or other biologically active molecules inside the cell. Understanding of the mechanism of CNT interactions with cellular membrane will simplify their applications for targeted drug delivery. In order to understand these principles, first it would be efficient to clarify how CNTs interact with pure lipid bilayer. This chapter is dedicated to the study of spontaneous insertion of CNTs bundles inside DPPC lipid membranes. A hybrid particle-field CG MD approach is used to describe the interactions. In particular, influence of the orientation and the aspect ratio of CNT bundles on the membrane perturbation are taken into consideration. The results are indicating on the perturbation of the lipid bilayer for all the studied systems. However, the distortions are more obvious for the case of perpendicularly oriented bundles. The poration of the membrane has been observed during the internalization of the bundle of 20 nm.

CHAPTER 5

5.2 INTRODUCTION

After being discovered, CNTs have attracted scientific attention due to their outstanding properties and characteristics.[1] Indeed, their ability to cross cell membranes[2] opens innumerable possibilities for biomedical applications.[3-4] Their large surface area allows attachment of biological molecules.[5-7] The empty core of the CNTs provides an opportunity to exploit them as nano-containers for drug[8-9] or any desired biologically active molecule encapsulation.[10-11]

The main difficulty of direct use of CNT is associated with their hydrophobicity and tendency to aggregate into bundles. Such kind of aggregates may evoke cytotoxic effect and even cause cell death in dose dependent manner. For this reason the interaction of CNTs with cellular membranes is an extremely demanding task for investigation. Understanding of these principles will determine any further applications of CNTs. Several studies have been performed in order to understand the pathways of internalization.[12-19]

The research group of Al-Jamal[12] has studied the cellular mechanism of functionalized MWCNTs by 3D electron tomography imaging. Two types of cells – epithelial lung carcinoma cells (A549) and human monocyte-derived macrophages (HMMs) have been considered for the interactions with functionalized MWCNTs NH_3^+. The results of the study suggest that the internalizations can occur either by direct piercing of the membrane of single nanotubes or by the wrapping of the nanotube by lipids of the cell membrane.[12] Such kind of translocations for single nanotubes was found to be energy independent, however, for the bundles or clusters of the nanotubes this process occurred via endocytosis and required energy.[12] The study of the mechanism of uptake of SWCNTs by HMMs has been performed by Porter et al.[13] Confocal microscopy and transmission electron microscopy (TME) techniques were used for observations. Energy dependent phagocytosis or endocytosis and passive diffusion were the pathways observed by Porter et al.[13] However, Yaron[17] and coworkers suggest that the only path, by which internalization of SWCNT occurs, is the endocytosis and not membrane penetration. The confocal Raman spectroscopy and fluorescence lifetime imaging (FLIM) has been applied in order to observe the path of SWCNT internalization into the cell membrane. SWCNTs were non-

covalently functionalized by pluronic F127 (PF-127). It was found that PF-127-SWCNT were localized in endosomes while interacting with HeLa cells.[17]

Theoretical study based on non-equillibrium all-atom steered molecular dynamics (SMD) simulations has been performed by Gangupomu and Capaldi[18] in order calculate the forces and the free energies required for the CNT to traverse the lipid bilayer. CNT of 2 nm in length and with the diameter of 1 nm was used in the study. The Palmitoyl, 2-Oleyoyl, Phosphatidylcholine (POPC) with and without the presence of cholesterol has been considered. The results, obtained by the authors, indicated on the dependence of the force, required to rupture the membrane, on the pulling velocity of CNT insertion. In particular, the rupture force was decreasing by decreasing the velocity of CNT. The presence of cholesterol did not affect the forces and free energies required to puncture the membrane, however, it favored the pore formation inside the lipid membrane.[18] Parthasarathi[20] has demonstrated the all-atom MD simulation for investigation of dioleoylphosphatidylcholine (DOPC) perturbation by the single CNT and the bundle, composed of seven CNTs (5, 5) of 6 nm in length. The orientations inside the membrane for the single nanotube were parallel and perpendicular, while for the bundle only perpendicular orientation respect to the bilayer surface has been considered. In all cases the perturbation of the lipids and swelling of the membrane had place. However, the perturbation of the lipids was found to be more in the case of the bundles and for the nanotube, placed in a perpendicular orientation.[20]

In the present chapter is demonstrated the study of interaction of DWCNT bundles with DPPC lipid bilayer. DPPC represents one of the major components of cell membranes. The structural properties of this phospholipid have already been tested by our research group[21] at the University of Salerno. The focus of the current work is based on the understanding of CNT bundles' interaction with DPPC lipid bilayer as a model of cell membrane. The study is carried out on the basis of MD-SCF CG approach. Investigation of larger scale system (~ 32 nm) for a longer simulation time (~3 μs) is provided. Influence of the orientation and the aspect ratio on the perturbation of DPPC lipid bilayer has been studied in the present chapter.

CHAPTER 5

5.3 MODELS AND METHODS

5.3.1 Simulation Methodology

The models considered here have been developed in a hybrid particle-field scheme combining Molecular Dynamics (MD) and Self Consistent Field (SCF). The theoretical scheme of MD-SCF technique is described in the second chapter related to Computational Methods.

5.3.2 Simulation Details

Simulations reported here have been performed using the parallelized version of the OCCAM code.[22-23] All simulations have been performed with velocity Verlet algorithm using a time steep of 0.03 ps in the *NVT* ensemble by keeping the temperature constant at 325 K - temperature that is above the transition phase at 315 K[24] and at which the area per lipid is close the one found out of experimental results.[21] Andersen's thermostat[25] with a collision frequency of 7 ps^{-1} was used to maintain the temperature of the system constant. The density field calculations have been performed using grid resolution of 0.705 nm and an update frequency of 300 steps. In Table 5.1 the simulated systems and their compositions are reported. Information related to bond length, bond angle for DPPC lipid molecule and the particle-filed interaction parameters $\chi_{KK'}$ are reported in Tables 5.2, 5.3 and 5.4, respectively. The corresponding parameters for the DWCNT are reported in Computational Method section of **Chapter 4**.

Table 5.1: *Composition of the simulated system.*

System	Box length [x=y=z] (nm)	DWCNT Length (nm)	No. of DPPC	No. of Water Beads	No. of DWCNT	Total No. of Particles
I	16.3521	4.6	832	27829	6	38605
II	32.7042	10.0	3319	267088	6	308500
III	32.7042	20.0	3319	265541	6	308537

Table 5.2: *DPPC bond parameters.*

Bond Type	b_o (nm)	K_b (KJ mol^{-1} nm^2)
N-P	0.470	1250
P-G	0.470	1250
G-G	0.370	1250
G-C	0.470	1250
C-C	0.470	1250

Table 5.3: *DPPC angle parameters.*

Angle Type	θ_o (deg)	K_θ (kJ mol^{-1})
P-G-G	120	25.0
P-G-C	180	25.0
G-C-C	180	25.0
C-C-C	180	25.0

Table 5.4: *Particle-Field interaction parameters $\chi_{KK'} \times RT$ (kJ/mol).*

χ_{ij}	**N**	**P**	**G**	**C**	**W**	**S**
N	0.00	-1.50	6.30	9.00	-8.13	5.10
P	-1.50	0.00	4.50	13.50	-3.60	9.30
G	6.30	4.50	0.00	6.30	4.50	3.90
C	9.00	13.50	6.30	0.00	40.50	2.40
W	-8.13	-3.60	4.50	40.50	0.00	27.90
S	5.10	9.30	3.90	2.40	27.90	0.00

5.3.3 Coarse-Grained Models for Carbon Nanotube, DPPC Lipid and the Molecule of Water

The CG particle-field model of DWCNT corresponds to the one described in the **Chapter 4**. As for the DPPC lipid and water molecules, particle-field model has been developed considering the CG model proposed by Marrink.[26] The MARTINI[26] force field has been considered as a reference model and the parameters needed for the particle field models (such as χ parameters, see Computational Methods in **Chapter 2**) have been optimized in order to reproduce some features of the reference model.

From the point of view of reduction of the degrees of freedom of biomolecular system, in a model of Marrink[26] a four to one mapping is used to represent the molecules; it means that four atoms are represented by a single interaction center. In Figure 5.1 is shown a mapping between a real structure and the CG representation of Marrink model of DPPC and the molecule of water.

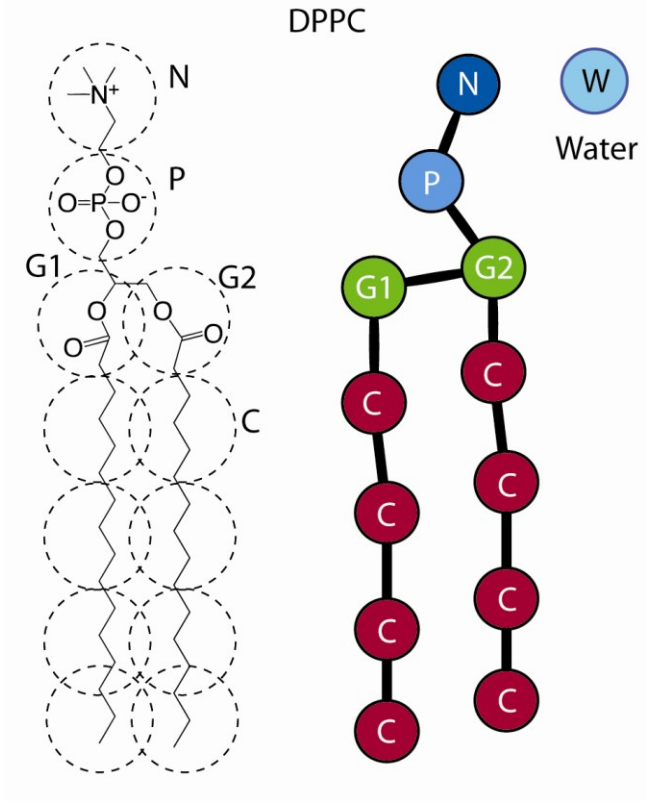

Figure 5.1: Atomistic (left) and CG model (right) of DPPC lipid molecule, derived from atomistic by four to one mapping.

CHAPTER 5

5.4 RESULTS AND DISCUSSIONS

5.4.1 Bundle Formation

A system of six nanotubes of length 4.7 nm in water has been simulated (system I in Table 5.1). In the initial configuration nanotubes were placed randomly in the simulation box avoiding superposition between them. In Figure 5.2, together with the behavior of the particle-field potential (the first addend of eq. 2.2.4 in Computational Methods part of **Chapter 2**) several snapshots are shown. A first sudden aggregation, corresponding to a drop in the particle-field potential, between closest CNTs is obtained. The first snapshot of Figure 5.2 shows some disordered aggregations between pairs or trimers of CNT. In particular, weak (small contact surface) and strong (large contact surface) pairs between CNTs can be identified. During the simulation it is possible to observe weak pairs dissociating or evolving through strong pairs. Strong pairs when formed they are stable and promote the stable aggregation of new CNTs until an ordered bundle is formed. It is interesting to see that when the stable contacts are formed and dissociations do not occur this corresponds to fast drops in the particle-field potential (for instance from the second to the third configuration of Figure 5.2) and in almost 250 ns the formation of an ordered bundle can be observed.

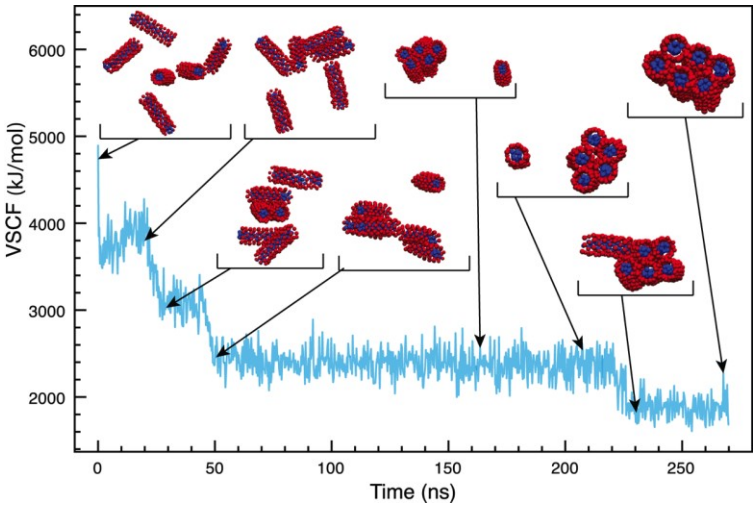

Figure 5.2: Time evolution of particle-field potential (first addend of eq. 2.2.4 in Computational Methods part) together with some snapshots.

Larger bundle or bundles having longer CNTs show similar behaviors, for the systems having CNT bundles interacting with lipid bilayers and reported in the next subsection, ordered bundles have been constructed from the beginning of the simulation and equilibrated in water. The configurations obtained in this way are stable and have been used for simulations described in the following section.

5.4.2 Bundles Insertion into Lipid Bilayers

In Figure 5.5 the time behavior of the center of mass position and orientation of a bundle of six CNTs 4.6 nm long are reported. In particular, for the system in Figure 5.5 and for all the other reported in the present chapter, the position of the center of mass of the bundle is reported taking as zero the average *z* coordinate of phospholipids in the first layer.

The orientation of the CNT bundle, as schematized in Figure 5.3, is calculated considering the angle of the bundle axis with respect to the *z* direction perpendicular to the bilayer plane. In particular, the order parameter P_2(t) has been reported calculating the second order Legendre polynomial $P_2(t) = \frac{3}{2}\cos^2(\theta(t)) - \frac{1}{2}$. Values of P_2 close to one indicate a parallel or antiparallel orientations, values close to -0.5 indicate a perpendicular orientation.

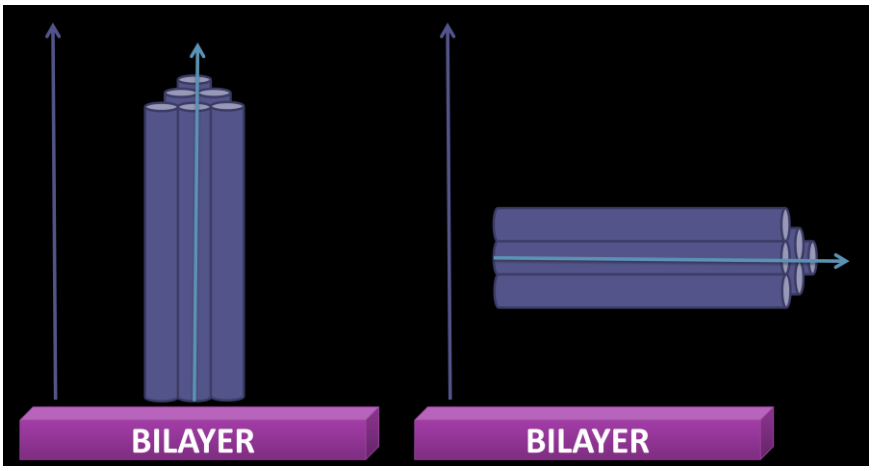

Figure 5.3: Definition of the CNT bundle orientation with respect to the lipid bilayer plane.

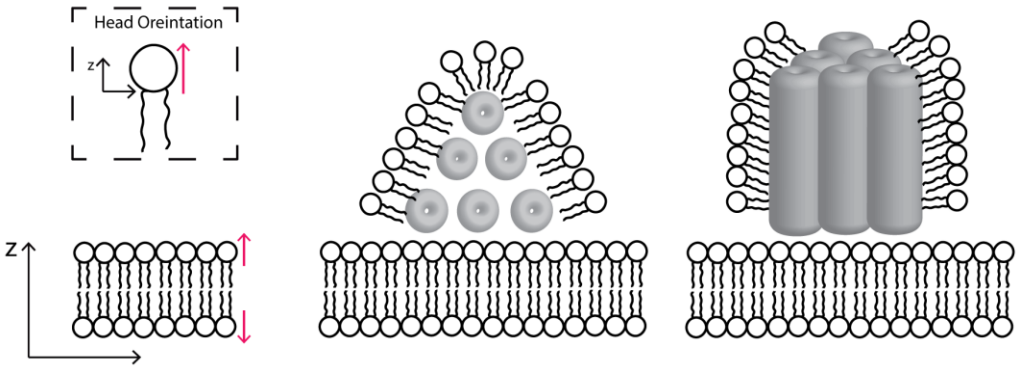

Figure 5.4: Definition of the DPPC orientation with respect to the *z* axis perpendicular to the lipid bilayer plane. In the figure the typical orientations in the equilibrium configuration of a lipid bilayer in the upper and lower layer (on the left) and when the bilayer structure is perturbed by a CNT bundle in parallel (center) and perpendicular orientation (right) are depicted. A vector joining beads of type G and N (depicted in red) is used to define the lipids orientation along the z axis.

As shown in Figure 5.5 A, from the beginning of the MD simulation there is a decrease of the CNT height toward the hydrophobic region of the lipid bilayer. In particular, after about 120 ns the insertion of the CNT bundle inside the hydrophobic region is completed. As shown in Figure 5.5 C, there is no strong correlation between CNT height with respect to the lipid bilayer and its orientation. Due to the low aspect ratio of the CNTs (their length is 4.6 nm) the orientation of the CNT bundle is very variable. (see also Figure 3.5 A). During the simulation the intermolecular potential reported in Figure 5.5 B (eq. 2.2.4 in the particle-field approximation, see Computational Methods part in **Chapter 2**) shows a fast and monotonic decrease up to 150 ns.

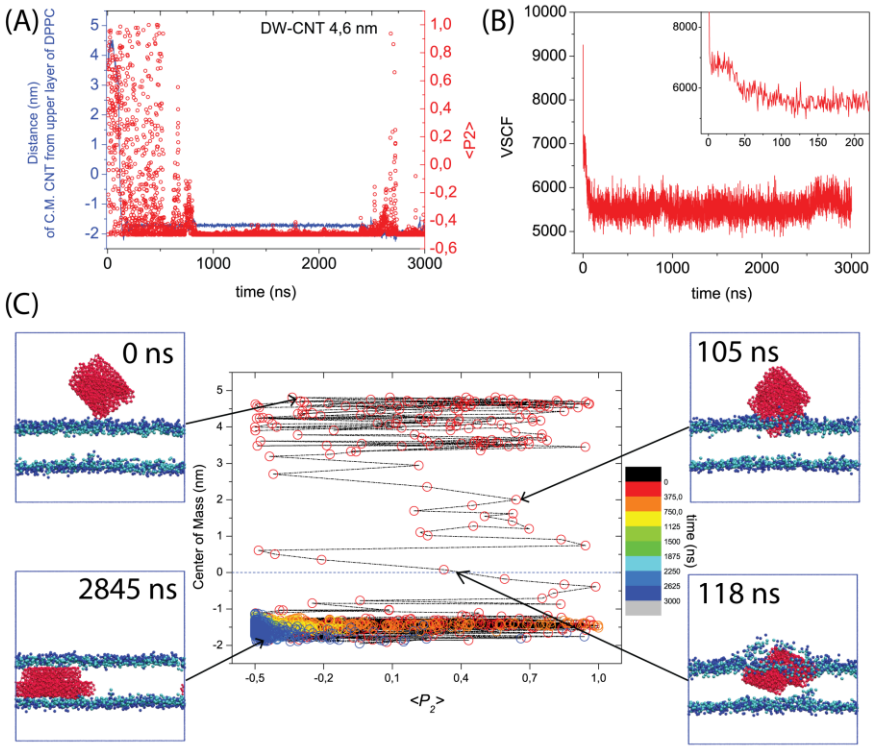

Figure 5.5: System I. Time behavior of **A**) CNT bundle center of mass height (blue curve) and orientation (P_2, red curve); **B**) Particle field potential (second addend of eq. 2.2.4 in Computational Methods part) **C**) correlation between center of mass height and bundle orientation together with some snapshots.

In order to analyze the distortions of the lipid bilayer during the insertion process two geometrical quantities have been considered. In particular, the deviation from the equilibrium lipid height (Δz) and the value of the cosine of the angle θ between the lipid and the z axis as defined in Figure 5.4. Both Δz and $\cos\theta$ have been averaged on a lattice made of 8x8 cells. In every cell, on average, there are 6.5 lipid/layer. For the larger systems (II and III), considered later, a grid of 16x16 with the same cell size (about 2 nm) and the same average number of lipid/layer has been used for the analysis.

In Figures 5.6 the deviation from the equilibrium height for upper (top of Figure 5.6 A) and lower layers of lipids (bottom of Figure 5.6 A) and the orientation of DPPC molecules with respect to the z axis in the upper (top of Figure 5.6 B) and lower layers (bottom of Figure 5.6 B),

as defined in Figure 5.4, are reported for different configurations. In the center the corresponding configurations of CNT bundle are depicted in both Figures 5.6 A and 5.6 B. As shown in the plots of Figure 5.6 A, the larger perturbation on the lipids height on both upper and lower layer is obtained between 105 and 118 ns, during the insertion process of the CNT bundle with a deviation in the lipids height between 1 and 1.5 nm. This behavior is clearer comparing the plots of Figure 5.6 A and the simulation snapshots reported in Figure 5.5 C. A similar behavior is obtained for the lipids orientation, in particular, as shown in Figures 5.6 B in the upper layer in a region localized close to the CNT bundle, for configurations between 118 and 150 ns the lipid orientation is about 90° with respect to the *z* axis. When the CNT bundle approaches the lipid bilayer large distortion of the lipids heights and orientation occur. The lipids closer to the CNTs of the bundles tend to be adsorbed on the CNT surface and to orient pointing the hydrophobic carbon tails towards and to expose the polar heads to the water phase. As shown in the following this is a common process in all the considered systems. A schematization of this behavior is depicted in Figure 5.4.

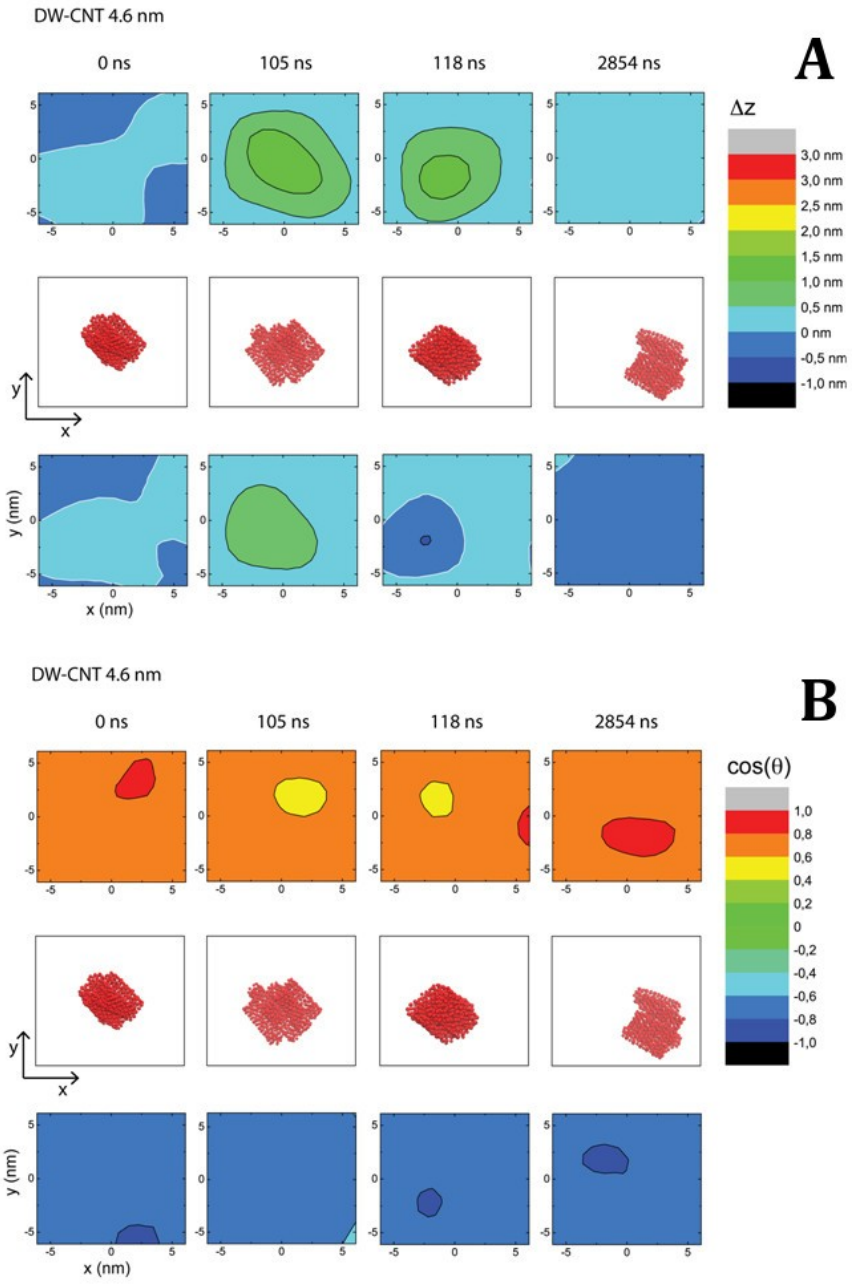

Figure 5.6: System I. **A**) Deviation (Δz) from the equilibrium height for upper (top of figure) and lower lipid layers (bottom of figure) for different configurations. **B**) Lipid orientation cos θ. In the center of both figures **A** and **B** the corresponding configurations of CNT bundle are depicted.

CHAPTER 5

In the following simulation results involving four systems having CNT bundles of larger aspect ratios will be reported. In particular, the insertions of bundles made of CNT of length 10 and 20 nm starting from parallel and perpendicular orientation of the bundle axis with respect to the bilayer plane have been simulated.

In Figure 5.7 main results of the insertion of the bundle made of CNTs of 10 nm length are summarized (system II). Similarly to the system with shorter CNTs, from the beginning of the MD simulation there is a decrease of the CNT height toward the hydrophobic region of the lipid bilayer. Differently from the system with shorter CNTs, where basically no correlation between bundle height and its orientation is found, here a parallel orientation with some small deviation during the insertion process (see Figure 5.7 B) is found. Also in this case, during the simulation the intermolecular potential (eq. 2.2.4 in the particle-field approximation, see Computational Methods part, **Chapter 2**) shows a fast and monotonic decrease up to 150 ns.

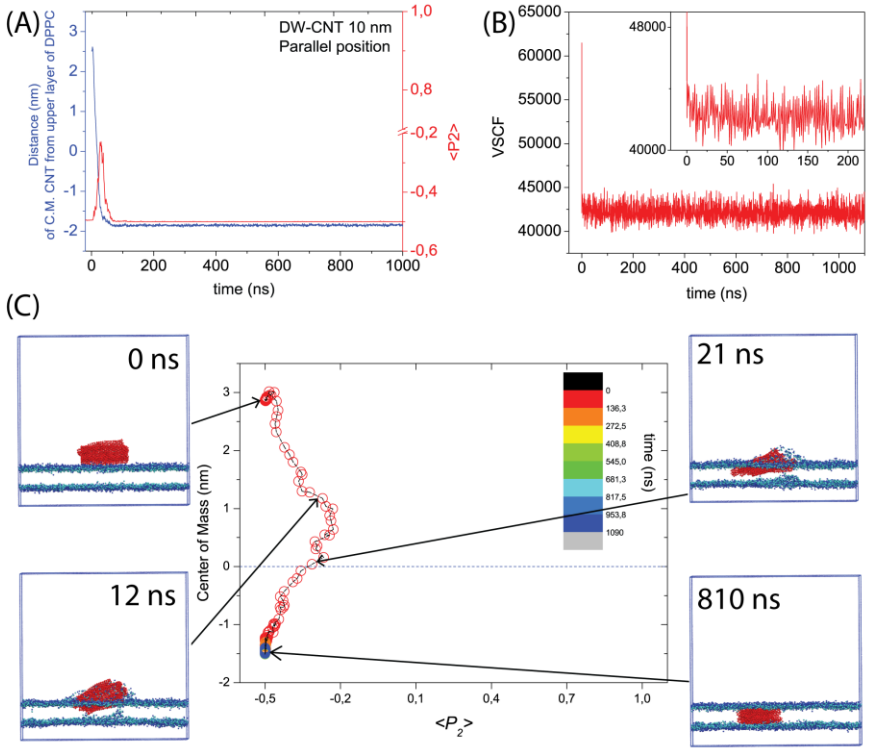

Figure 5.7: System II (bundle in parallel orientation). Time behavior of **A**) CNT bundle center of mass height (blue curve) and orientation (P_2, red curve); **B**) Particle field potential (second added of eq. 2.2.4) **C**) Correlation between the center of mass height and the bundle orientation together with some snapshots.

The distortion of equilibrium height of lipids is larger. In particular, a region with a displacement close to 2 nm (see Figure 5.8 A) has place in this case. The lipid orientation is more perturbed, as well, with respect to the system with shorter CNTs. Namely, the region where the orientation is almost perpendicular is larger with a central part where the average value of the cosθ is zero (see Figure 5.8 B).

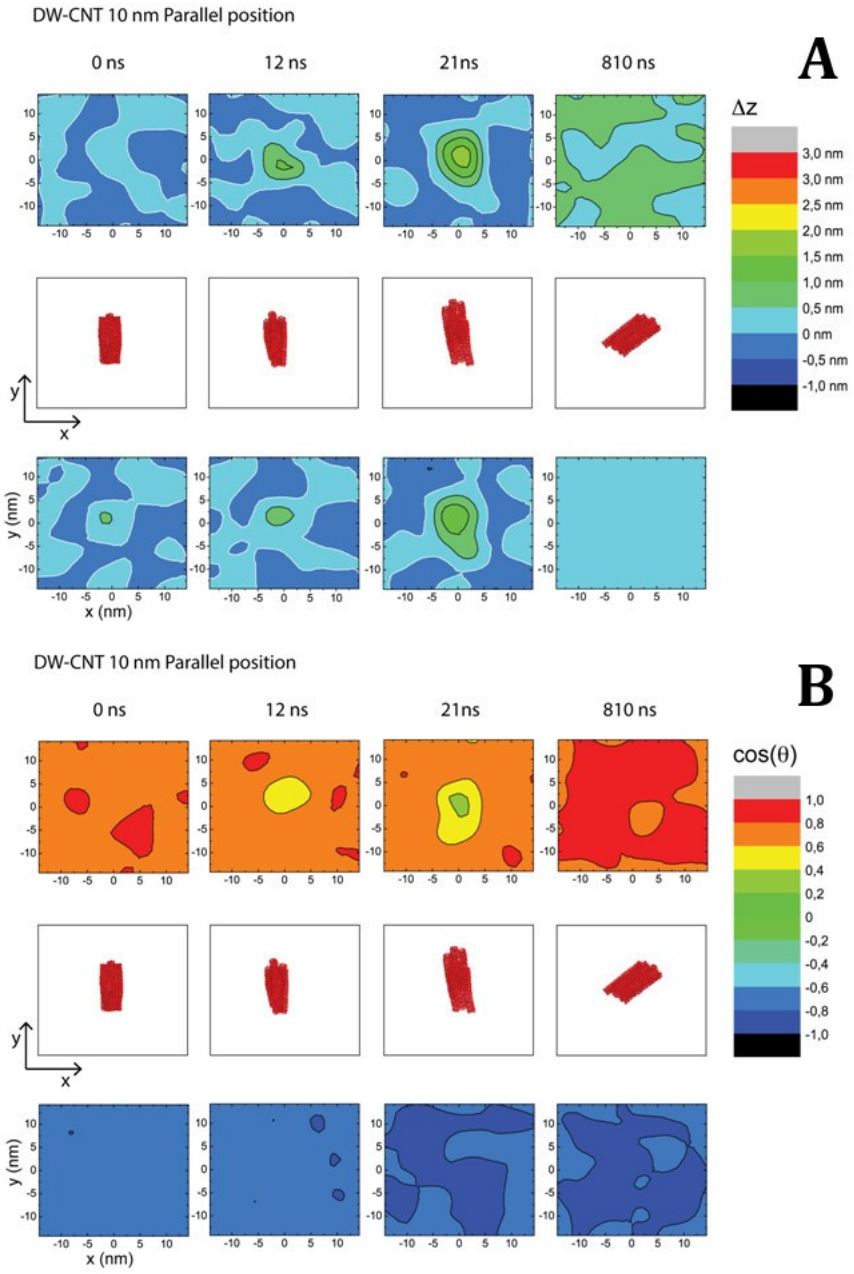

Figure 5.8: System II (bundle in parallel orientation). **A**) Deviation (Δz) from the equilibrium height for upper (top of figure) and lower lipid layers (bottom of figure) for different configurations. **B**) Lipid orientation cosθ. In the center of both figures **A** and **B** the corresponding configurations of CNT bundle are depicted.

During the simulation, having as starting configuration the CNT bundle oriented in perpendicular orientation it is possible to observe spontaneous insertion. The process is slower (about 200 ns against less than 100 ns for the parallel orientation). Comparing the plots of Figure 5.9 A and C and the snapshots reported in Figure 5.9 it is possible to observe that the insertion involves mechanism a concerted insertion/rotation of the bundle. The perturbation of both lipid heights (with a region with Δz from 1 to 3 nm) and orientation (strong perpendicular orientation) is more localized but stronger than the one obtained with the bundle in parallel orientation.

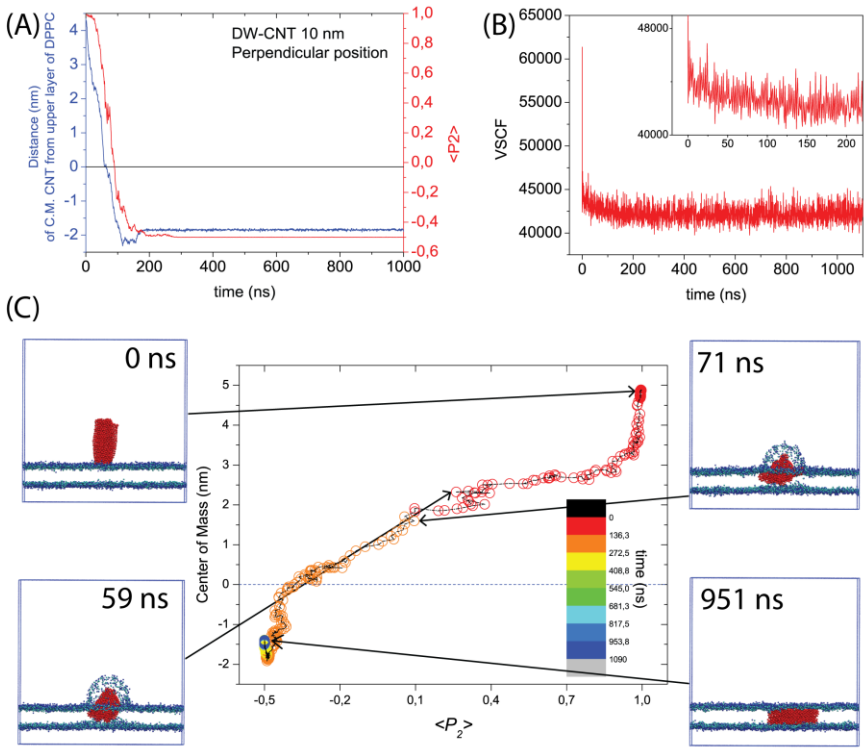

Figure 5.9: System II (bundle in perpendicular orientation). Time behavior of **A**) CNT bundle center of mass height (blue curve) and orientation (P_2, red curve); **B**) Particle field potential (second added of eq. 2) **C**) correlation between center of mass height and bundle orientation together with some snapshots.

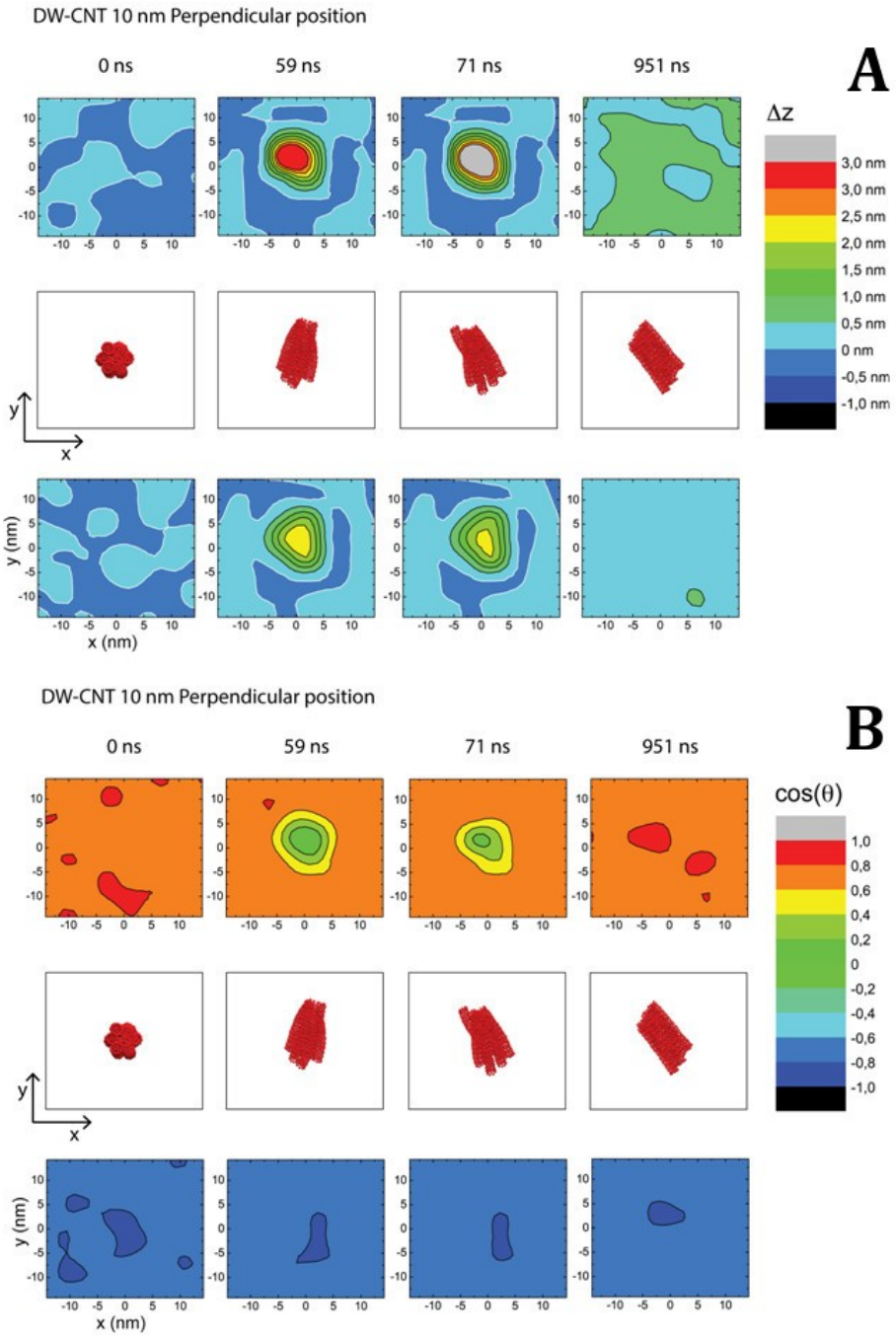

Figure 5.10: System II (bundle in perpendicular orientation). **A**) Deviation (Δz) from the equilibrium height for upper (top of figure) and lower lipid layers (bottom of figure) for different configurations. **B**) Lipid orientation cosθ. In the center of both figures **A** and **B** the corresponding configurations of CNT bundle are depicted.

As shown in Figure 5.11, the behavior of the system having a bundle made of CNTs long 20 nm (system III) is similar for both parallel and perpendicular orientations of the bundle. In comparison with the system II (CNTs 10 nm long), the insertion of bundle parallel to the bilayer is slower (Figure 5.11 A) and the orientation of the bundle is more strictly parallel (Figure 5.11 C) to the bilayer plane during the entire insertion process.

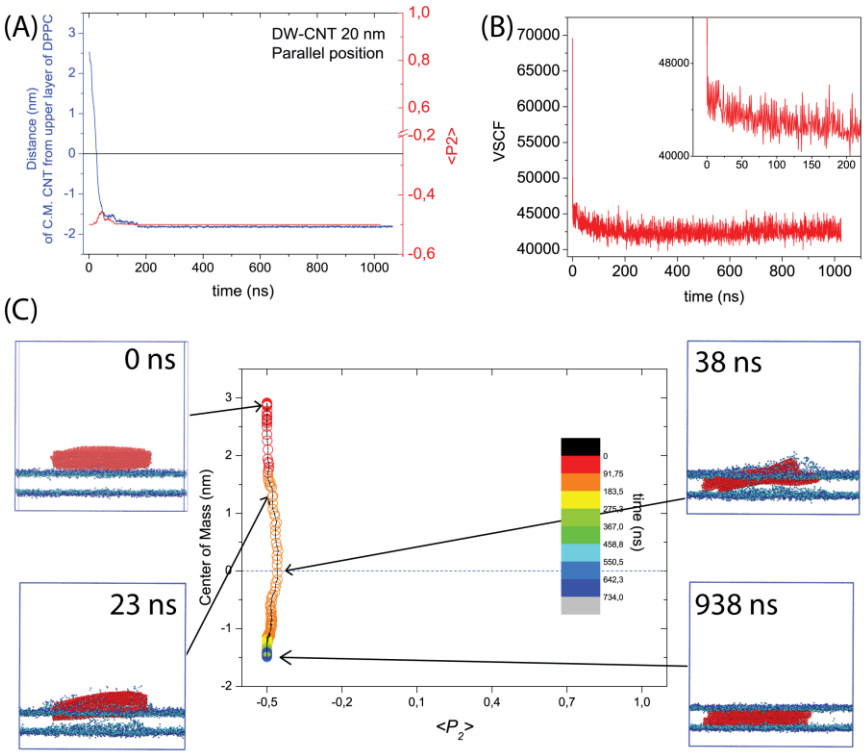

Figure 5.11: System III (bundle in parallel orientation). Time behavior of **A**) CNT bundle center of mass height (blue curve) and orientation (P_2, red curve); **B**) Particle field potential (second added of eq. 2.2.4, see Computational Methods part) **C**) correlation between center of mass height and bundle orientation together with some snapshots.

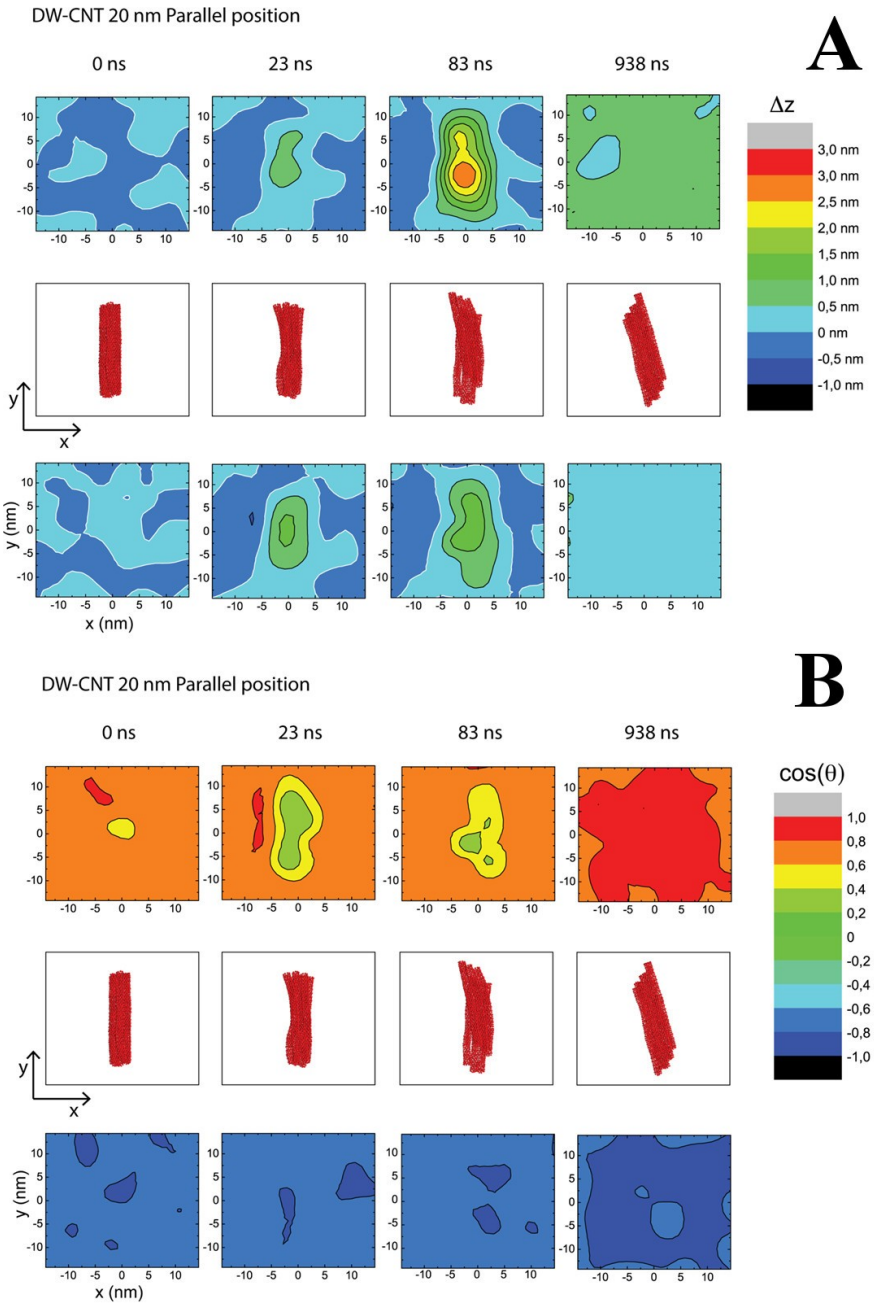

Figure 5.12: System III (bundle in parallel orientation). **A**) Deviation (Δz) from the equilibrium height for upper (top of figure) and lower lipid layers (bottom of figure) for different configurations. **B**) Lipid orientation cosθ. In the center of both figures **A** and **B** the corresponding configurations of CNT bundle are depicted.

As shown in Figure 5.12 A in this case, the region having large lipid displacement is larger and comparable with CNTs length. In the plot of Figure 5.12 A corresponding to the configuration at 37.8 ns it is possible to observe a region with a displacement between 2 and 3 nm. A similar behavior can be observed (see Figure 5.12 B) also for lipids orientation during the insertion process.

The insertion process involving a CNT bundle in perpendicular orientation is the one showing the largest perturbation on the structure of the lipid bilayer. In particular, as shown in Figure 5.13 A and C, the concerted insertion/rotation of the CNT bundle is slower than the corresponding process for system II having shorter (10 nm) CNTs. From the snapshots reported in Figure 5.13 it is clear that there is a large displacement of lipids towards the CNT wall. This displacement and the corresponding orientation of lipids pointing toward the CNT surfaces the hydrophobic carbon tails is able to minimize the contacts between the CNT surface and the water phase. Differently from other systems considered here, in this case the intermolecular interactions (see the behavior of particle-field potential reported in Figure 5.13 C) does not show a monotonic decrease, but between 100 and 200 ns shows a local maximum.

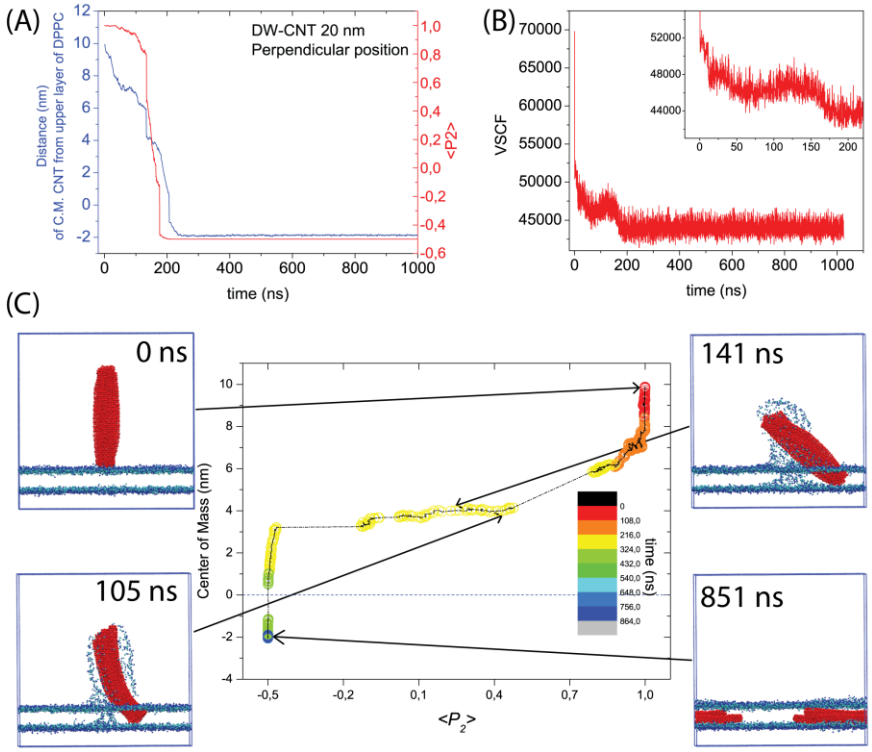

Figure 5.13: System III (bundle in perpendicular orientation). Time behavior of **A**) CNT bundle center of mass height (blue curve) and orientation (P_2, red curve); **B**) Particle field potential (second addend of eq. 2.2.4, see Computational Methods section, **Chapter 2**) **C**) correlation between center of mass height and bundle orientation together with some snapshots.

The displacement of lipids is quite large in comparison with the systems with shorter CNTs. In particular, as reported in the plots of Figure 5.14 A the value of Δz can be also as large as 7 nm. These strong perturbations involve also the lower layer. The orientation of lipids is strongly perpendicular corresponding to time interval between 105 and 141 ns (see Figure 5.14 B).

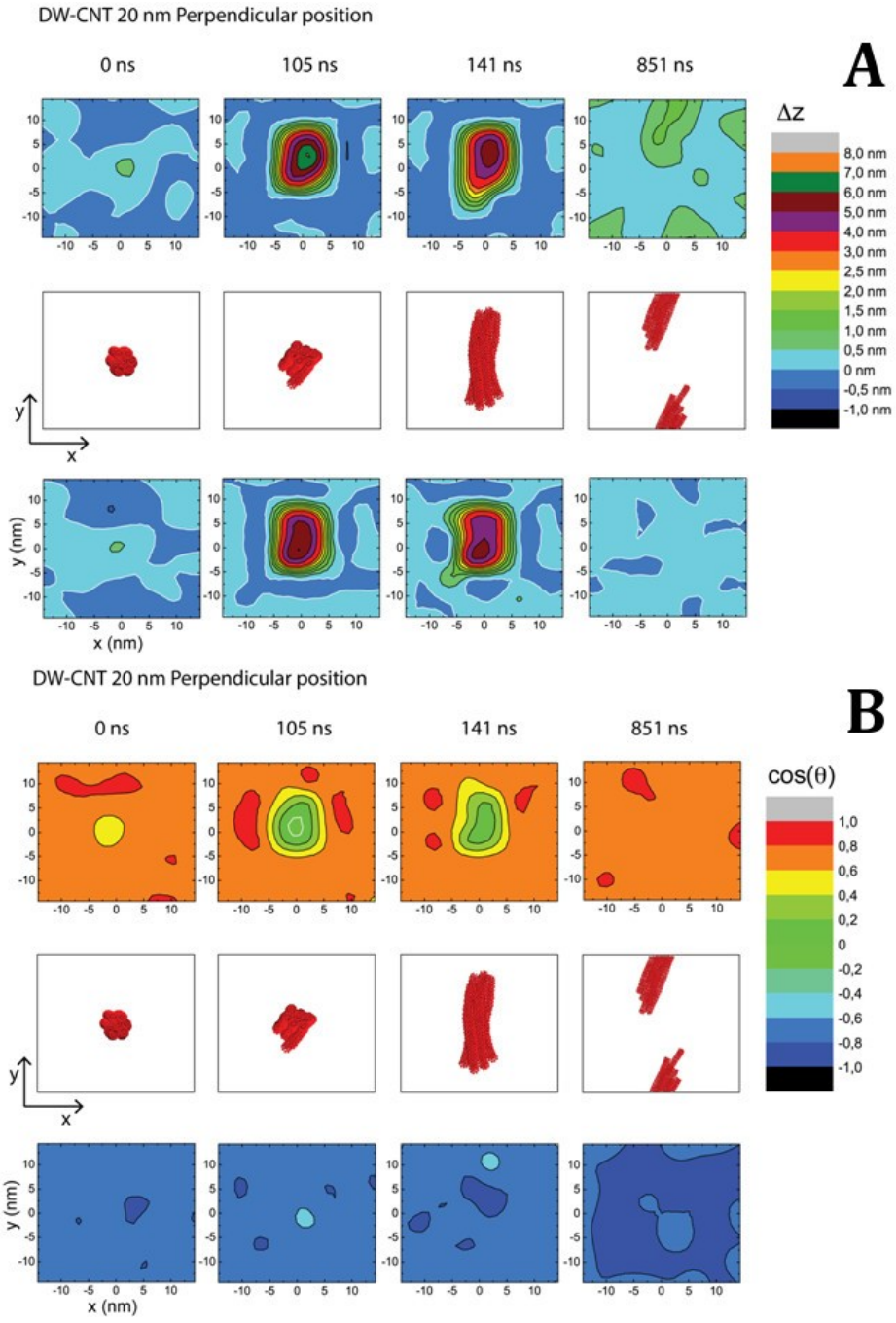

Figure 5.14: System III (bundle in perpendicular orientation). **A**) Deviation (Δz) from the equilibrium height for upper (top of figure) and lower lipid layers (bottom of figure) for different configurations. **B**) Lipid orientation cosθ. In the center of both figures **A** and **B** the corresponding configurations of CNT bundle are depicted.

In Figure 5.15 snapshots showing the coating process of lipids toward the CNT surfaces are shown.

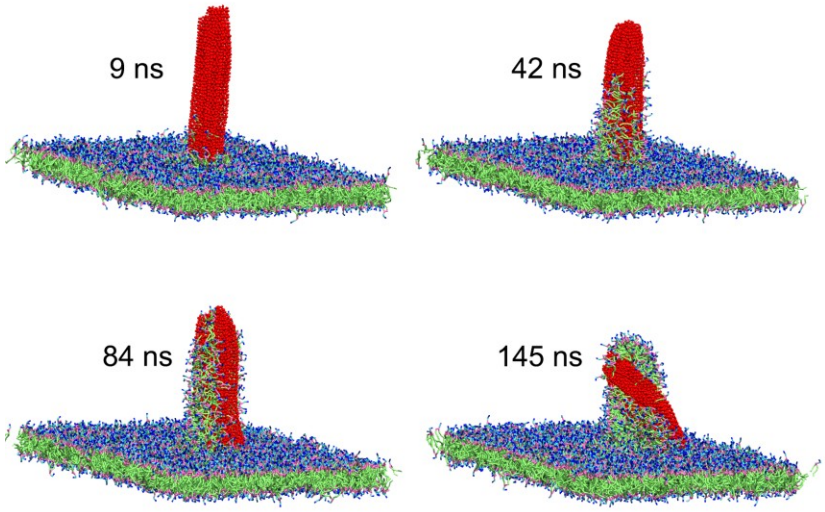

Figure 5.15: Snapshots showing the coating process of lipids attached to the CNT surfaces.

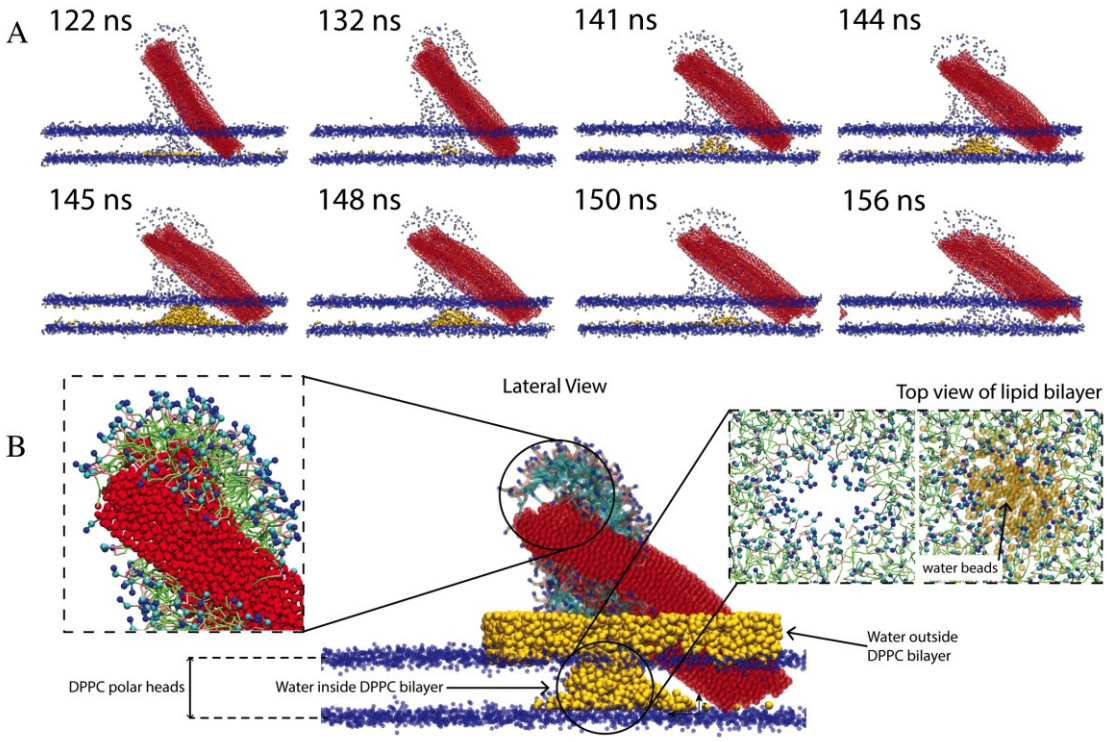

Figure 5.16: A) Process of pore formation inside the lipid bilayer during the insertion process of a bundle made of CNTs long 20 nm. B) The lipid orientations corresponding to micelle in water around the CNTs (inset on the left side) and reverse micelle (around the pore including water) aggregates (right side) are highlighted.

Another interesting aspect is the formation of a transient pore in the lipid bilayer during the insertion process of the CNT bundle. In particular, as shown in Figure 5.16 A, starting from the configuration at 123 ns a poration inside the bilayer can be observed. In the figure in yellow the water beads are reported. In this way it is possible to observe water permeation inside the pore with a maximum amount of water for the configurations around the one at 145 ns. Interestingly, this time corresponds to the maximum of particle-field potential (see Figure 5.13 B). In the Figure 5.16 B the structure of the water pore and the arrangement of lipids on the CNTs surface and around the pore percolated by water are highlighted. In particular, the arrangement on CNT surface is typical of phospholipids at low concentration in water (micellar phases), while the ones around the pore inside the hydrophobic region of the bilayer are closer to the one obtained

at high lipid concentration (reverse micelles) having lipids forming reverse micelles with water inside.

5.5 CONCLUSIONS

In all considered systems it has been possible to observe spontaneous insertion of bundles made of CNTs of different lengths ranging from 4.6 to 20 nm. In all cases the insertion process causes distortions in both lipid height and orientations. In particular, during the insertion process lipid molecules tend to coat bundles' surfaces and this causes an increase of the average lipids heights in both upper and lower lipid layers. The lipids closer to the bundle tend to orient their carbon tails toward the hydrophobic surfaces of CNTs. These distortions are more pronounced for systems having long CNTs and oriented perpendicularly to the bilayer surfaces. In all cases these distortions are transient and they become minimal when the CNTs forming the bundle rearrange inside the hydrophobic region of the lipid bilayers. Interestingly, in the case of the bundle made of CNTs long 20 nm it has been possible to observe a transient poration of the lipid bilayer and a subsequent water percolation through the bilayer.

5.6 ACKNOWLEDGEMENTS:

I would like to acknowledge Antonio De Nicola for the part of contribution to the work presented in the current chapter. In particular, for the performed analysis related to correlation between bundles' centre of mass and their orientation and for the writing codes to perform the analysis.

5.7 REFERENCES

(1) Lacerda, L.; Bianco, A.; Prato, M.; Kostarelos, K. *Advanced drug delivery reviews* **2006**, *58*, 1460.

(2) Kostarelos, K.; Lacerda, L.; Pastorin, G.; Wu, W.; Wieckowski, S.; Luangsivilay, J.; Godefroy, S.; Pantarotto, D.; Briand, J.-P.; Muller, S. *Nature Nanotechnology* **2007**, *2*, 108.

(3) Yang, W.; Thordarson, P.; Gooding, J. J.; Ringer, S. P.; Braet, F. *Nanotechnology* **2007**, *18*, 412001.

(4) Sinha, N.; Yeow, J.-W. *NanoBioscience, IEEE Transactions on* **2005**, *4*, 180.

(5) Pantarotto, D.; Singh, R.; McCarthy, D.; Erhardt, M.; Briand, J. P.; Prato, M.; Kostarelos, K.; Bianco, A. *Angewandte Chemie* **2004**, *116*, 5354.

(6) Pantarotto, D.; Briand, J.-P.; Prato, M.; Bianco, A. *Chemical Communications* **2004**, 16.

(7) Kam, N. W. S.; Dai, H. *Journal of the American Chemical Society* **2005**, *127*, 6021.

(8) Foldvari, M.; Bagonluri, M. *Nanomedicine: Nanotechnology, Biology and Medicine* **2008**, *4*, 183.

(9) Tripisciano, C.; Kraemer, K.; Taylor, A.; Borowiak-Palen, E. *Chemical Physics Letters* **2009**, *478*, 200.

(10) Liu, G.; Cheng, Y.; Mi, D.; Li, Z. *International Journal of Modern Physics C* **2005**, *16*, 1239.

(11) Kang, Y.; Liu, Y.-C.; Wang, Q.; Shen, J.-W.; Wu, T.; Guan, W.-J. *Biomaterials* **2009**, *30*, 2807.

(12) Al-Jamal, K. T.; Nerl, H.; Muller, K. H.; Ali-Boucetta, H.; Li, S.; Haynes, P. D.; Jinschek, J. R.; Prato, M.; Bianco, A.; Kostarelos, K.; Porter, A. E. *Nanoscale* **2011**, *3*, 2627.

(13) Porter, A. E.; Gass, M.; Muller, K.; Skepper, J. N.; Midgley, P. A.; Welland, M. *Nature Nanotechnology* **2007**, *2*, 713.

(14) Porter, A. E.; Gass, M.; Bendall, J. S.; Muller, K.; Goode, A.; Skepper, J. N.; Midgley, P. A.; Welland, M. *ACS nano* **2009**, *3*, 1485.

(15) Zhou, F.; Xing, D.; Wu, B.; Wu, S.; Ou, Z.; Chen, W. R. *Nano letters* **2010**, *10*, 1677.

(16) Lamprecht, C.; Liashkovich, I.; Neves, V.; Danzberger, J.; Heister, E.; Rangl, M.; Coley, H. M.; McFadden, J.; Flahaut, E.; Gruber, H. J. *Nanotechnology* **2009**, *20*, 434001.

(17) Yaron, P. N.; Holt, B. D.; Short, P. A.; Losche, M.; Islam, M. F.; Dahl, K. N. *J Nanobiotechnology* **2011**, *9*, 45.

(18) Gangupomu, V. K.; Capaldi, F. M. *Journal of Nanomaterials* **2011**, *2011*.

(19) Höfinger, S.; Melle-Franco, M.; Gallo, T.; Cantelli, A.; Calvaresi, M.; Gomes, J. A.; Zerbetto, F. *Biomaterials* **2011**, *32*, 7079.

(20) Parthasarathi, R.; Tummala, N.; Striolo, A. *The Journal of Physical Chemistry B* **2012**, *116*, 12769.

(21) De Nicola, A.; Zhao, Y.; Kawakatsu, T.; Roccatano, D.; Milano, G. *Journal of Chemical Theory and Computation* **2011**, *7*, 2947.

(22) Zhao, Y.; De Nicola, A.; Kawakatsu, T.; Milano, G. *Journal of Computational Chemistry* **2012**, *33*, 868.

(23) Milano, G.; Kawakatsu, T. *The Journal of chemical physics* **2009**, *130*, 214106.

(24) Marrink, S. J.; Lindahl, E.; Edholm, O.; Mark, A. E. *Journal of the American Chemical Society* **2001**, *123*, 8638.

(25) Frenkel, D.; Smit, B. *Understanding molecular simulation: from algorithms to applications*; Access Online via Elsevier, 2001.

(26) Marrink, S. J.; Risselada, H. J.; Yefimov, S.; Tieleman, D. P.; de Vries, A. H. *Journal of Physical Chemistry B* **2007**, *111*, 7812.

CHAPTER 6:

Atomistic Simultions of Cecropin A-Magainin 2 Hybrid Prptide in Water Solutions

CHAPTER 6

ATOMISTIC SIMULATIONS OF CECROPIN A – MAGAININ 2 HYBRID PEPTIDE IN WATER SOLUTIONS

6.1 ABSTRACT

Antimicrobial peptides are promising alternative to traditional antibiotics for the battle against new antibiotic resistant bacteria strains and cancer. Therefore it is important to understand their structural and dynamical properties under physiological conditions. In this chapter, the effects of temperature, ionic strengh and solute concentration on these properties for the antimicrobial hybrid peptide Cecropin A – Magainin 2 have been studied by MD simulations. The results of the simulations indicate on dependence of the residual amount of secondary structure (α-helix) with the ionic strength of the solution. More relevant stabilizing effect on the secondary structure was also observed with the raise of the peptide concentration that significantly reduce the unfolding kinetics of the α-helix structure present in the peptide at the beginning of the simulations.

CHAPTER 6

6.2 INTRODUCTION

Peptides with antimicrobial activity are found in a broad variety of organisms, including mammals, amphibians, and insects.[1-7] It has been recognized that these peptides play an important role in the host defense system and its innate immunity. For this reason, they are considered as possible alternative to traditional antibiotics for the battle against new drug resistant bacteria strains and cancer cells.[8-10] In the quest for new peptides with improved antibacterial and anticancer activities but without toxic effects on healthy eukaryotic cells, the use of systematic combinatorial methods resulted in the synthesis of hybrid peptides.[11-13] Among these new artificial peptides, those from the combination of the Cecropin A (CA) and the Magainin 2 (MA) peptide, have shown promising anticancer and antibacterial activity.[11-13]

CA is a 37 amino acids antimicrobial peptide present in the hemolymph of *Hyalophora cecropia* pupae,[2,4,11-12,14-16] and MA is 23 amino acids long peptide extracted from the skin of the African clawed frog, *Xenopus laevis*.[1,4-5,17-18] Both, CA and MA have strong lytic activities against Gram-positive and Gram-negative bacteria without toxic effects against eukaryotic cells, such as human erythrocytes.[1-2,4-5] Among the different hybrid peptides derived from CA and MA peptides, the one composed with the residues 1-8 from Cecropin A and the residues 1-12 from Magainin 2 (KWKLFKKI-GIGKFLHSAKKF-NH_2) showed better antibacterial and antitumor activity rather than the original CA or MA peptides.[13,19-20] The structure of the CA-MA peptide in solution was studied by NMR and Circular Dichroism (CD) for the peptide concentrations of 100 µg/ml.[13,21-22] The CD spectrum has shown that for CA-MA in phosphate buffer, the α-helix percentage is as low as 5.9 % while in 50 % trifluoroethanol (TFE) and 30 mM sodium dodecylsulphate (SDS) it increases up to 54.4% and 14.1%, respectively.[22] The available NMR structures of CA-MA hybrid peptide in dodecylphosphocholine micelles consists of two helices that are separated by a flexible hinge region containing G9-I10-G11 sequence.[19,22] This sequence is known to be flexible and plays an important role in providing the conformational flexibility required for ion channel formation in cell membrane.[19,22] Experimental results suggest that although the α-helical propensity of antimicrobial peptides can play a significant role in bactericidal and tumoricidal capabilities, the amount of α-helical content does not correlate with

their antibacterial and antitumor activities.[22] Indeed, some experimental works have found out that antibiotic and antitumor activities of CA-MA, mostly, depend on the presence of G9-I10-G11 hinge region.[19,22] This amino acid triplet in the middle part of the peptide provides conformational flexibility, which is relevant for antibiotic activity. In fact, deletion or substitution of G9-I10-G11 by G9-P10-G11 sequence resulted in decrease of bactericidal rate in *B.subtilis* and *E.coli* and anti-cancer activity against four different cancer cell lines.[19,22]

To understand the interaction mechanism with the cell membrane and to design delivery systems for this and other antibiotic peptides, it is relevant to know how ionic strength, temperature and peptide concentration influence structural and dynamical behaviors of the peptide in solution. Therefore, the aim of this work is to study the behavior of the CA-MA hybrid peptide in aqueous media at different ionic strength conditions, temperatures and peptide concentrations using MD simulations. MD is so far the best method to study disordered structures of peptides and small proteins in solution and, nowadays, it is possible to easily access time scales of several hundred nanoseconds at which these phenomena become interesting. In particular, single CA-MA peptide in pure water, in the presence of 150 mM NaCl (close to the concentration in the human blood plasma[23]) and at the temperatures of 300 and 310 K (37 ^{o}C, the average temperature of the human body). Recent computational studies have suggested the importance of the peptide aggregation in driving mechanism of pore formations in lipid bilayers.[24-25] Therefore, simulations with four CA-MA peptides have been additionally performed, keeping the same temperature and ionic strength conditions, as for the single peptide simulations, with the aim to understand how the peptides aggregate.

The chapter is organized as follows. In the Material and Methods section, the technical details of the MD simulations are provided. Thereafter, the results obtained out of the simulations of single and four CA-MA peptides in different conditions are reported. In the Discussion section, the results will be compared with the available experimental results and other simulations study on similar peptides. Finally, the summary and outlook of the work will be provided in the Conclusions section.

CHAPTER 6

6.3 MATERIAL AND METHOD

6.3.1 System Setup.

The starting coordinates of CA-MA hybrid peptide have been obtained from the average NMR structure of the peptide in trifluoroethanol-containing aqueous solutions (Protein Data Bank, entry code 1D9J).[21] The Simple Point Charge (SPC) model of water was used in all the simulations.[26] The GROMOS54a7[27] force field parameters were used for the modeling of the atomic interactions. The peptides were centered in cubic boxes of size 10 nm and the empty space was filled with water molecules by stacking an equilibrated box of 216 water molecules. The water molecules within 0.25 nm from the solute atoms were removed. Cl^- counter ions were added to keep the system neutral for the simulation boxes with 1 and 4 CA-MAs. Two set of simulation at different ionic strength were performed. In the low salt concentration (LSC) simulations, only Cl- ions were added to neutralize the positive charges on the peptide and neutralize the simulaton box. For the simulations at high salt concentration (HSC), extra Na^+ and Cl^- ions were added to obtain a final concentration of ~150 mM (comparable to the concentration in the human blood serum[23]).

In addition, three simulation boxes with only NaCl solutions at the same concentrations as for the peptide systems were prepared to analyze the effect of the peptides on the dynamics properties of the ions. In Table 6.1, a summary of the composition and temperature conditions of the simulated systems is reported.

CHAPTER 6

Table 6.1: *Summary of the composition and temperature condition of the simulated systems.*

	Simulation Name	N° of Peptides	N° of Water molecules	N° of Na^+ ions	N° of Cl^- ions	T (K)
1	1W300	1	33082	0	8	300
2	1I300	1	32906	88	96	300
3	1I310	1	32906	88	96	310
4	4W300	4	32683	0	32	300
5	4I300	4	32509	87	119	300
6	4I310	4	32509	87	119	310
7	W300	0	33155	8	8	300
8	I300	0	33264	88	88	300
9	I310	0	33264	88	88	310

6.3.2 MD Simulations.

MD simulations were performed using GROMACS (version 4.5.5) software package. The LINCS algorithm[28] has been applied in order to constraint the bond lengths during the simulation. The integration time step was set equal to 2 fs. The temperature and pressure were maintained to the reference values (T=300 and 310 K, P=1bar) using the Berendsen thermostat and barostat[29] with coupling time constant of τ_T=0.1 ps for temperature and τ_p=0.5 ps for pressure, respectively. The isothermal compressibility of $4.5x10^{-5}$ bar^{-1} was used for all the simulation. Particle mesh Ewald (PME) method[30] was applied for the long-range interactions with a real space cutoff of 1 nm, a Fourier mesh spacing of 0.12 nm. The Lennard-Jones interactions were calculated using the cutoff of 1.4 nm. Description of the peptides in current simulations is related to experimental value of pH equal to 7. All the systems were energy minimized using steepest descent algorithm of at least 1000 steps in order to relax the system and remove too close contacts among atoms. Hence, the systems were gradually heated from 50 K up to the simulation temperature in 1 ns of simulation. After equilibration MD simulations were run for 500 ns for all the systems. Reference simulation box of water and NaCl only of the same concentrations as those with peptides were run for 10 ns.

6.3.3 Analysis of the Trajectories.

The VMD (version 1.9.1)[31] program was used to visualize the trajectories and create the figures in the thesis. Gromos clustering method[32] of the peptide conformations has been used to analyze the structural changes during the simulation. In this work a cutoff criterion of 0.25 nm on the backbone root mean square deviations (RMSD) among all the conformations in a trajectory is used to classify the structures in different clusters. A total of 10000 structures, sampled every 50 ps from the 500 ns trajectories, have been used for the analysis. The conformation with the least deviation from the other structures in the same cluster is considered as the representative one (median structure) of the cluster.

Secondary structure analysis has been performed referring to Kabsch and Sander's algorithm[33] and the diffusion coefficients were calculated using Einstein's relation.[34]

The radial distribution functions (RDFs) for the specific ion are calculated with respect to C-α atom of each amino acid residue and represented all together as two dimensional "heat" maps. In this representation the x-axis represents the distance from C-α atoms, the y-axis – the amino acids and the colors in these plots codify for the values of the RDF curves.

6.4 RESULTS

6.4.1 Structure of the Isolated Peptide in Solution

Figure 6.1 shows the changes of the CA-MA peptide secondary structures in pure water, 150 mM NaCl solution at T=300 K and 310 K during the simulation time. The percentage of secondary structure for the last 250 ns has been calculated and the data are presented as histogram bars plot on the right side of the figure. For the simulation 1W300 (Figure 6.1, top), a sharp decrease of α-helix structure for the first 15 amino acids occurs in the first 20 ns followed by the formation of β-hairpin conformation until the end of the simulation. The increase of the salt concentration reduces the kinetics of unfolding (Figure 6.1, second plot), with the results that the average helical content is 2.5 times higher than in the low salt concentration simulations. Finally, the increase of the temperature till 310 K resulted in irreversible loss of α-helicity also in the region 15-20 (see Figure 6.1, third plot). In this case the peptide has high contents of β-sheet, but very low contents of α-helix (see right side of Figure 6.1). The low amount of α-helix is in qualitative agreement with experimental CD data on the conformations of the peptide in solution.[13,19,22] In particular, the occurrence of 5.8 % of α-helicity in the case of simulation of the single peptide in water (Figure 6.1, first chart, violet column bar), is consistent with the value of 5.9 % reported from CD measurements of the CA-MA peptide in 10 mM sodium phosphate buffer (pH 7.2) at 25°C.[22] However, to the best of our knowledge, no experimental data of the peptide in high salt concentration has been reported in literature. Our model suggests that at 300 K and higher salt concentration rather than experimental the peptide retains more α-helical structure than at LSC. However, at HSC and 310 K (physiological conditions) the α-helix

disappears almost completely. Interestingly in all the simulations, the dominant secondary structure is the β-strand. We suppose that this conformation might be favorable for the peptide in aqueous solutions after being unfolded from its initial α-helix conformation.

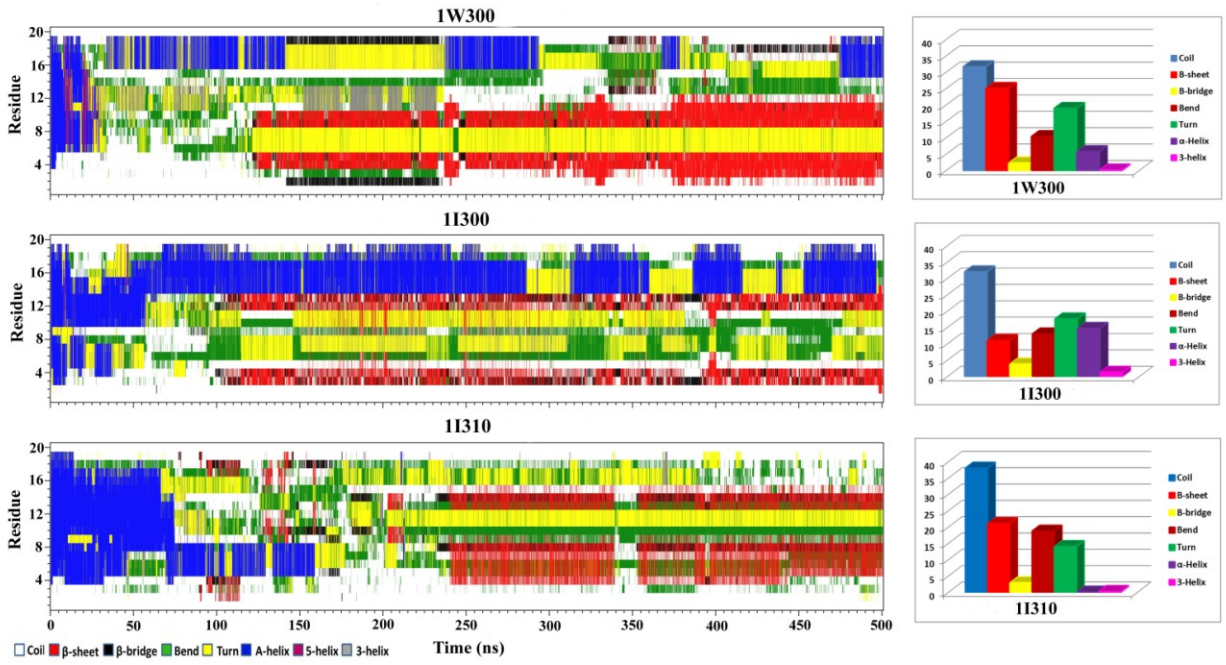

Figure 6.1: Secondary structures changes during the time for single peptide simulation in water at T=300 K (first plot), 150 mM NaCl solution at T=300 K (second plot) and at T=310 K (third plot). At the right side from the plots are shown percentages of average secondary structure for the corresponding simulations.

Cluster analysis has been performed for all single peptide simulations. In Figure S1 of Supporting Information (SI) the cumulative number of cluster is reported. In all the simulations the number of cluster converges to plateau (which means that there are no any new clusters), but at different simulations times. For the simulation 1I300 (red curve), the curve plateaus at 69 clusters after 150 ns. At higher temperature (green curve) a larger variety of conformations are generated and the curve start to plateau at 150 clusters after 250 ns. However, for the LSC simulation at low temperature (black curve), a temporary convergence at 69 clusters is observed and then it increases again to final plateau of ~125 clusters after 400 ns. In Figure 6.2, all representative structures (RS) of the first 5 clusters are reported. For the system 1W300, the most

abundant cluster contains 28% of total conformations with the median (representative) structure at time of 153 ns (see Figure 6.2, first column). The structure includes residues at positions L4, F5 and G9, I10 that form two β-strands with the turn region at positions K6, K7 and I8. A β-bridge is also observed at both N and C-terminals, including residues W2 and K19. The rest of the residues of the peptide adopt turn or bend structures. The second cluster contains 13.7% of the total conformations with the representative structure at 409 ns. The main secondary structure in the cluster consists, mainly, of two β-sheets, separated by turn. Finally, clusters 3, 4 and 5 contain together about 15% of total conformations. N-terminal region of the median structure of cluster 3 are shows random coil conformation, while the last 4 C-terminal residues form a α-helix structure, including last 4 amino acid residues. Median structures of clusters 4 and 5 present β-sheet secondary structure in the N-terminal regions and by β-turns in the middle. C-terminal region is composed of the residues forming α-helix for the cluster 4 and β-bridge for the cluster 5.

The population of conformers in the simulation 1I300 is represented by 71 % of total conformers by the first cluster (Figure 6.2, second column). The representative structure consists of a β-hairpin with two β-strands at positions K3, L4 and K12, F13 and α-helix at the C-terminal residues 15 – 19 (HSAKK). The clusters 2-5 contain in total only ~12.24 % of the total conformations and are populated in similar amount (~3%). The representative clusters show an abundance of beta-strands structures with the exception of cluster 2 and 5 in which a segment of a-helix is present at positions 13-19 (FLHSAKK) and 10-14 (IGKFL), respectively.

In the third column Figure 6.2, the representative cluster structures for the system 1I310 are reported. The population in the different clusters resembles the one from the 1W300 simulation. They have similar secondary structure composition. In particular, the presence of β-sheet formed by the residues at positions 4-8 (LFKKI) and 13, 14 (FL) with bend and turn regions in between. Amino acid residues localized near to the C-terminal for the structure of cluster 1 are in bend and turn conformations, whereas for the structure of cluster 2 amino acid residues are mostly in random coil conformations. For cluster 3 the representative structure is, mostly, random coiled with the exception of residues at positions 5 – 8 (FKKI) that form α-helix. The last two representative structures of clusters 4 and 5 are mainly in α-helical conformations. These

structures represent by themselves conformations of the peptide corresponding to the time frame of 44 and 48 ns, when the peptide still is in α-helix (see Figure 6.1 third plot).

Cluster No.	1W300	1I300	1I310
1	 28 % 153 ns	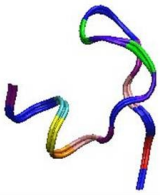 71 % 335 ns	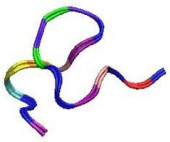 28.8 % 285 ns
2	 13.7 % 409 ns	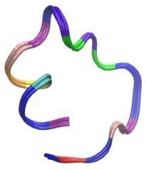 3.6 % 71 ns	 8.5 % 425 ns
3	 5.54 % 76 ns	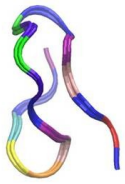 3.35 % 425 ns	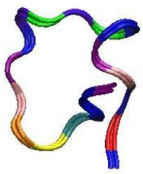 5.1 % 101 ns
4	 5.39 % 478 ns	 3 % 358 ns	 5.1 % 44 ns
5	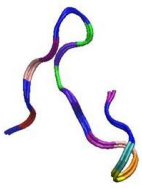 5 % 340 ns	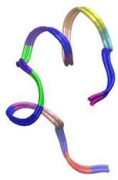 2.29 % 23 ns	 4.1 % 48 ns

Figure 6.2: First five representative structures obtained from cluster analysis out of the simulation of CA-MA hybrid peptide for the systems 1W300, 1I300 and 1I310. Color code for the amino acids in chain: K – blue, W – red, L – pink, F - magenta, I – green, G – violet, H – orange, S – yellow, A – cyan. Here N-terminal that starts with L is marked in blue, C – terminal, that has F is labeled in magenta.

Distribution of Ions around the Peptide. In Figure 6.3 the graph representing the RDFs of the Na^+, Cl^- ions and of the oxygen atoms (O_w) of water molecules are presented. The positions of the peaks of the RDF for the Cl^- ions show a tendency to bind the positively charged peptide. In particular, the Cl^- ions tend to localize in correspondence of the positively charged amino acids at positions 6, 7, 18, 19, at both 300 K and 310 K. In comparison, the RDFs for Na^+ and water oxygens do not show high localized peaks around the peptide.

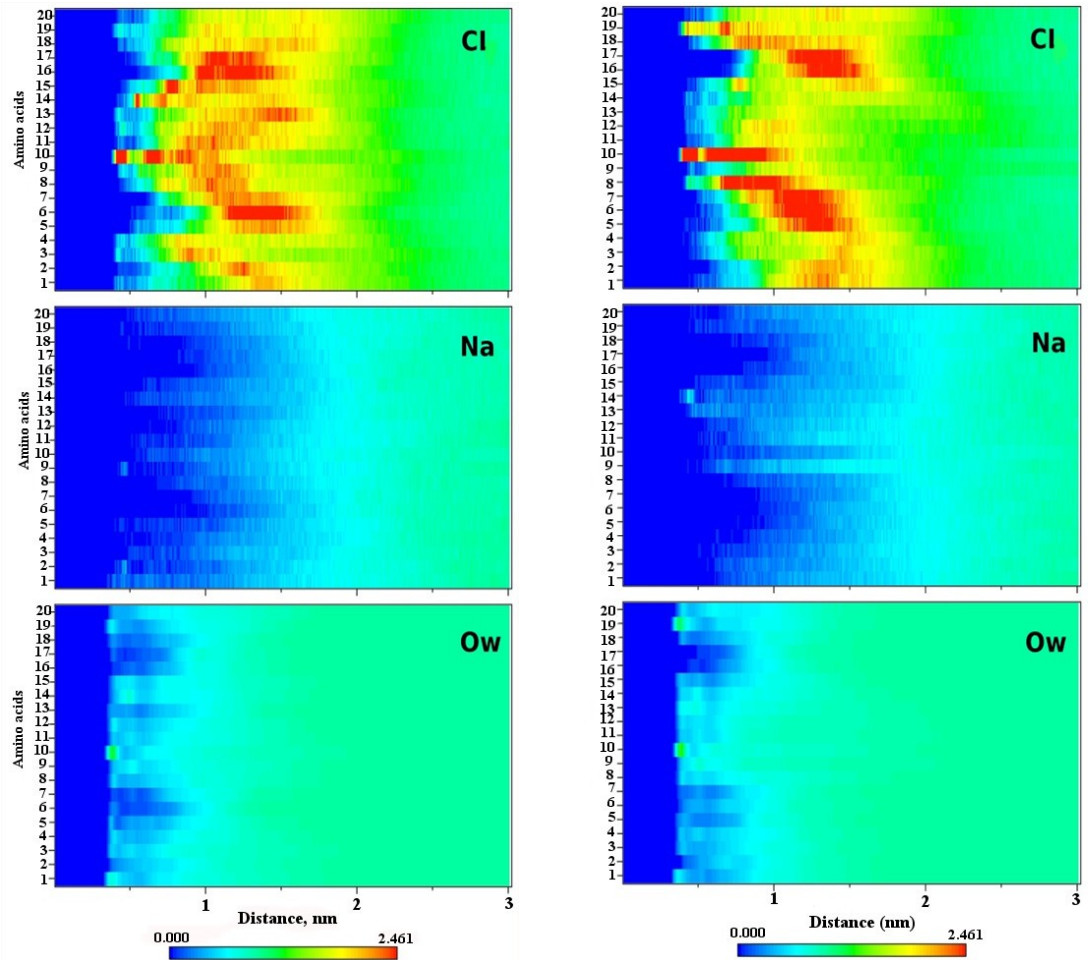

Figure 6.3: RDFs for the Cl^-, Na^+ and O_w respect to each residue of CA-MA peptide in 150 mM NaCl solutions at T=300 K (left) and T=310 K (right). The interval of color code for the RDFs starts from 0, the lowest value (shown in blue), up to 2.4 nm, the highest value (shown in red).

In Figure S2 of the SI, the Cl^-/Na^+ ratios (calculated for each amino acids using the number of ions within 1.5 nm) at low (blue curve) and high temperatures (red curve) compared the total box ratio (bulk ratio, black line) are reported. The ratios show that the average concentration of the Cl^- ions is 6.4 times larger than the bulk phase, which points out again on preferential binding of Cl^- ions in comparison to the Na^+ ions.

The diffusion coefficients of the ions have been calculated with and without the presence of peptide and the data is reported in Table 6.2. The presence of the peptide does not significantly change the value of diffusion coefficients for Na^+, Cl^- and O_w. For the Cl^- ions diffusion coefficients are slightly higher than for Na^+ ions. Diffusion coefficient increases with the increase of the temperature for all studied cases.

Table 6.2: *Diffusion coefficients for Na^+ and Cl^- ions in different conditions.*

D (10^{-5} cm^2/s)		**13 mM Cl-, T=300 K**	**150 mM NaCl, T=300 K**	**150 mM NaCl, T=310 K**
Na^+	Without peptide	1.98 ± 0.33	1.92 ± 0.04	2.12 ± 0.34
	1 peptide		1.82 ± 0.02	2.16 ± 0.05
	4 peptides		1.69 ± 0.04	2.19 ± 0.01
Cl^-	Without peptide	2.65 ± 0.33	2.22 ± 0.42	2.82 ± 0.30
	1 peptide	2.78 ± 0.41	2.52 ± 0.10	2.8 ± 0.01
	4 peptides	2.17 ± 0.08	2.14 ± 0.01	2.57 ± 0.13
O_w	Without peptide	4.54 ± 0.003	4.41 ± 0.02	5.14 ± 0.001
	1 peptide	4.49 ± 0.01	4.37 ± 0.005	5.12 ± 0.04
	4 peptides	4.43 ± 0.02	4.26 ± 0.01	5.027 ± 0.03

6.4.2 Peptide Aggregation.

Structural Properties of the Peptide. The effect of concentration on the structural and dynamical properties of CA-MA has been studied by simulation of 4 peptides in water solutions, keeping the same conditions as for the single peptide. In Figure S3 of SI the secondary structure variations along the simulations 4W300 are reported. Peptides 1 and 4 retain most of the α-helicity for all the simulation time. The peptide 2 loses the α-helical content after 430 ns and the peptide 3 after 85 ns. Figure 6.4 reports a quantitative analysis of the secondary structure for the last 250 ns. In the simulations, the concentration of the peptides is higher than in the experiments. This may explain the observed aggregation of the peptides during the simulations. In Figure 6.5 the minimum distances among the peptides using only the backbone atoms only are reported. The distance variations in Figure 6.5 A show the formation of two aggregation complexes one involving peptide 1 and 4 after 30 ns, and the other peptide 2 and 3 after 430 ns, respectively. It is interesting to note that for the 1-4 peptide complex the loss of α-helix structure is less in comparison to the 2-3 complex. It is evident that the peptide aggregation is playing a role in the stabilization of the peptide α-helix structure by delaying the unfolding kinetics.

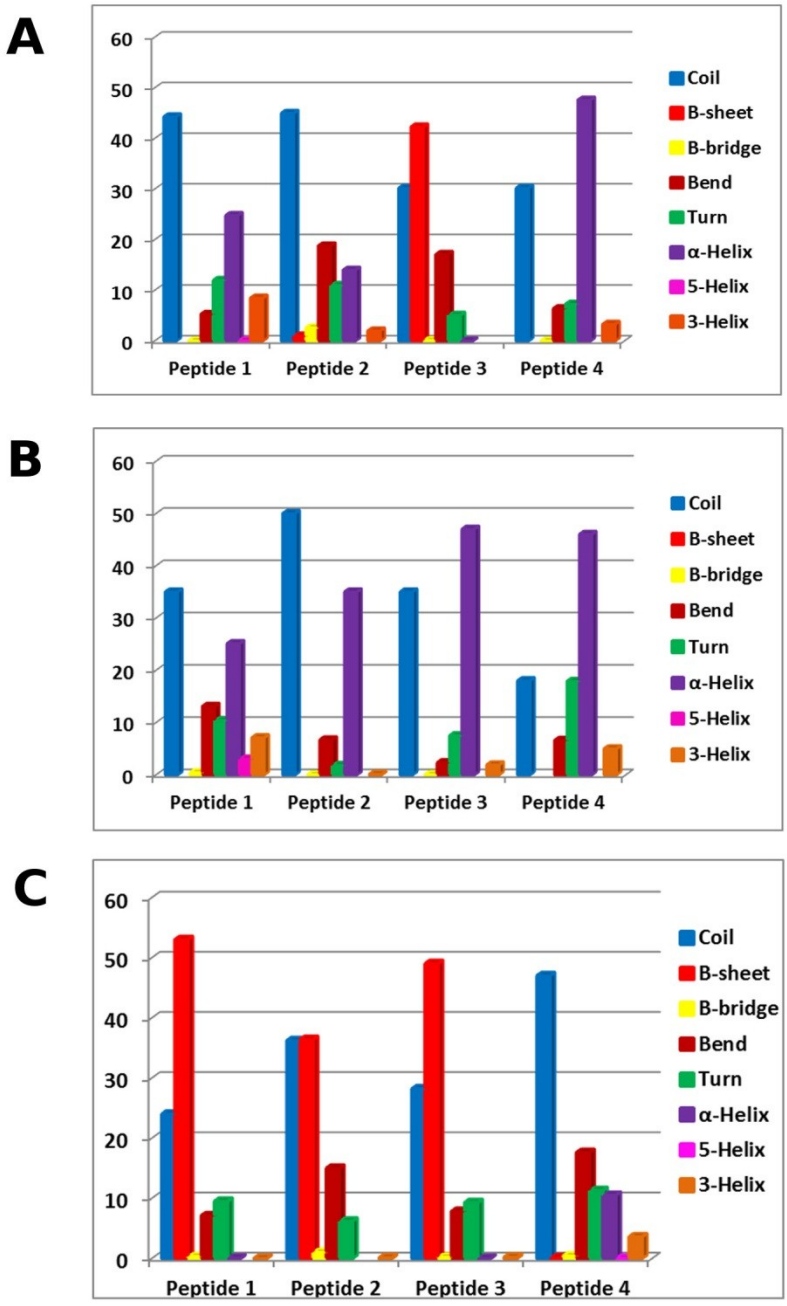

Figure 6.4: Percentages of average secondary structure for the simulation of 4 CA-MA peptides in water at T=300K (A), in 150 mM NaCl solution at T= 300 K (B) and at T = 310 K (C) for the last 250ns.

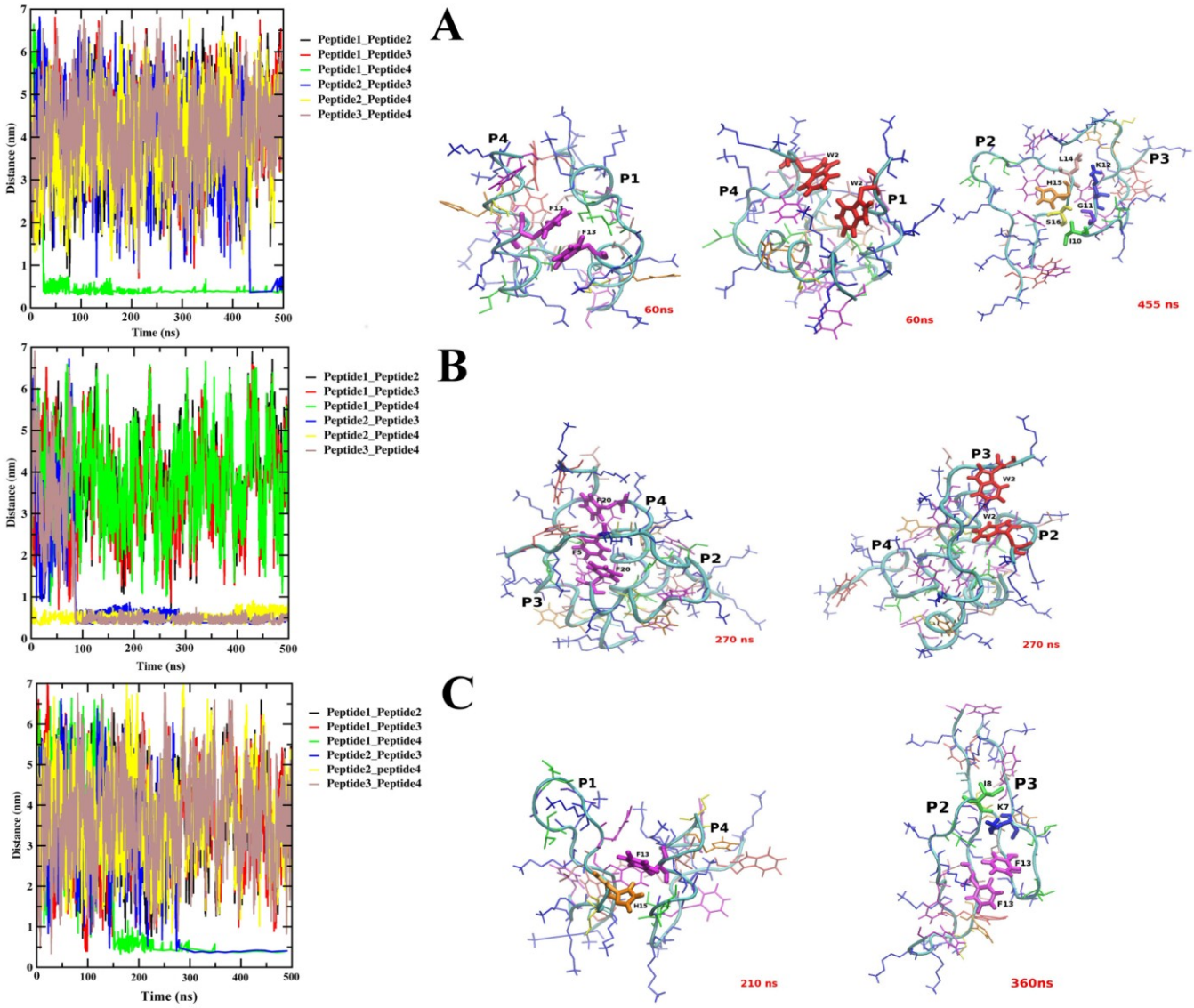

Figure 6.5: At the left side the minimum distance vs. time between the backbones of the peptides simulated in the system 4W300 (A), 4I300 (B) and 4I310 (C) are shown. At the right side representation of peptide aggregated conformations from the simulation 4W300, 4I300 and 4I310, respectively, are presented. In licorice are highlighted amino acids, involved in contacts between the peptide pairs.

In the 4I300 simulation (Figure 6.5 B), an aggregate of three peptides is formed at the end of the simulation. Peptide 2 and 4 are forming an aggregate almost from the beginning of the simulation, and, after 90 ns, also the peptide 3 joins the complex (see Figure 6.5 B). Also in this case the aggregation prevents the unfolding of the initial α-helix structure (see Figure 6.4 B, violet bars and Figure S4 SI), but more effectively than for the peptides at LSC (Figure 6.4 A and Figure S3 in SI). These results suggest that high salt and peptide concentration can cooperatively stabilize α-helix structure in this peptide.

The increase of the temperature by 10 K results in a loss of α-helicity and favors formation of β-sheet (Figure S6 SI and Figure 6.4 C). In this case two aggregates are formed by peptide 1 with peptide 4 after 150 ns, and by peptide 2 with peptide 3 after 250 ns (see Figure 6.5 C). Interactions between the peptides for all studied systems occur, mostly, involving aromatic residues. In particular, between F13 – F13 and W2 – W2 for the peptide 1 and peptide 4 in the case of LSC simulation at 300 K (Figure 6.5 A, right side); between F5 – F20 – F20 for the peptides 2, 3 and 4, and W2 – W2 for the peptides 2 and 3 in the case of HSC simulation at 300 K (Figure 6.5 B, right side) and, finally, between H15 – F13 for the peptide 1 and peptide 4, F13 – F13 for the peptide 2 and 3 in the case of HSC simulation at 310 K (Figure 6.5 C, right side).

In Figure 6.6, the cumulative numbers of cluster along the different simulations for the case of high peptide concentration are reported. In the system 4W300, the number of clusters for peptides 1, 3 and 4 converge to different number of clusters (54, 85 and 25) at different simulation times, 350 ns, 120 ns and 25 ns, respectively. On the contrary, the number of clusters (red curve) for the peptide 2 is constantly growing along the simulation to reach the highest value of 222 clusters at the end of the simulation. Figure 6.8 B shows cumulative numbers of clusters vs. time for the system 4I300. Also in this case, three peptides evidenced a convergence to a plateau with the range number of clusters (40-78) comparable to cluster convergence plateaus in the 4W300 simulation. The peptide 4 (blue curve) converges after 150 ns to the lowest number of clusters (9) plateau.

Finally, for the system 4I310 (Figure 6.8 C), the minimum number of clusters 58 (peptide 1) is higher than the other two systems due to the higher temperature (black curve). Three of the peptides (1, 2 and 3) reach after ~200 ns a stable plateau. The number of clusters for the peptide continues to grow till the end of the simulation time.

The behavior of the curves for the case of high peptide concentration simulations compared with the one from single peptide simulations (see Figure S1 SI) is similar. In particular, the minimal number of clusters among the 4 peptides for the system 4W300 is above 20, for the system 4I300 – above 8 and for the system 4I310 – above 50 (see Figure 6.6). In the case of the single peptide the highest number of cluster is received for the system 1I310, which is similar to the system 4I310. Less numbers of clusters are in the case of 1W300 that is comparable with the system of 4W300. Finally, the least number of clusters has been obtained for the system 1I300 and this is compatible with the results for the system 4I300.

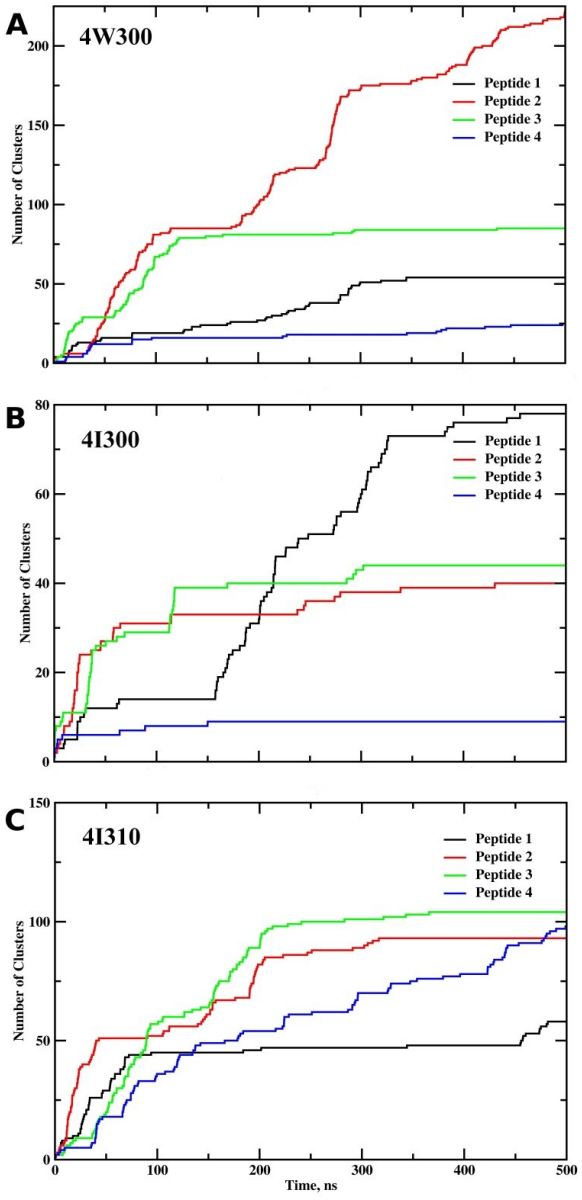

Figure 6.6: Cumulative number of clusters vs. time for the 4 CA-MA peptides simulations in different conditions.

In Figure 6.7 the representative structures of the most abundant cluster for each peptide in the different simulations are reported. If we compare structures, it can be observed that in 4W300 simulation, the peptides are mostly uncoiled, except the peptide 4, which sustains its α-helical content. However, in the 4I300 simulation, the peptides better preserve their initial helical content. Finally, for the 4I310 simulations the representative structures are mostly forming β-sheets, except the peptide 4, which is partially keeping helicity.

Peptide No.	4W300	4I300	4I310
1	 32 % 464 ns	 26 % 55 ns	 64 % 306 ns
2	 10.5 % 135 ns	 42 % 357 ns	 38 % 491 ns
3	 51 % 309 ns	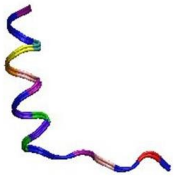 48 % 407 ns	 36 % 332 ns
4	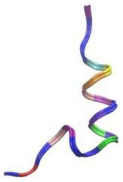 54 % 165 ns	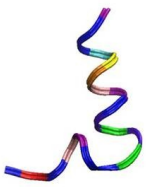 92 % 363 ns	 18 % 358 ns

Figure 6.7: Representative structures obtained from the cluster analysis out of the simulation of 4 CA-MA hybrid peptides in water at T=300 K, in 150 mM NaCl at T=300 K and at T=310 K. The color code is the same as in the case of simulation of single peptide (see Figure 6.2).

Distribution of Ions around the Peptides. In Figure 6.8, the RDFs of the ions around the each residues of 4 peptides simulation in HSC at 300 K are reported. The Cl^- ions tend to accumulate around the peptide 2, 3 and 4 depleting ions from the peptide 1 that does not aggregate. This effect is quantitatively shown by the Cl^-/Na^+ ratios in Figure S5 in SI that is higher for the peptides 2, 3 and 4 in comparison with the peptide 1. The ratios also show that for the peptide 1 the highest values correspond to the G and A residues at position 11 and 17, for the peptide 2 to the K and F at position 7 and 13, for the peptide 3, to the F, G and I residues at positions 5, 9 and 10, and for the peptide 4 to the residues L, A and K at positions 14, 17, 18, respectively.

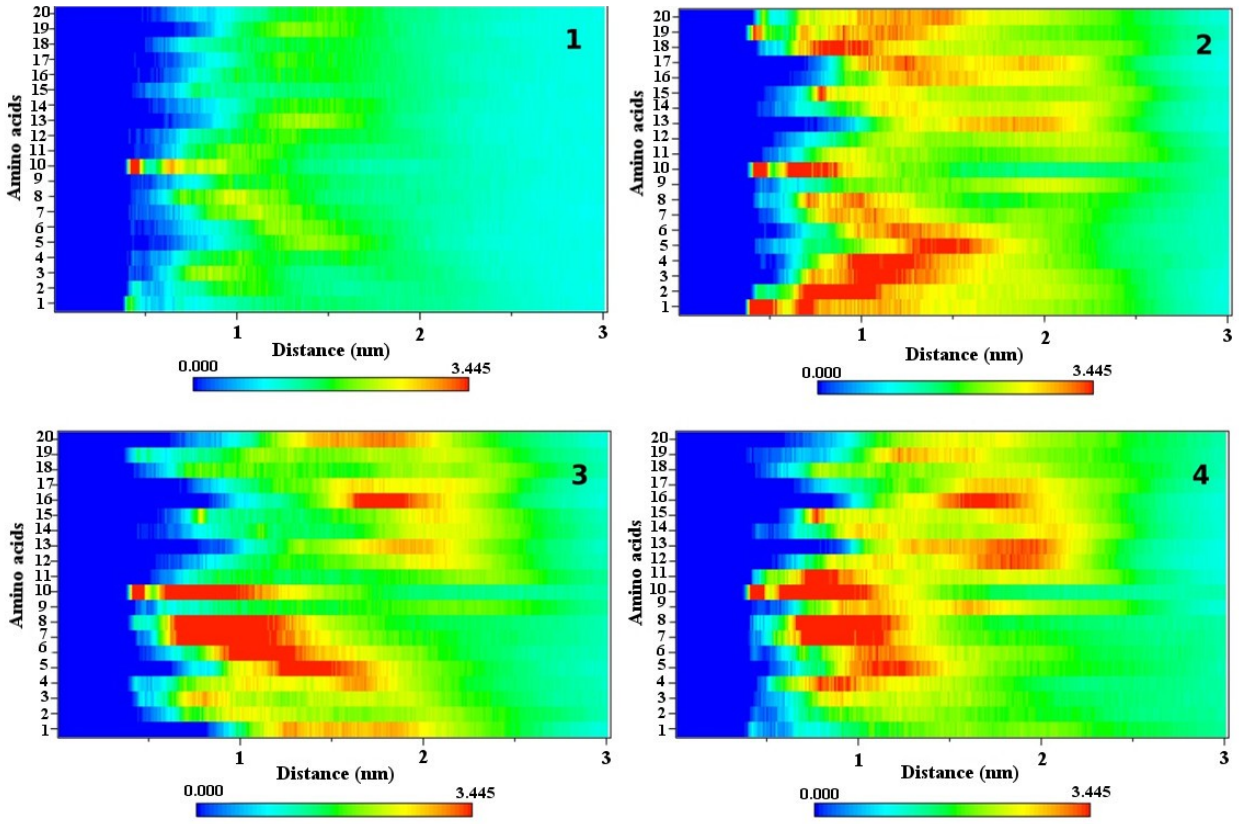

Figure 6.8: RDFs for the Cl^- ions respect to each residue of 4 CA-MA peptide simulations in 150 mM NaCl solution at T=300 K. The values of RDFs are within the interval of 0, shown in blue (the lowest value), up to 3.4, shown in red (the highest value).

In Figure 6.9 the RDFs of Cl^- ions respect to the residues of each peptide in the case of simulation at HSC at 310 K are reported. The preferential binding of the ions around the peptides 1, 2 and 3 is localized to the central residues while in the peptide 4 in the end regions. The multiple peaks in the distribution indicate the presence of peptide aggregates. The Cl^-/Na^+ ratios for the peptide 1, 2 and 3 (Figure S7 SI) present a minimum in the residues sequence 8-11 corresponding to the sequence IGIG, with the lowest value at positions 9 and 10 (G and I). On the contrary, the peptide 4 (not involved in the aggregate) has more constant values of the Cl^-/Na^+ ratio with a maximum for the G residue at position 10.

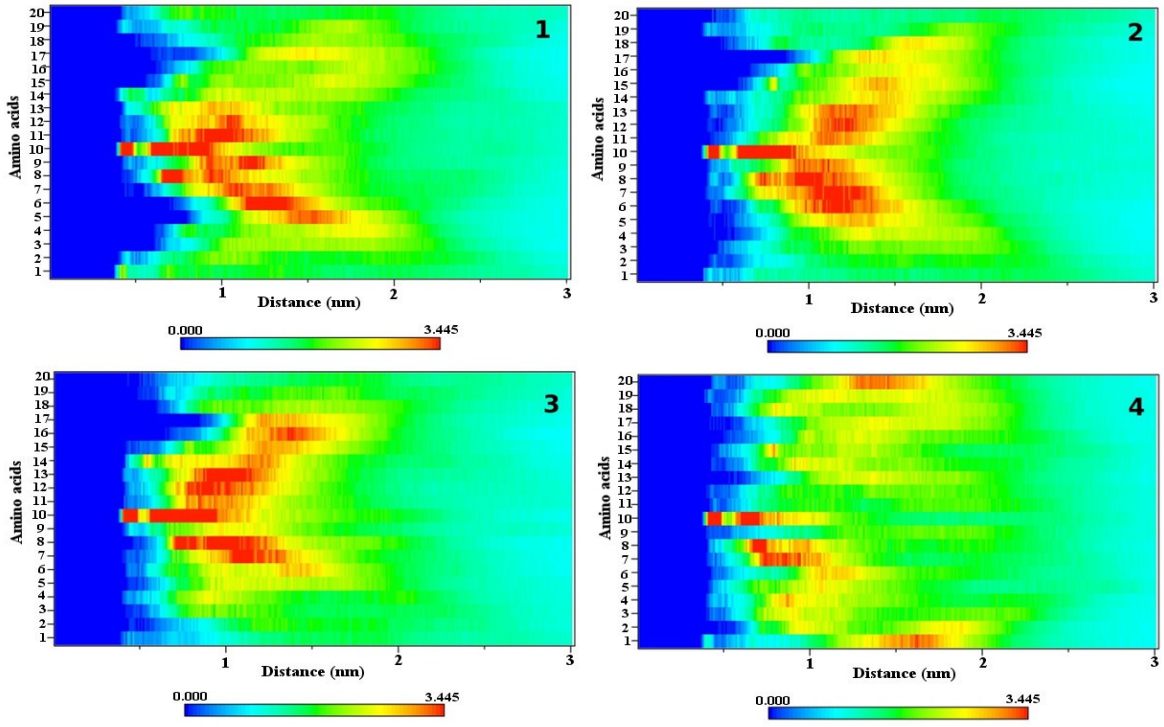

Figure 6.9: RDFs for the Cl^- ions respect to Cα atom of each residue of 4CA-MA peptide simulations in 150 mM NaCl solution at T=310 K.

CHAPTER 6

6.5 DISCUSSION AND CONCLUSIONS

The interaction of ions with peptide or protein structure is still not completely understood phenomenon. It is useful to know either it plays stabilizing or destabilizing role for the protein structure. There are several recent theoretical studies based on MD approach which are directed on understanding of salt effects on structure and dynamics of polypeptides.[35-38] Specificity of binding ions to a specific amino acid on a S6 ribosomal protein surface has been performed by simulation studies of Friedman.[37] Similarly to our results regarding to distribution of ions respect to CA-MA peptide, they have found that the probability of Cl^- ions to bind to the protein surface is higher in comparison with Na^+ when the concentration is close to physiological (120mM). They have also shown in their work that at higher concentration of 1M solution, there were no competing effect on bindings to the protein surface between the Cl^- and Na^+ ions. What is related to the effect of the salt on structural stability of the solute, Dzubiella et al.[38] performed MD simulations, where he studied an influence of high concentration (2.5-2.7 M) of NaCl, KCl, NaI, and KI on the α-helicity of alanine-based peptides. In overall, the results, found by Dzubiella, are indicating that all the salts, except NaI, are playing stabilizing role for the secondary structure.[38] In particular, an increase of α-helicity had place, when the solutes were placed in salty environment. This in turn is in accordance with our results, since in our case we have found an increase of α-helicity when simulation was performed in 150 mM NaCl for both, single and 4 CA-MA peptides, despite the concentration of the salt in our case is lower, than the one used by Dzubiella (2.7 M NaCl).

In conclusions, we have performed atomistic MD simulations of single CA-MA hybrid peptide in water, in 150 mM NaCL at T=300 K and at T=310 K. We studied the behavior of the peptide in these conditions and found out that peptide loses its α-helicity in water which is in accordance with experimental data. In salty environment such as 150 mM NaCL at T=300 K the peptide partially maintains its α-helical content, however, increasing the temperature by 10 K in the same solution, results in complete loss of α-helicity. Increasing peptide concentration in the same conditions as for the single one, leads towards aggregations. This, in turn, stabilizes the secondary structure.

CHAPTER 6

Here we have shown conditions (ionic strength, temperature and solute concentration) that play a role on structural stability of CA-MA peptide, knowing of which can be useful for better application of CA-MA peptide as an antibiotic or anticancer drug.

Studies have been performed in aqueous environment, were usually CA-MA receives random coil conformation. Further studies can be useful to be extended in membrane mimicking environments, where the peptide sustains its α-helical structure.

6.6 REFERENCES

(1) Bevins, C. L.; Zasloff, M. *Annual Review of Biochemistry* **1990**, *59*, 395.
(2) Boman, H. G. *Cell* **1991**, *65*, 205.
(3) Zasloff, M. *Curr. Opin. Immunol.* **1992**, *4*, 3.
(4) Boman, H. G. In *Annual Review of Immunology*; Paul, W. E., Ed.; Annual Reviews Inc. {a}, P.O. Box 10139, 4139 El Camino Way, Palo Alto, California 94306, USA: 1995; Vol. 13, p 61.
(5) Maloy, W. L.; Kari, U. P. *Biopolymers* **1995**, *37*, 105.
(6) Hancock, R. E. W.; Rozek, A. *FEMS Microbiol. Lett.* **2002**, *206*, 143.
(7) Brogden, K. A. *Nat. Rev. Microbiol.* **2005**, *3*, 238.
(8) Joerger, R. D. *Poultry Science* **2003**, *82*, 640.
(9) Sang, Y.; Blecha, F. *Animal Health Research Reviews* **2008**, *9*, 227.
(10) Hancock, R. E. W. *The Lancet* **1997**, *349*, 418.
(11) Steiner, H.; Hultmark, D.; Engstrom, A.; Bennich, H.; Boman, H. G. *Nature* **1981**, *292*, 246.
(12) Lee, J. Y.; Boman, A.; Sun, C. X.; Andersson, M.; Jornvall, H.; Mutt, V.; Boman, H. G. *Proc. Natl. Acad. Sci. U. S. A.* **1989**, *86*, 9159.
(13) Shin, S. Y.; Kang, J. H.; Lee, M. K.; Kim, S. Y.; Kim, Y. M.; Hahm, K. S. *Biochem. Mol. Biol. Int.* **1998**, *44*, 1119.
(14) Hultmark, D.; Steiner, H.; Rasmuson, T.; Boman, H. G. *Eur. J. Biochem.* **1980**, *106*, 7.
(15) Boman, H. G.; Faye, I.; Vonhofsten, P.; Kockum, K.; Lee, J. Y.; Xanthopoulos, K. G.; Bennich, H.; Engstrom, A.; Merrifield, R. B.; Andreu, D. *Dev. Comp. Immunol.* **1985**, *9*, 551.
(16) Lehrer, R. I.; Ganz, T. *Curr. Opin. Immunol.* **1999**, *11*, 23.
(17) Zasloff, M. *Proc. Natl. Acad. Sci. U. S. A.* **1987**, *84*, 5449.
(18) Soravia, E.; Martini, G.; Zasloff, M. *FEBS Lett.* **1988**, *228*, 337.
(19) Oh, D.; Shin, S. Y.; Lee, S.; Kang, J. H.; Kim, S. D.; Ryu, P. D.; Hahm, K.-S.; Kim, Y. *Biochemistry* **2000**, *39*, 11855.
(20) Bechinger, B. *Biochimica et Biophysica Acta (BBA) - Biomembranes* **1999**, *1462*, 157.
(21) Oh, D.; Kim, Y.; Shin, S. Y.; Kang, J. H.; Hahm, K. S.; Kim, K. L. *The Journal of Peptide Research* **1999**, *53*, 578.
(22) Shin, S. Y.; Kang, J. H.; Jang, S. Y.; Kim, Y.; Kim, K. L.; Hahm, K.-S. *Biochimica et Biophysica Acta (BBA) - Biomembranes* **2000**, *1463*, 209.
(23) Krebs, H. *Annual Review of Biochemistry* **1950**, *19*, 409.
(24) Sengupta, D.; Leontiadou, H.; Mark, A. E.; Marrink, S.-J. *Biochimica et Biophysica Acta (BBA)-Biomembranes* **2008**, *1778*, 2308.
(25) Leontiadou, H.; Mark, A. E.; Marrink, S. J. *Journal of the American Chemical Society* **2006**, *128*, 12156.
(26) Berendsen, H. J. C.; Postma, J. P. M.; van Gunsteren, W. F.; Hermans, J.; Pullman, B., Ed.; Reidel: Dordrecht: 1981, p 331.
(27) Schmid, N.; Eichenberger, A. P.; Choutko, A.; Riniker, S.; Winger, M.; Mark, A. E.; van Gunsteren, W. F. *European Biophysics Journal* **2011**, *40*, 843.
(28) Hess, B.; Bekker, H.; Berendsen, H. J. C.; Fraaije, J. G. E. M. *Journal of Computational Chemistry* **1997**, *18*, 1463.
(29) Berendsen, H. J. C.; Postma, J. P. M.; Vangunsteren, W. F.; Dinola, A.; Haak, J. R. *Journal of Chemical Physics* **1984**, *81*, 3684.
(30) Darden, T.; York, D.; Pedersen, L. *Journal of Chemical Physics* **1993**, *98*, 10089.
(31) Humphrey, W.; Dalke, A.; Schulten, K. *Journal of Molecular Graphics* **1996**, *14*, 33.

(32) Daura, X.; Gademann, K.; Jaun, B.; Seebach, D.; van Gunsteren, W. F.; Mark, A. E. *Angewandte Chemie International Edition* **1999**, *38*, 236.
(33) Kabsch, W.; Sander, C. *Biopolymers* **1983**, *22*, 2577.
(34) Allen, M. P.; Tildesley, D. J. *Computer simulation of liquids*; Oxford university press, 1989.
(35) Hess, B.; van der Vegt, N. F. *Proceedings of the National Academy of Sciences* **2009**, *106*, 13296.
(36) Xie, W. J.; Gao, Y. Q. *Faraday Discussions* **2013**, *160*, 191.
(37) Friedman, R. *The Journal of Physical Chemistry B* **2011**, *115*, 9213.
(38) Dzubiella, J. *The Journal of Physical Chemistry B* **2009**, *113*, 16689.

SUPPORTING INFORMATION

ATOMISTIC SIMULATIONS OF CECROPIN A – MAGAININ 2 HYBRID PEPTIDE IN WATER SOLUTIONS

CONTENTS

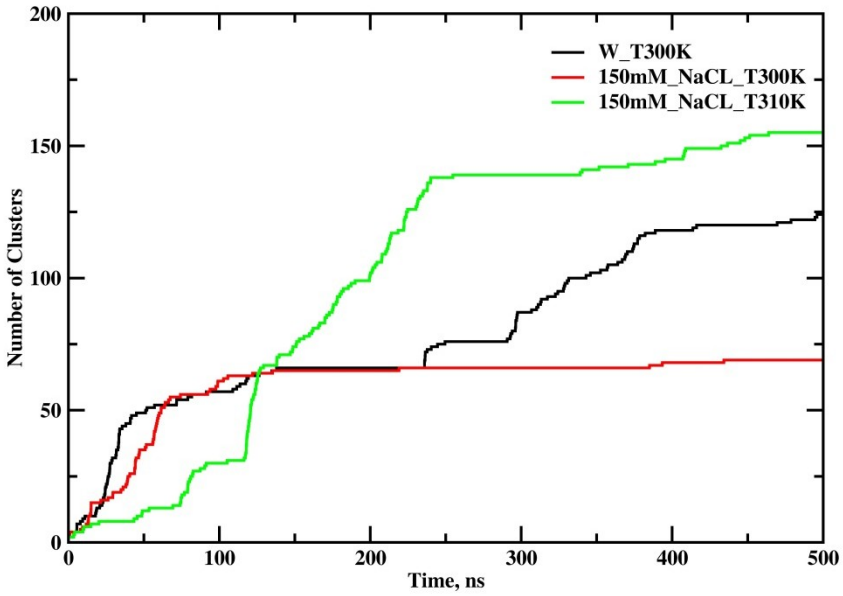

Figure S1: Cumilative number of clusters for the simulation of single peptide in water (green curve), 150 mM NaCl at T=300 K (red curve) and at T=310 K (green curve).

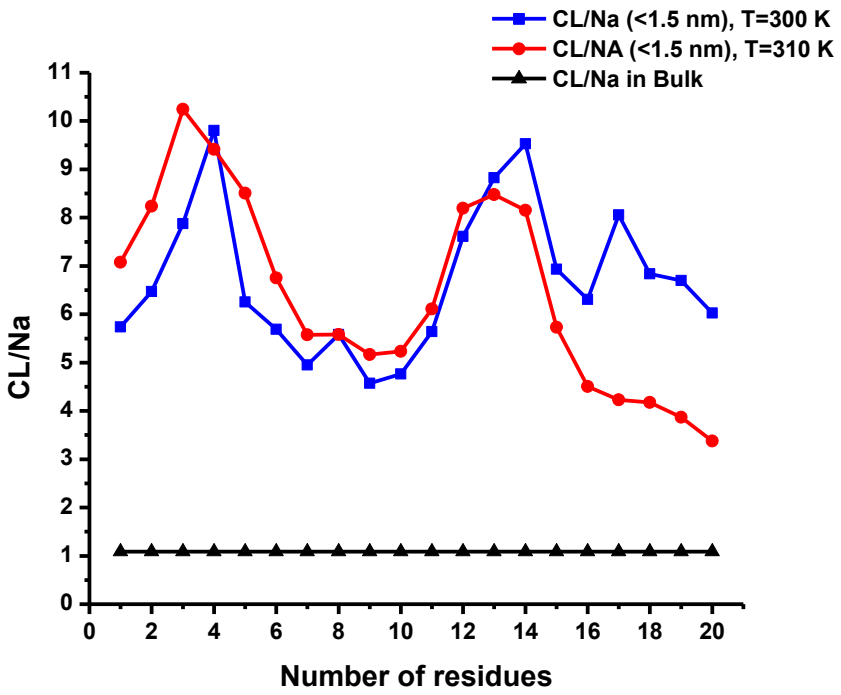

Figure S2: Cl/Na ratio respect to Cα atoms of each residue within 1.5 nm from the surface of CA-MA peptide in 150 mM NaCL solution at T=300 K (blue curve) and 310 K (red curve).

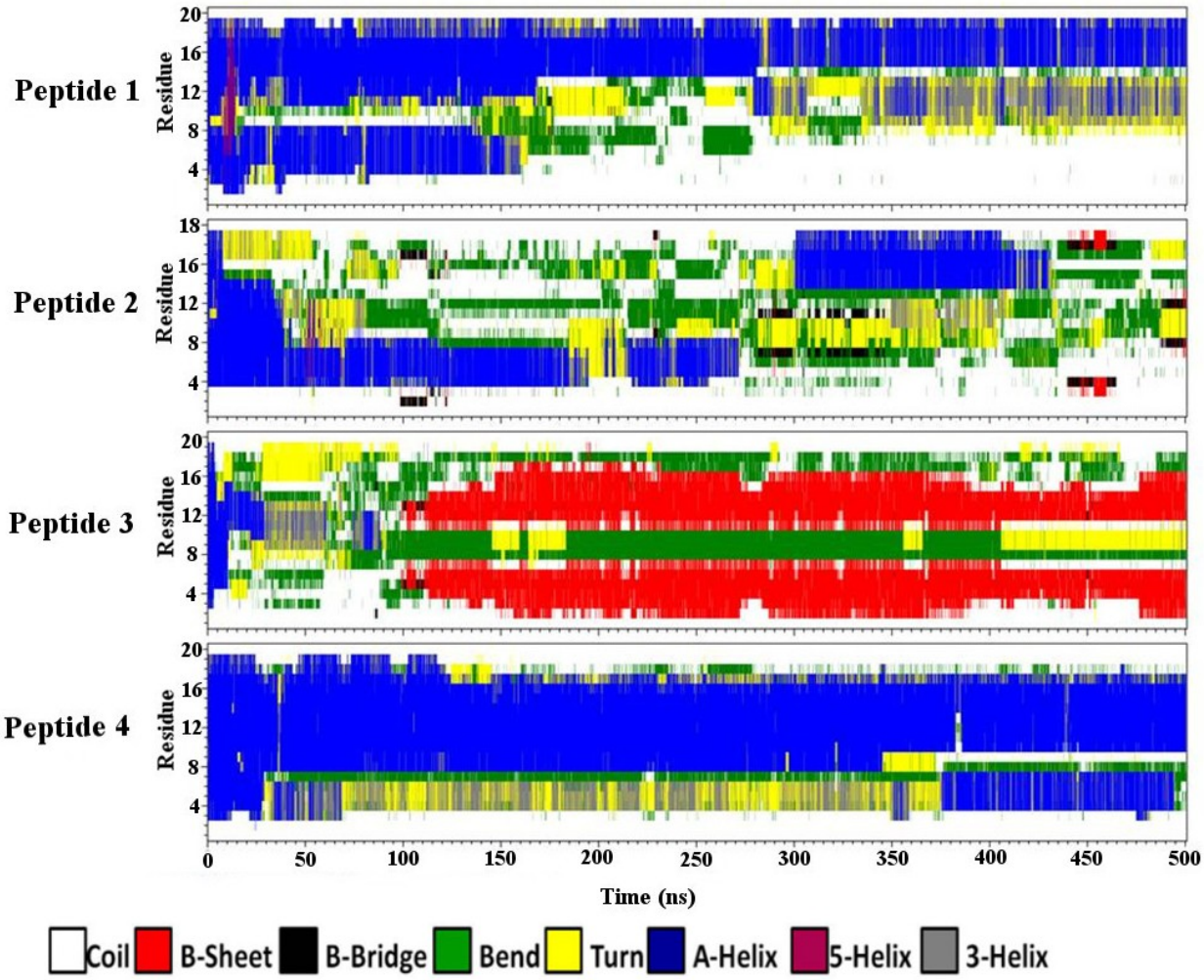

Figure S3: Secondary structure changes vs. time of 4 CA-MA peptides simulation in water at T = 300 K.

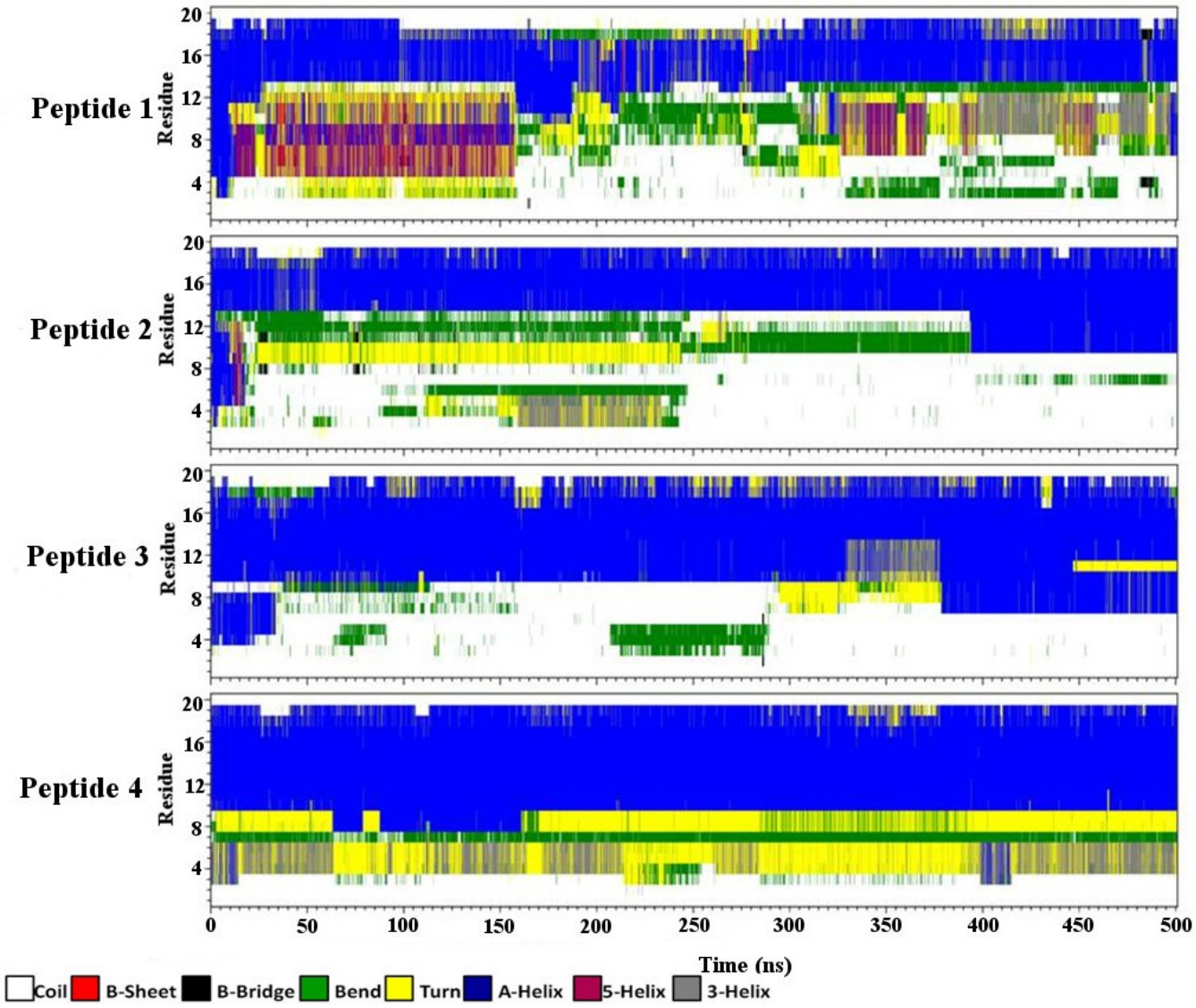

Figure S4: Secondary structure changes vs. time for 4 CA-MA in 150 mM NaCL at T = 300 K.

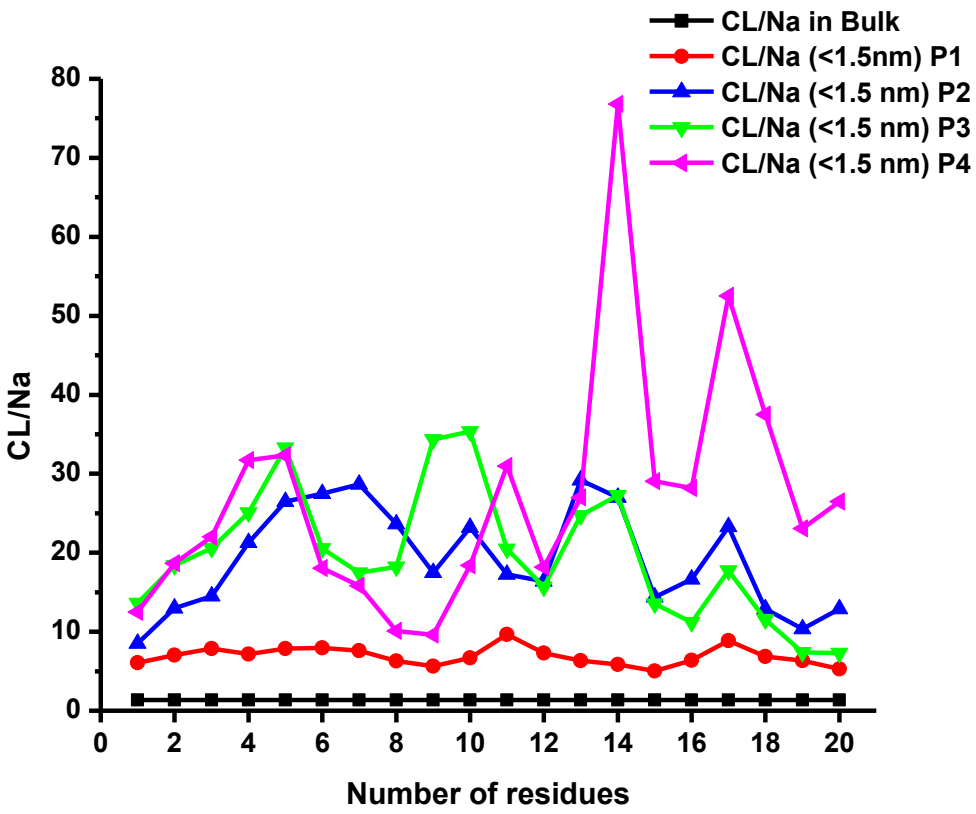

Figure S5: CL/Na values respect to Cα atoms of each residue of 4 peptides in 150 mM NaCL at T=300K, calculated within the distance of 1.5 nm from the surface of the peptide.

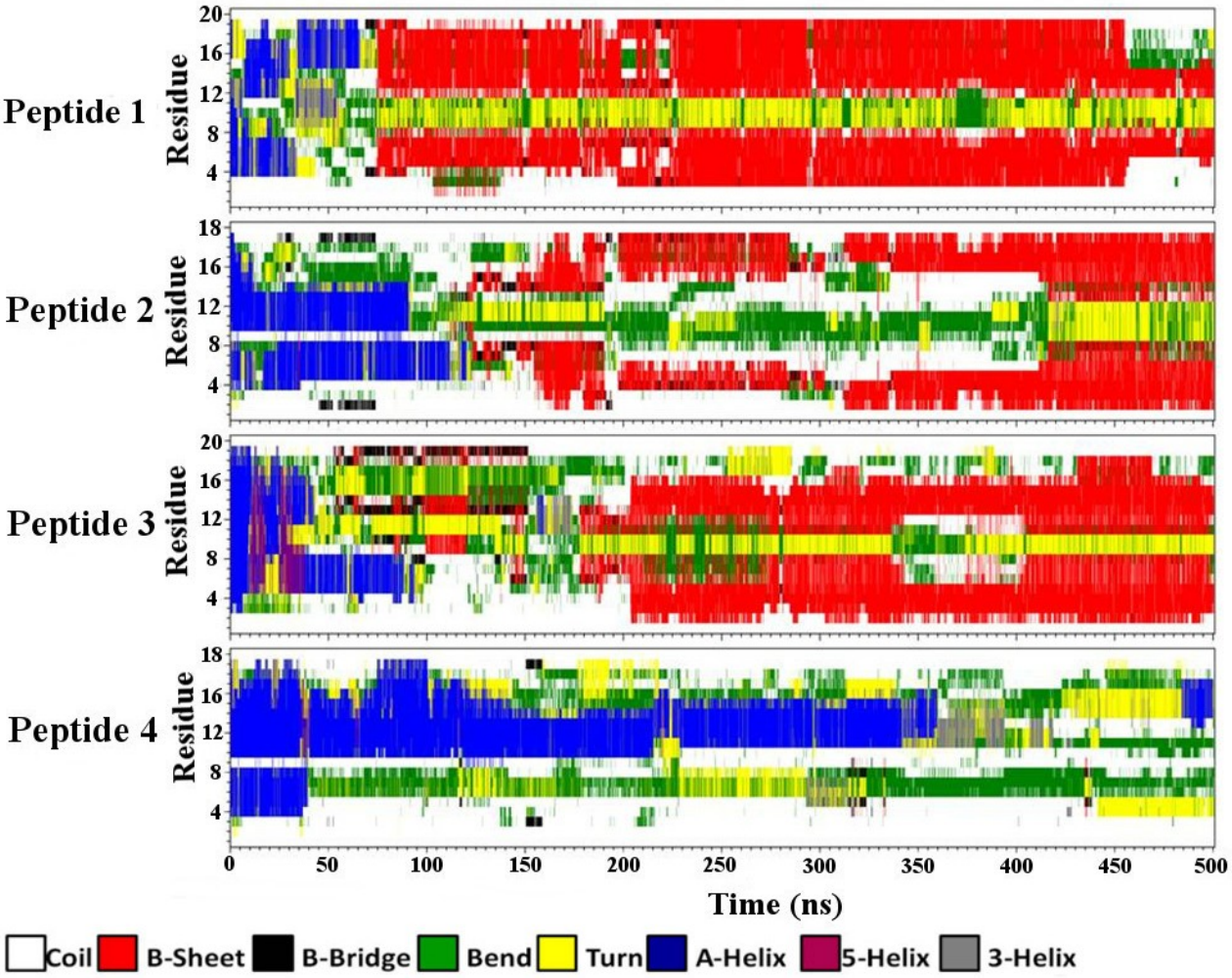

Figure S6: Secondary structure changes vs. time for 4 CA-MA in 150 mM NaCL at T=310 K.

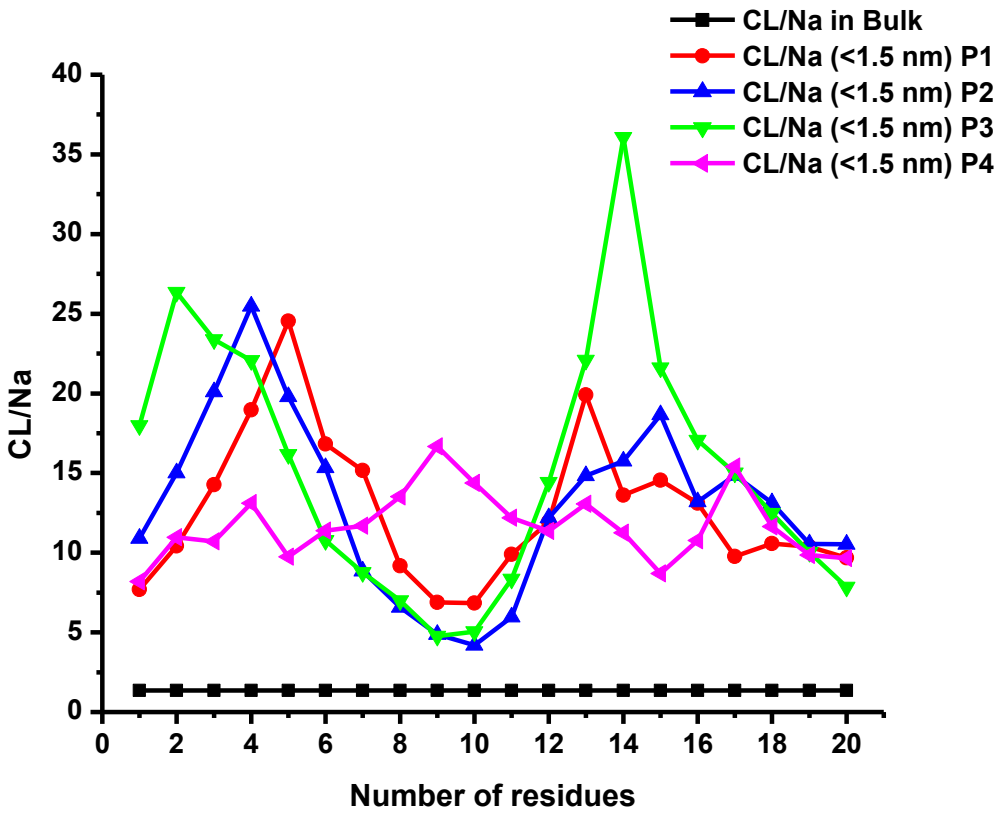

Figure S7: Cl/Na ratio values respect to each residue of 4 peptides in 150 mM NaCL at T=310K, calculated within the distance of 1.5nm from the surface of the peptide.

CHAPTER 7:

Curvature Dependant Interaction of Cecropin A – Magainin 2 (CA-MA) Hybrid Peptide with Carbon Based Nanomaterials

CHAPTER 7

CURVATURE DEPENDANT INTERACTION OF CECROPIN A-MAGAININ 2 (CA-MA) HYBRID PEPTIDE WITH CARBON BASED NANOMATERIALS

7.1 ABSTRACT

The Cecropin A – Magainin 2 (CA-MA) hybrid peptide has a significant ability to lyse bacterial cells with potential applications as antibacterial agent. It can be used for sterilization or prevention of contamination of synthetic fibers. For these applications, it is important to understand the structure of the molecule in the presence of solid surfaces capable to adsorb and, in the case of necessity, to release the peptide. Carbon based nanomaterials, such as CNT and graphene sheet, are simple models of hydrophobic surfaces. Their curvatures can be accurately controlled and CNT can act also as nanocontainer for drug delivery. Therefore, a theoretical study, using molecular dynamics simulations on the interaction of CA-MAs with these nanomaterials, has been performed. The results of the simulation have shown that the peptide is absorbed on the nanosurfaces independently by their curvature with preferential interactions of the aromatic planar amino acids (tryptophanes). Moreover, secondary structure changes, namely, the loss of α-helical content was noticed for the peptide molecules that were in contact with both, nanotube and graphene surfaces. The rate of the loss of the secondary structure are slightly faster on the graphene than on the CNT surface. Finally, the diffusion of one of the peptides inside the CNT has been observed within 150ns.

CHAPTER 7

7.2 INTRODUCTION

Carbon nanomaterials comprise materials of different shapes and surface curvatures as the hollow carbon nanotubes (CNTs) and the planar graphenes. They possess many outstanding properties, which makes them attractive for applications in various fields of science and technology. It has been shown that CNTs can act as ion channel blockers[1], artificial muscles[2], sensors,[3-4] as well as, drug-delivery vehicles.[5] However, the major obstacle to use them for medical purposes concerns their poor solubility in water. In fact, they usually form unsoluble aggregates (bundles), which can evoke cytotoxic effects in most cases.[6-10] Covalent[11-12] or non-covalent[13-15] surface modification may help to solve this problem. However, one should pay attention, that covalent modification can alter the CNT properties. Therefore, non-covalent adsorbtion of molecules is more preferential.

There is a great interest in discovering the capabilities of biomolecules, such as peptides[16] and DNA,[17] to improve CNTs solubility by covalent or non-covalent interactions, and, hence, to use them as drug delivery system. For this reason, it is crucial to understand the CNT/peptide interactions at molecular level.

Several studies, either experimental[16,18] or theoretical,[19-24] regarding to peptide-CNT interactions have been published. Wang et al.[16] have studied by scanning electron microscopy (SEM), the binding of different peptides on carbon nanotubes. They found that higher binding affinity have revealed peptides, containing aromatic residues. Tomasio and Walsh,[19] used similar peptides (named "strong binder" peptides having tryptophane rich sequences) to study their adsorption on carbon nanosurfaces using molecular dynamics (MD) simulations. In the study they replaced the tryptophane residues either with tyrosine, or phenylalanine and showed that the peptide's ability to bind the graphitic surface was reduced compared to the original one. Trzaskowski et al.[20] performed MD studies on interaction of α-helix and β- hairpin model peptides with outer and inner wall of CNTs. Two types of the nanotubes, (22,0) and (30,0), were considered in the study, both with the length of ~ 2.2 nm. The results of the studies have shown that the encapsulation in the CNT or the binding to its surface do not affect the original secondary structure of the peptide. However, when the peptide was covalently binded to the nanotube through a linker significant changes of the secondary structure were observed. Recently, Wallace and Sansom[22] reported

multiscale MD simulation studies of the adsorption of *de-novo* designed amphiphilic helical peptide (nano-1) on CNT surface. They have found that the adsorption mechanism of peptide on the CNT was the same, either for the atomistic or the coarse-grained model. They also reported that the adsorption of a single peptide on CNT surface caused the loss of its α-helical content. However, if more than one peptide is adsorbed on the CNT surface, the secondary structure remained stable. An effect of curvature on the α-helix breaking tendency of carbon based nanomaterials has been studied by Balamurugan *et al.*[23] using again MD simulations. It was shown that the tendency of helix breakage was increasing, while decreasing the curvature of the nanomaterials. Secondary structure changes have also been found by Zuo and coworkers[24] when investigating an adsorption of protein Villin headpeace (HP35) onto graphene surface.

In this chapter, we extend these theoretical studies by considering the interaction of the hybrid peptide Cecropin A – Magainin 2 (CA-MA) with carbon nanotube and graphene surfaces. CA-MA hybrid peptide is an attractive model for the investigation, because of its recognised antimicrobial and anticancer capabilities.[25-27] In Figure 7.1 is shown the structure and the aminoacid sequence of hybrid CA-MA peptide. CA-MA can be used to prevent the bacterial contamination of materials. For these applications, it is important to understand the structure of the molecule in the presence of solid surfaces. CNT and graphene nanosheet are convenient models of hydrophobic surfaces, because their geometric properties, as the curvature, can be accurately controlled. In additions, CNT can act also as nanocontainer for drug delivery.

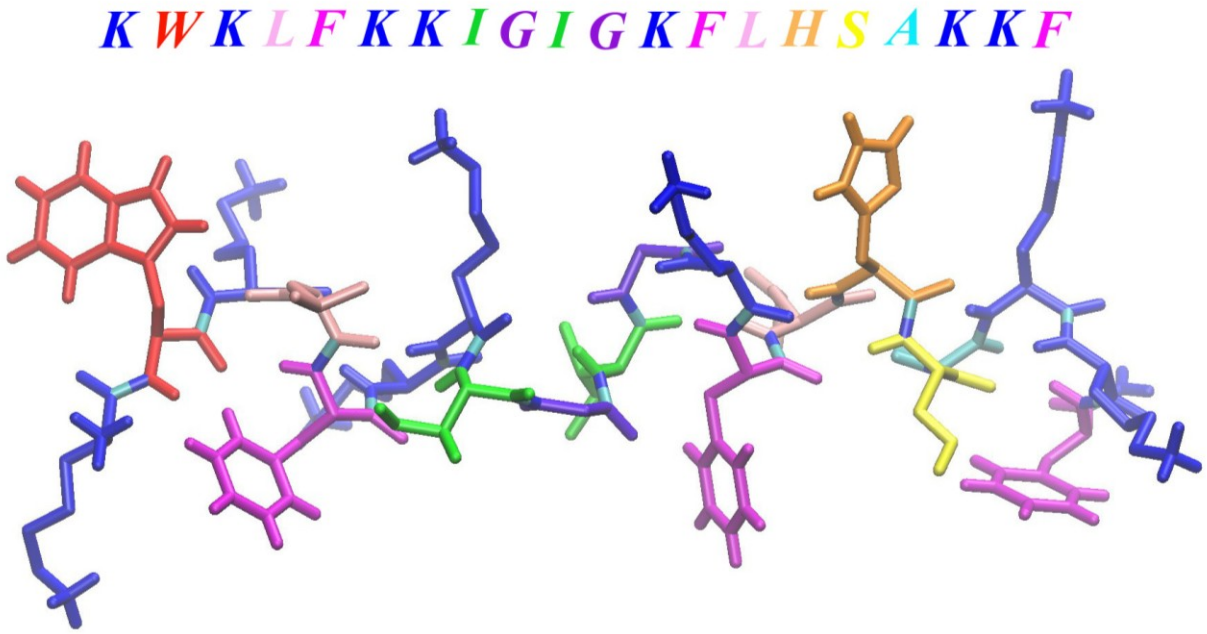

Figure 7.1: Structure of Cecropin A-Magainin 2 hybrid peptide and aminoacid sequence.

The present goal of the preliminary study is the understanding of the binding modes of CA-MA peptide to carbon based nanomaterials. In this work the model of non-covalent interaction of this peptide with the surface of these nanomaterials has been tested in order to predict the adsorption tendency and the effect on the peptide's structural and dynamical properties.

7.3 COMPUTATIONAL METHOD

7.3.1 System Setup.

The coordinates of CA-MA hybrid peptide have been obtained from the Protein Data Bank (PDB), entry code 1D9J. Carbon nanotube with the chiral indices m=10, n=10 and the length of 6 nm was generated using the VMD software version 1.9.1.[28] A graphene layer with the same chiral indices and length, as the nanotube, has been considered. The VMD software was used to build up the graphene layer, as well. Simple Point Charge (SPC/E) model of water was used in all the simulations[29] The GROMOS54a7 force field parameters were used for modeling the

atomic interactions. The Lennard-Jones parameters for carbon-carbon interaction of nanotube ε_{cc} were chosen to be 0.4396 kJmol^{-1} and σ_{cc} - 3.851 A^{0} [30] and carbon – oxygen between the carbon of the nanotube and the oxygen of water, ε_{co}= 0.392 kJmol^{-1} and σ_{co}= 0.319 nm [31]. The LJ parameters between the carbon of the nanotube and hydrogen of the naotube were set to zero, whereas the partial charges, carrying by hydrogen atoms q(H) were equal to 0.1 e, the opposite value of the charge was chosen for the carbon atoms q(C) = -0.1, in order to keep the system neutral. The rest of the parameters were calculated using the GROMOS combination rules: [32]

$$C_{ij}^{(6)}=\sqrt{C_{ii}^{(6)} * C_{jj}^{(12)}} \qquad C_{ij}^{(12)} = \sqrt{C_{ii}^{(12)} * C_{jj}^{(12)}} \qquad (7.1).$$

To study an interaction of peptides with the carbon nanomaterials and to investigate the character of interaction and the mechanism of adsorption on different surfaces, we centered four CA-MA peptides with CNT/graphene in cubic simulation boxes with the side size of at least 10 nm. The empty space was filled with water molecules by stacking an equilibrated box of 216 water molecules. The water molecules within 0.25 nm from the solute atoms were removed. 32 counter ions were added to keep the systems neutral. In Table 7.1 is given information related to simulated system.

Table 7.1: *Composition and conditions of studied systems.*

System	N^{o} of Peptides	N^{o} of Water	N^{o} of Cl^{-}	T/K	Time/ns
CNT+CA-MA	4	32242	32	300	350
Graphene+ CA-MA	4	32211	32	300	350

7.3.2 MD Simulations.

Atomistic MD simulations were performed using GROMACS (version 4.5.5) software package. The LINCS algorithm [33] has been applied in order to constraint the bonds during the simulation. The integration time step was chosen to be 2 fs. The temperature and pressure were maintained to the reference value (T=300 K, P=1 bar) using the Berendsen thermostat and barostat[34] with coupling time constant of τ_T=0.1 ps for the temperature and τ_p=0.5 ps for the pressure, respectively. The isothermal compressibility of 4.5×10^{-5} bar^{-1} was used for all the simulations. Particle mesh Ewald (PME) method [35] was applied for the long-range interactions with a real space cutoff of 1 nm, a Fourier mesh spacing of 0.12 nm. The Lennard-Jones interactions were calculated using a cutoff of 1.4 nm.

The VMD (version 1.9.1)[28] program was used to visualize the trajectories and create the graphical representation of the molecules. Secondary structure analysis has been performed by DSSP method.[36]

7.4 RESULTS AND DISCUSSIONS

7.4.1 Interaction of CA-MA with CNT

In Figure 7.2 A the starting configuration of the simulations with four CA-MA peptides with CNT (10,10) and in Figure 7.2 (B-F) different views of the configuration at 350 ns are reported. For clarity other peptides and the water molecules are omitted. From the figures it is evident, that all four peptides are adsorbed on CNT surface at the end of the simulation. In Figure 7.2 (B-D), it is shown the peptides 1, 3 and 4 adsorbed on nanotube surface. As shown in Figure 7.2 (E and F), the peptide 2 has diffused into the CNT for almost all of its length.

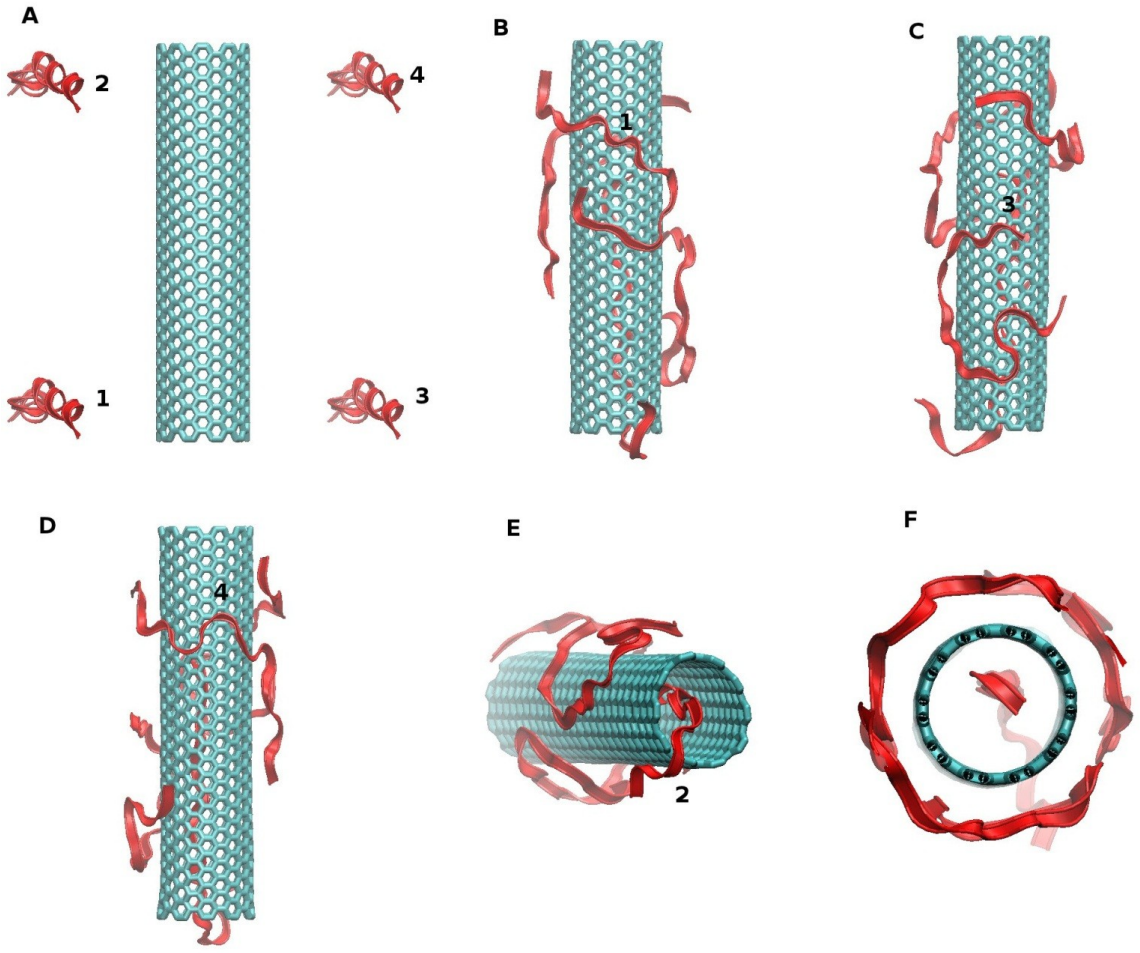

Figure 7.2: Four CA-MAinteractions with CNT (10, 10) (water molecules are ommited for clarity). A-starting configuration, B, C, D, E-configuration after 350 ns (side view), F – (top view).

The process of absorption of the four peptides has been monitored calculating the minimum distances between the C-alpha atoms of the peptides and the carbon asoms of the CNT along the simulation. In Figure 7.3 the variation of these distances are reported. For the peptide 3 and 4, a rapid adsorption (distances less than 0.5 nm) occurs after few nanoseconds. After 20 ns, peptide 1 binds to the CNT and ~250 ns are required for the peptide 2 to get in contact with one of the nanotube entrance and to start diffusion inside.

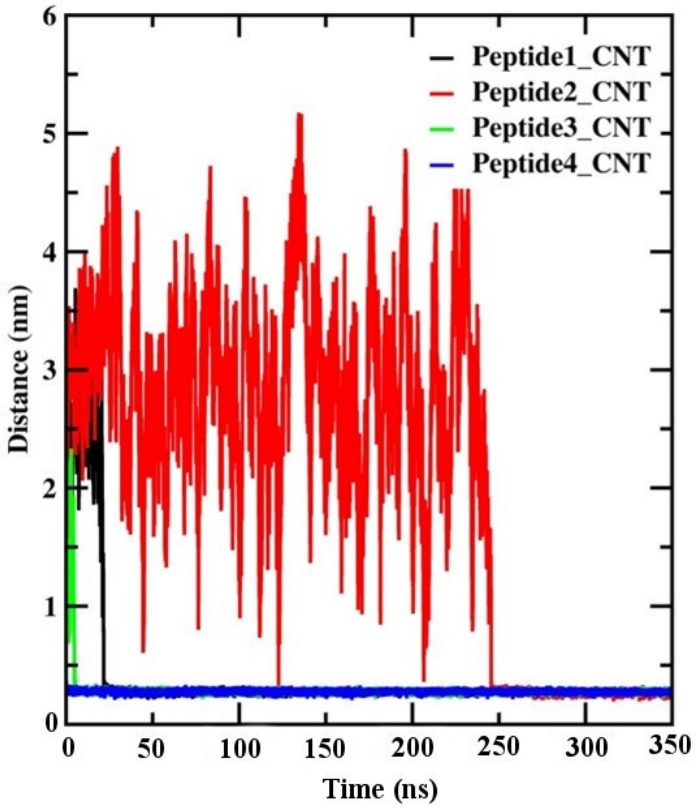

Figure 7.3: Minimum distance between the C-alpha atoms in each peptide and the CNT surface.

The distances between C-α atoms of each aminoacid, which are present in CA-MA peptide, and the nanotube has been calculated for the last 10 ns in order to characterize the preferential bindings of the aminoacids to the surface of the CNT. Based on the distances between the aminoacids (C-α atoms) and the nanotube, the relatively closest distances are, mainly, for C-α atoms corresponding to tryptophanes (see Figure 7.4 red coloumn bars), phenylalanins (Figure 7.4 magenta color bars), lysins in some cases (Figure 7.4 blue bars), glycines for the case of peptide 2 (Figure 7.4 violet bars). The possible explanation can be the presence of aromatic group in tryptophane, phenylalanine that reveals higher affinity to the surface of the CNT compared to the other aminoacids, because of its surface characteristics. The average distance between the surface of the nanotube and C-α atoms for all the peptides is ~ 0.44 ± 0.04 nm.

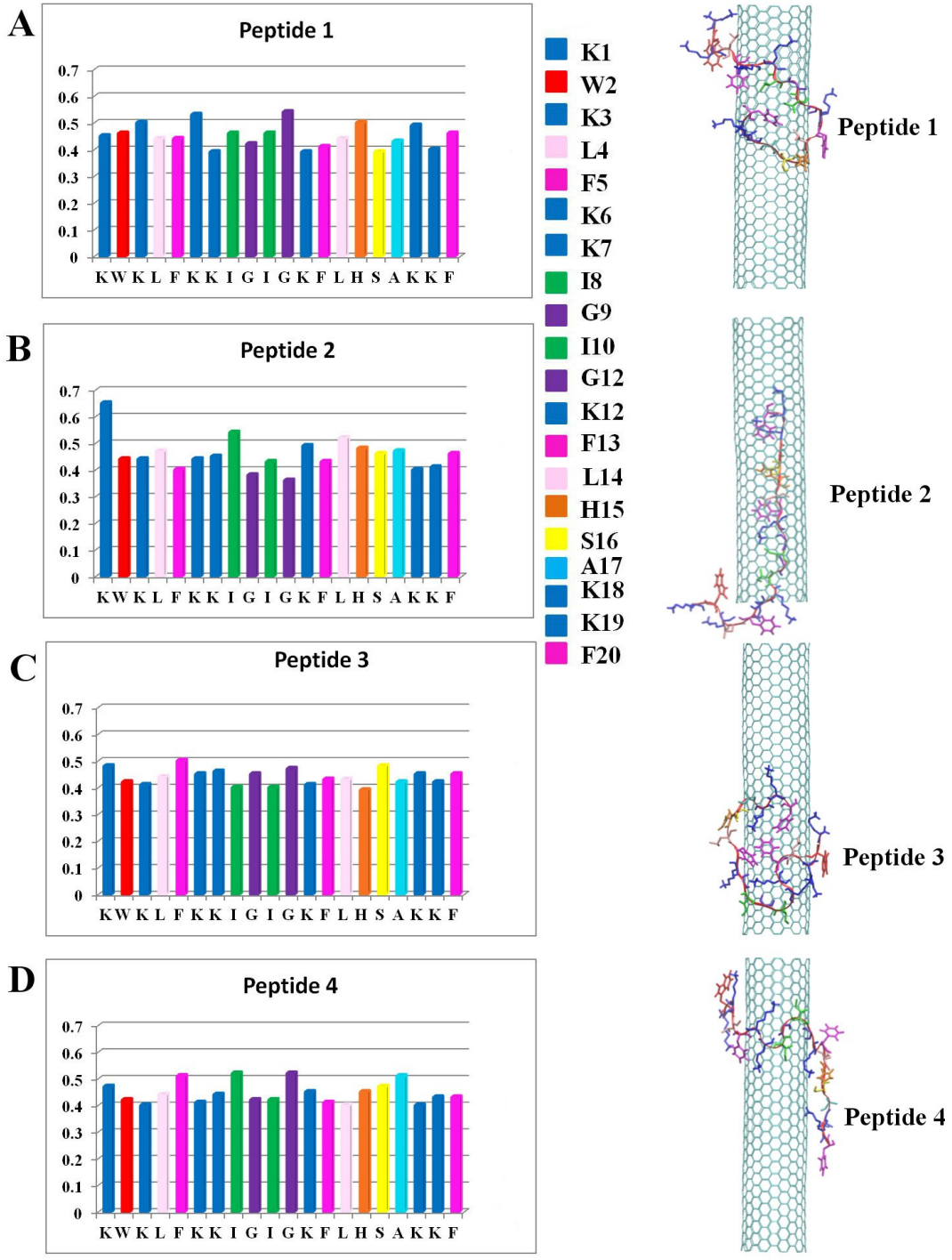

Figure 7.4: At the left side the distances between the C-α atoms of each amino acid and the surface of the CNT are reported. At the right side the peptides 1, 2, 3 and 4 adsorbed on CNT surface are shown.

7.4.2 Diffusion of the Peptide Inside the CNT

In Figure 7.5 the different stages of the diffusion process are reported. The entry in the CNT rim occurs starting from the C-terminal of the peptide at ~265 ns and it proceeds till the 315 ns of the simulation. After this time, the N-terminal of the peptide remain anchored to the outer surface of the nanotube stopping further diffusion into the CNT for the rest of the simulation. Therefore, at the end of the simulation (Figure 7.2 E and F), the peptide has diffused inside for ¾ (~4.5 nm) of the CNT length (6 nm) with an average speed of ~0.09 nm/ns.

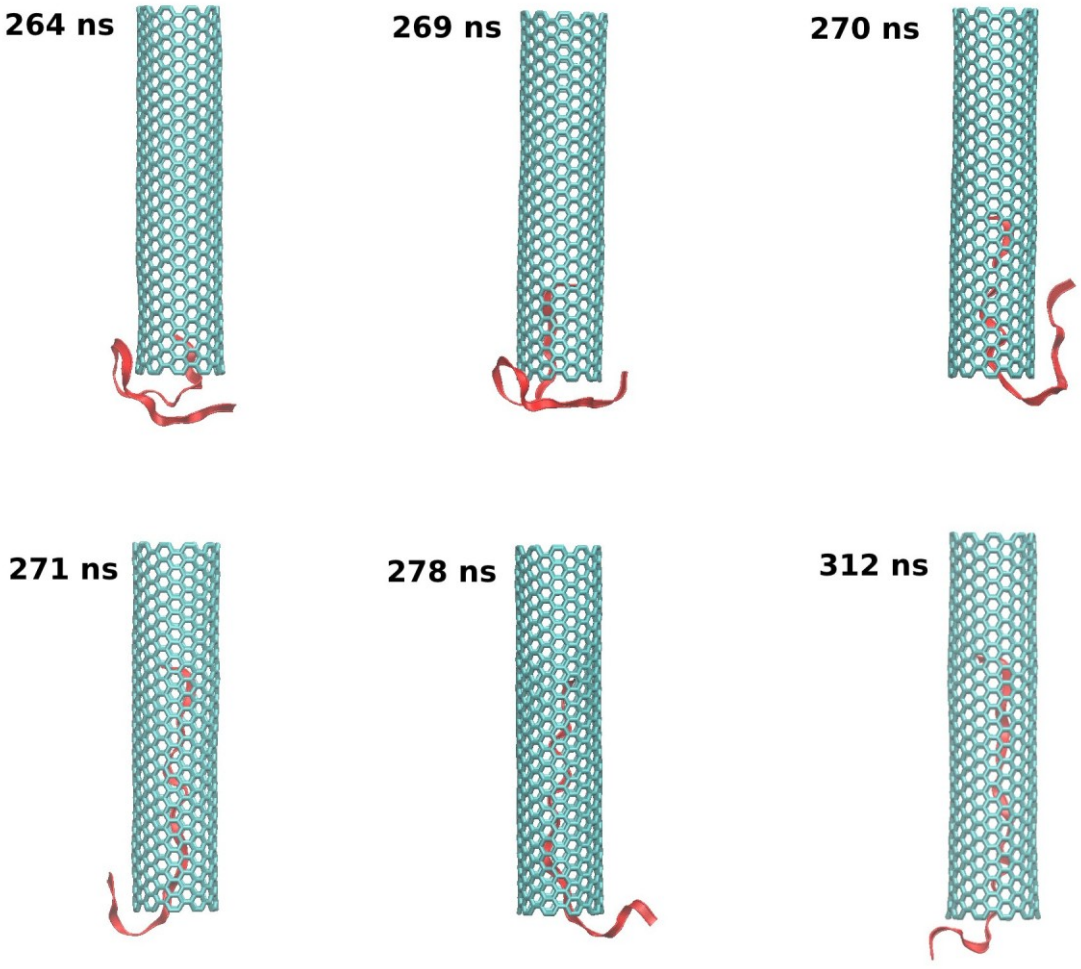

Figure 7.5: Diffusion process in time for the peptide 2 inside the CNT core.

The effect of the presence of hydrogens on the rim of CNT has been studied by running a new simulation with the peptide in the configuration shown in Figure 7.5 at 264 ns, where the peptide is pulled out and placed in front of the same CNT, but with fully protonated carbon rim atoms. In Figure 7.6 the snapshots of the configuration at 0, 0.3, 1, 5 and 100 ns –A, B, C, D, E, respectively, are reported. The first contact of the peptide with the surface of the nanotube occurs just at 0.3 ns and after 5 ns the peptide is totally extended it and remains in such conformation until the end of the simulation. Contrary with the previous case (see Figure 7.5), the peptide does not diffuse inside the nanotube, but adsorbes on its surface. Although the result of simulation suggest that electrostatic repulsion between the hydrogens of CNT and the positively charged peptide prevent the peptide to enter the nanotube, more simulations are required to be performed in order to obtain statistical significance of this phenomenon.

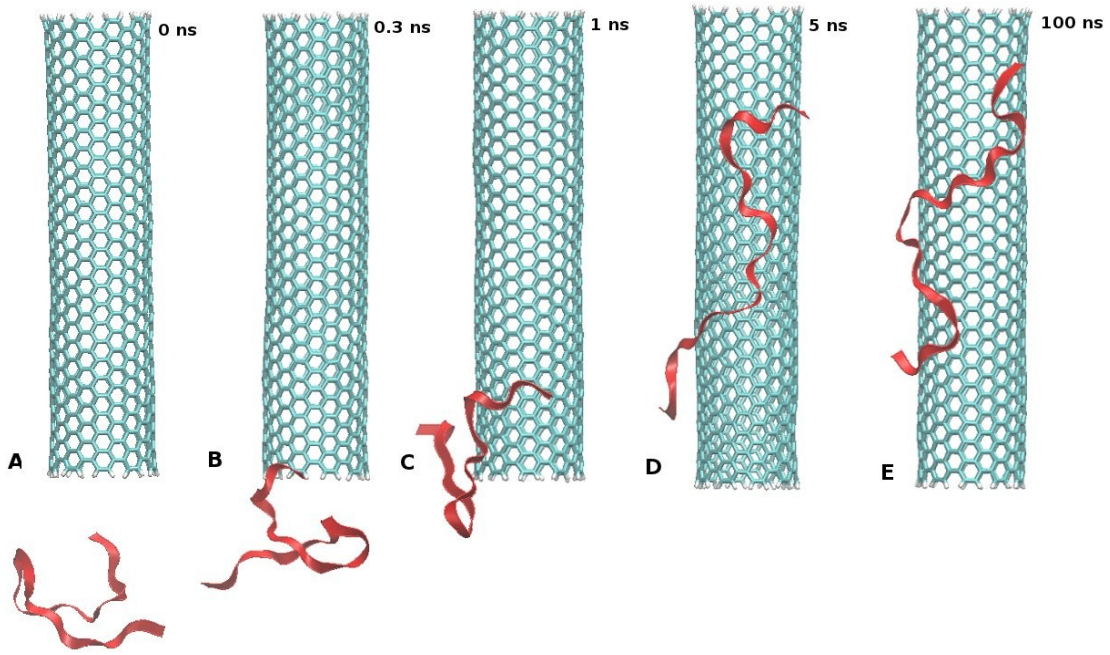

Figure 7.6: Interaction of the peptide with the hydrogenated nanotube. A - initial configuration (0 ns), B, C, D and E are configurations at 0.3, 1, 5 and 100 ns, respectively.

7.4.3 Secondary Structure.

The analysis of the changes in the peptide secondary structure (SS) along the simulation has been performed in order to understand how the interaction with the CNT surface affect the initial peptide fold. Figure 7.7 reports secondary structure changes during the simulation for each amino acids of the four CA-MA peptides.

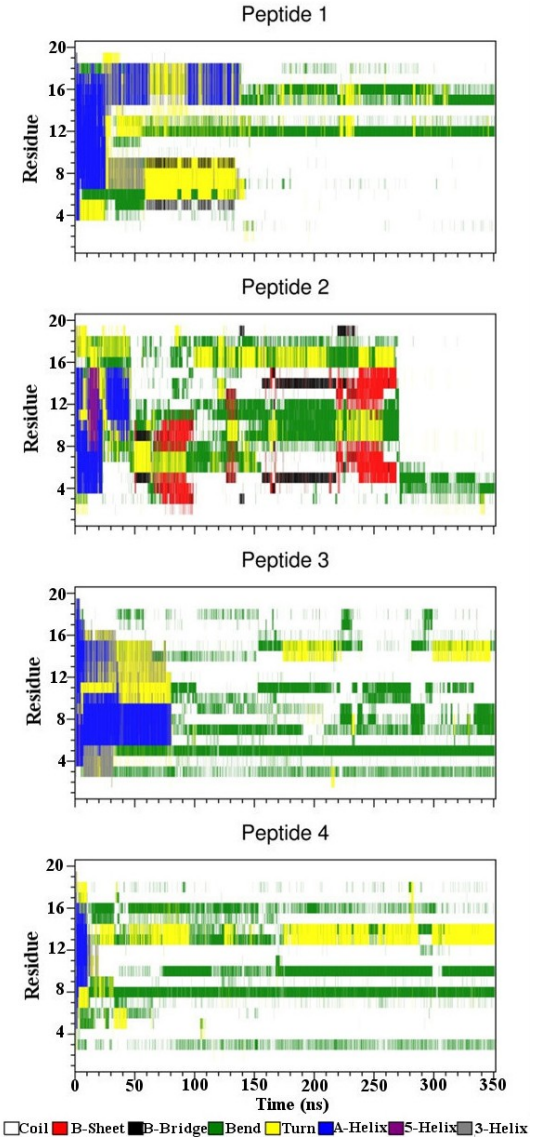

Figure 7.7: Secondary structure changes during the time for 4 CA-MA peptides while interacting with CNT.

The decrease of the intial a-helical content occurs already at the beginning of simulation for all the peptides. After 150 ns, a complete loss of the α-helical content is observed. In particular, for the peptide 1 significant decrease of α-helical structure suddenly occurs around 20 ns, the remained a-helix fragment in the N-terminal part of the peptide unfolds completely after 140 ns. For the peptide 2, similarly to the peptide 1, the decrease of α-helix structure takes place after 20 ns with the complete loss of the helical content after just 40 ns. After this time, β-strands and β-bridges form temporary in different parts of the peptide chain until the entrance into the CNT at ~240 ns. At the end of the simulation, when the peptide is into the CNT, only an extended random coil conformation is observed. For the peptide 3, the unfold of the initial α-helix structure occurs within 70 ns with a different pattern with respect the other peptides. It can be noted that the peptide 4 come in contact with the nanotube from almost the beginning of the simulation. This is the reason of the immediate and irreversible loss of the α-helix structure.

Figure 7.8 shows the average SS for four CA-MA peptides in percentage calculated for the last 100 ns. Random coil conformation represents more than 70% of the secondary structure (see Fig. 7.8 blue bars). The rest of SS is present in the form of turn and bend regions. In general, all the peptides suffer a loss of the initial a-helix content upon the contact with the CNT apolar surface with formation of highly unfolded structure.

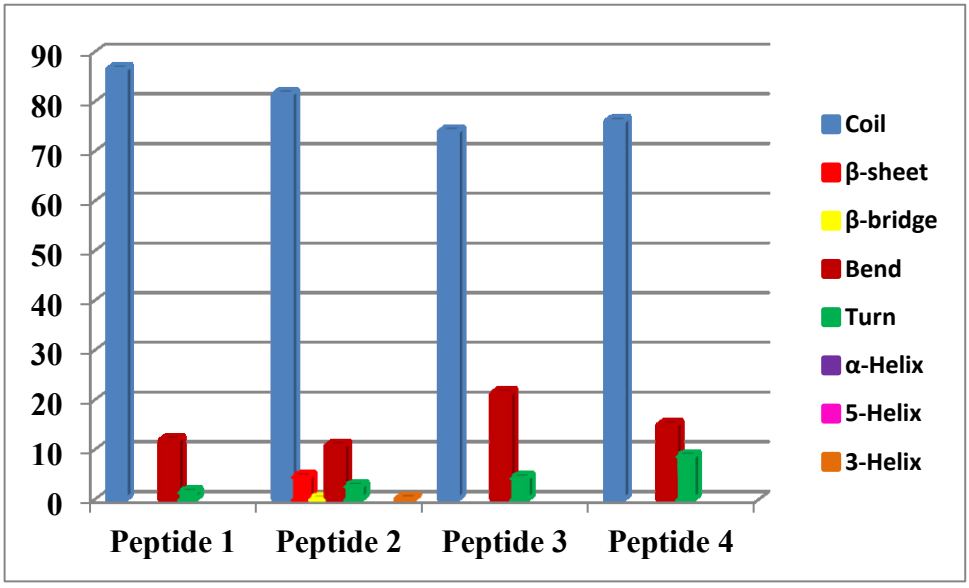

Figure 7.8: Average secondary structure for each peptide, interacting with CNT (10,10), shown in percentage.

7.4.4 Interactions of CA-MA Peptides with Graphene Nanosheet.

Effect of the surface curvature on structural stability of peptide has been investigated by analyzing the bindings of four CA-MA peptides on the top of a graphene layer. Figure 7.9 represents snapshots from the simulations of the CA-MA peptides with graphene. Figure 7.9 A represent the initial configuration and B and C the side and top views of the configuration at 350 ns, respectively. The peptides are adsorbed on both sides of the graphene nanosheet with three of them on one side and the other in the opposite side.

Figure 7.10 reports the minimum distances between the C-α atoms of each peptide and the surface of the graphene. Adsorption of the peptides 1, 2 and 4 on one side of the graphene surface occurs in the first 10 ns of simulation. After 50 ns of simulation also peptide 3 binds on the other side of the graphene nanosheet. This delay is due to the time to diffuse on the free side.

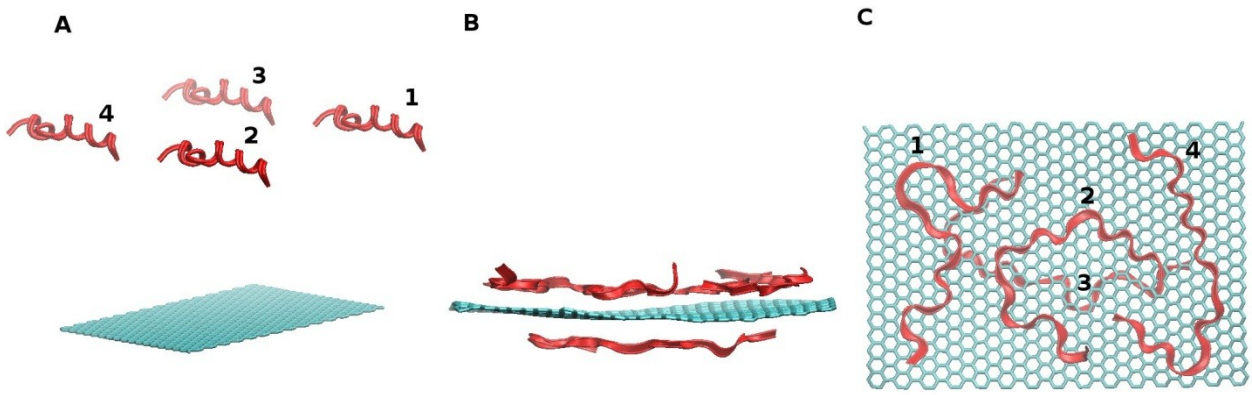

Figure 7.9: Four CA-MAinteractions with graphene layer. A – initial configuration, B and C – configurations at 350 ns (side and top views respectively). For clarity water molecules are ommited and the peptides are labeled as 1, 2, 3 and 4.

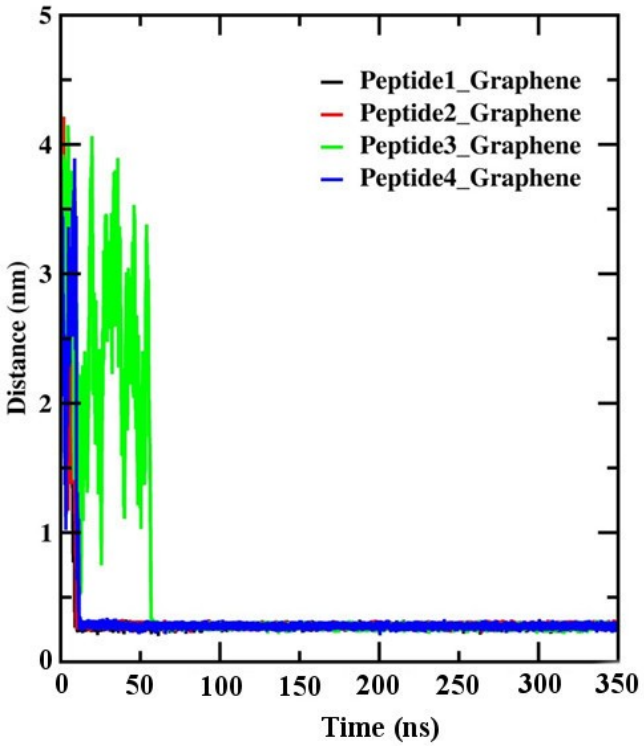

Figure 7.10: Minimum distance between the C-αatoms of each peptide respect and the graphene.

In Figure 7.11, the averaged minimum distances between the C-α atoms of each aminoacid and the graphene surface are reported. All the peptides show similar avarage distances ~ 0.44 ± 0.03 for C-α atoms from the surface of graphene indicating a flattering of the peptide on a graphene surface (see Figure 7.11, the right side). Similarly to the case of interactions with the surface of CNT (see Figure 7.4, the right side), in this case the peptides also obtain certain conformation while interacting with the surface of graphene. Since CA-MA peptide contains aromatic amino acids like tryptophanes, phenylalanines and histidines in its sequence, the preferential contacts are between these groups and the CNT/graphene surface due to the planar geometry of these residues. In order to provide the possibility of interaction between these groups and the carbon nanosurfaces, the peptide should unfold from its initial α-helical configuration and obtain specific conformation on the nanosurface.

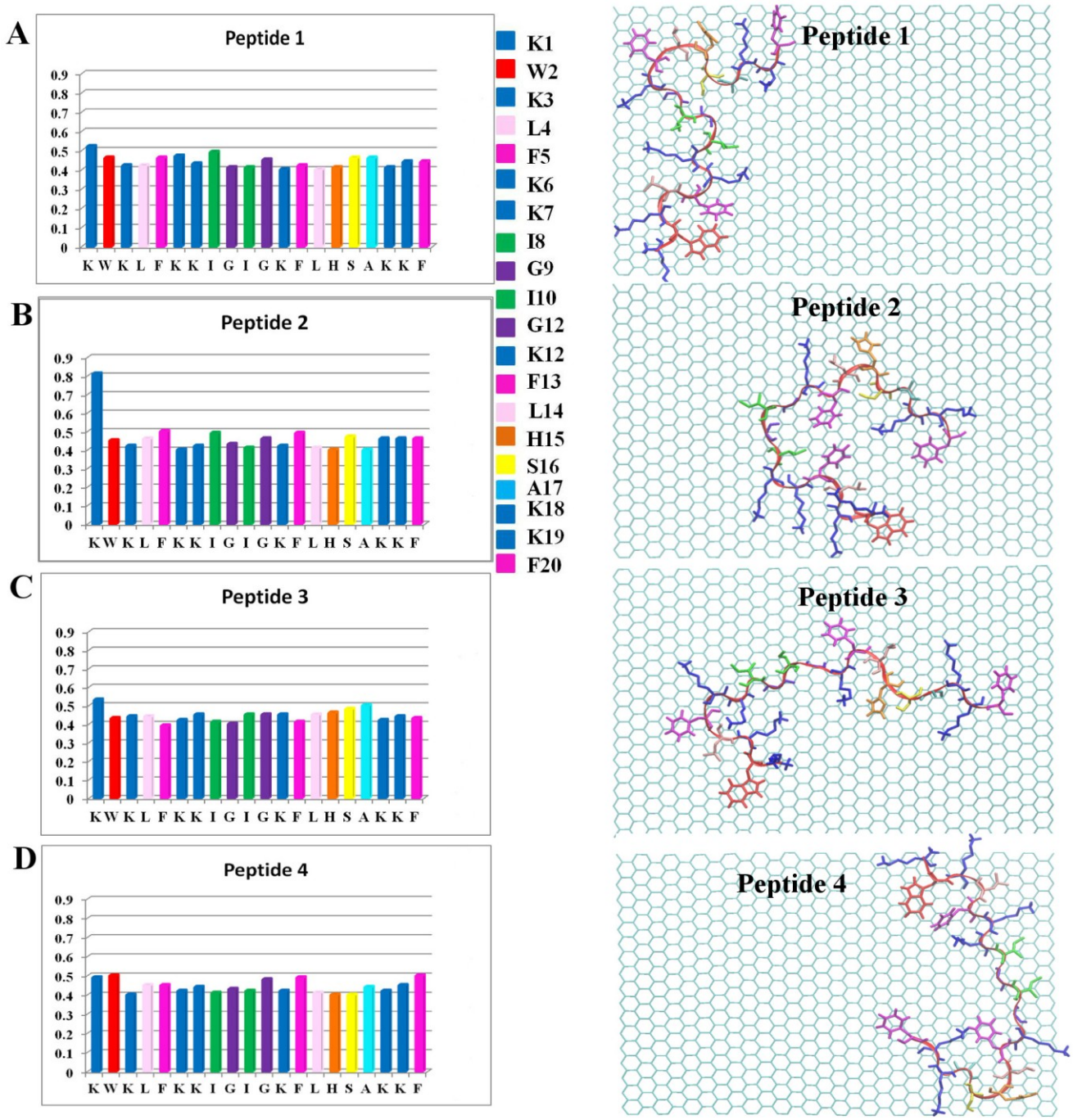

Figure 7.11: At the left side the distances between the C-α atoms of each amino acid and the surface of the graphene are reported. At the right side the peptides 1, 2, 3 and 4 adsorbed on the surface of graphene nanosheet are shown.

7.4.5 Secondary Structure.

Figure 7.12 shows the results of the secondary structure changes of four CA-MA peptides vs time for the interaction with the flat surface of the graphene. Significant decrease of α-helix structure takes place for CA-MA peptides (except peptide 3) as the peptide start to bind the nanosheet. Complete loss of the α-helical content occurs within 70, 10, 60 and 40 ns for the peptides 1, 2, 3 and 4, respectively. Later, the peptides are mostly present in random coil, turn and bend conformations similarly to the case of simulations of peptides with the nanotube. In the case of peptide interaction with the planar graphene surface the rate of the loss of secondary structure is slightly faster compared to the interaction with the curved nanotube surface.

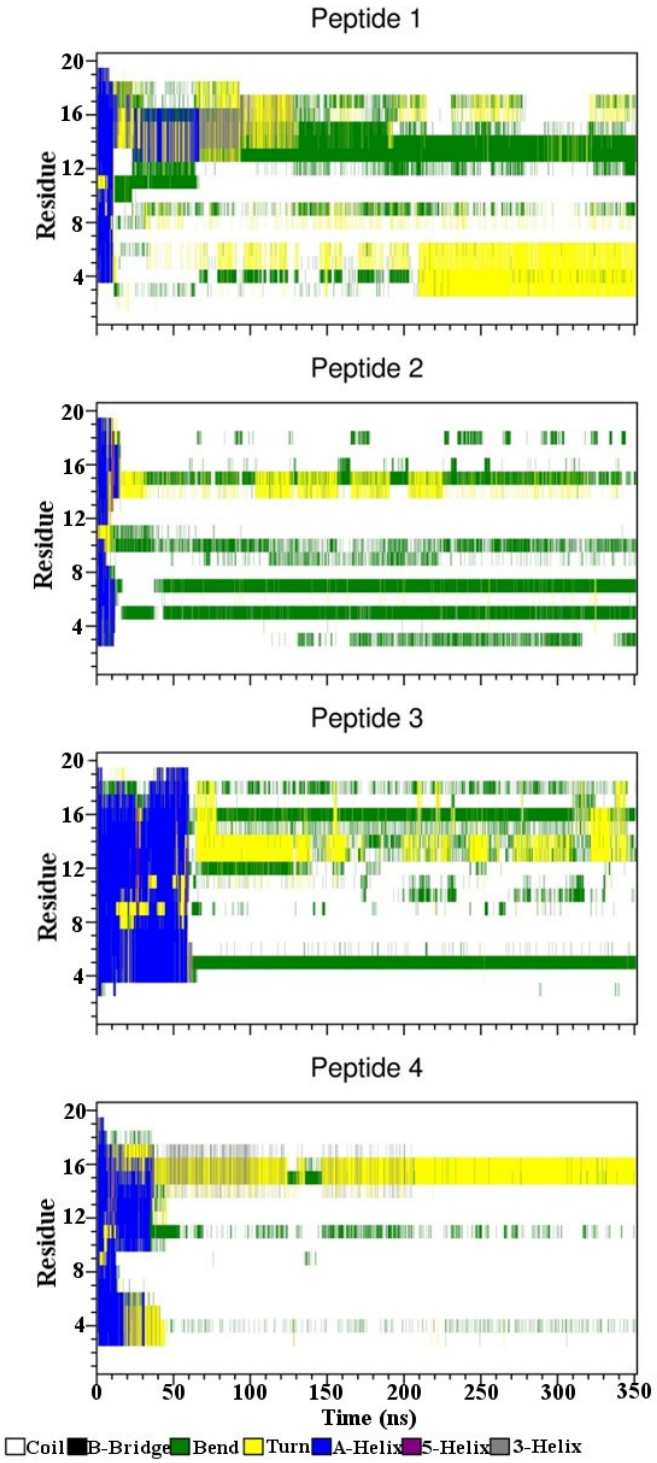

Figure 7.12: Secondary structure changes during the time for 4 CA-MA peptides, interacting with graphene.

Figure 7.13 shows the average secondary structure amount in percentage for the peptides' simulation with graphene for the last 100 ns. As in the case of simulations of peptides with CNT, the most abundant conformations are random coil and less than 20 % of the structure are present as bend and turn SS.

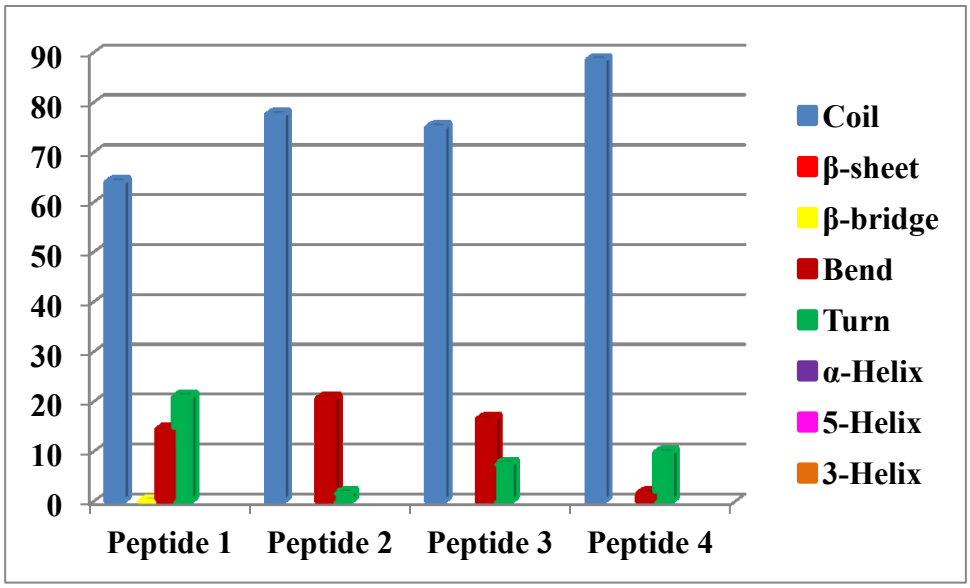

Figure 7.13: Secondary structure of each peptide, interacting with graphene, shown in percentage.

CHAPTER 7

7.5 CONCLUSIONS

MD simulations have been performed to study the mechanism of interaction of hybrid antimicrobial peptide – CA-MA with the CNT (10,10) and the graphene nanosheet of the same linear size. The MD results of the study have shown that the peptides coat both the CNT and graphene surfaces with different kinetic. The peptides coating the carbon nanosurfaces loose completely their secondary structure compared to the simulations in absence of nanomaterials (see Chapter 6). The preferential binding, estimated by the minimum distance of the peptide from the CNT surface atoms, suggest that aromatic amino acids like tryptoptophanes, phenylalanines and histidines, bind closely to the surface due to the favorable LJ interactions of the flat surface of the aromatic side chains. This result is in agreement with the one obtained by Wang et al.[16], where it was found, that specifically binding peptides to the nanotube surface were rich with aromatic residues, such are histidine and tryptophane, at their binding sites.

Spontaneous diffusion of one of the peptides inside the not hydrogenated CNT has been obseved. To the best of our knowledge this is the first simulation in which this phenomenon is observed for such a small nanotube. However, more simulation are requiered to be performed in this direction for higher statistical importance. This process can be also interesting to further investigate for the possibility to use CNT as a drug delivery system.

7.6 REFERENCES

(1) Baughman, R. H.; Zakhidov, A. A.; de Heer, W. A. *Science* **2002**, *297*, 787.
(2) Baughman, R. H.; Cui, C.; Zakhidov, A. A.; Iqbal, Z.; Barisci, J. N.; Spinks, G. M.; Wallace, G. G.; Mazzoldi, A.; De Rossi, D.; Rinzler, A. G. *Science* **1999**, *284*, 1340.
(3) Liu, X.; Shi, L.; Niu, W.; Li, H.; Xu, G. *Biosensors and Bioelectronics* **2008**, *23*, 1887.
(4) Allen, B. L.; Kichambare, P. D.; Star, A. *Advanced Materials* **2007**, *19*, 1439.
(5) Dhar, S.; Liu, Z.; Thomale, J. r.; Dai, H.; Lippard, S. J. *Journal of the American Chemical Society* **2008**, *130*, 11467.
(6) Colvin, V. L. *Nature biotechnology* **2003**, *21*, 1166.
(7) Magrez, A.; Kasas, S.; Salicio, V.; Pasquier, N.; Seo, J. W.; Celio, M.; Catsicas, S.; Schwaller, B.; Forró, L. *Nano letters* **2006**, *6*, 1121.
(8) Lam, C.-W.; James, J. T.; McCluskey, R.; Hunter, R. L. *Toxicological Sciences* **2004**, *77*, 126.
(9) Monteiro-Riviere, N. A.; Nemanich, R. J.; Inman, A. O.; Wang, Y. Y.; Riviere, J. E. *Toxicology letters* **2005**, *155*, 377.
(10) Cui, D.; Tian, F.; Ozkan, C. S.; Wang, M.; Gao, H. *Toxicology letters* **2005**, *155*, 73.
(11) Riggs, J. E.; Guo, Z.; Carroll, D. L.; Sun, Y.-P. *Journal of the American Chemical Society* **2000**, *122*, 5879.
(12) Huang, W.; Fernando, S.; Allard, L. F.; Sun, Y.-P. *Nano letters* **2003**, *3*, 565.
(13) Min, K.; Kim, J.; Park, K.; Yoo, Y. J. *Journal of Molecular Catalysis B: Enzymatic* **2012**, *83*, 87.
(14) Lee, J. U.; Huh, J.; Kim, K. H.; Park, C.; Jo, W. H. *Carbon* **2007**, *45*, 1051.
(15) Granite, M.; Radulescu, A.; Pyckhout-Hintzen, W.; Cohen, Y. *Langmuir* **2011**, *27*, 751.
(16) Wang, S.; Humphreys, E. S.; Chung, S.-Y.; Delduco, D. F.; Lustig, S. R.; Wang, H.; Parker, K. N.; Rizzo, N. W.; Subramoney, S.; Chiang, Y.-M. *Nature materials* **2003**, *2*, 196.
(17) Johnson, R. R.; Johnson, A. C.; Klein, M. L. *Nano letters* **2008**, *8*, 69.
(18) Zorbas, V.; Ortiz-Acevedo, A.; Dalton, A. B.; Yoshida, M. M.; Dieckmann, G. R.; Draper, R. K.; Baughman, R. H.; Jose-Yacaman, M.; Musselman, I. H. *Journal of the American Chemical Society* **2004**, *126*, 7222.
(19) Tomásio, S. M.; Walsh, T. R. *The Journal of Physical Chemistry C* **2009**, *113*, 8778.
(20) Trzaskowski, B.; Jalbout, A. F.; Adamowicz, L. *Chemical Physics Letters* **2006**, *430*, 97.
(21) Chiu, C.-c.; Dieckmann, G. R.; Nielsen, S. O. *The Journal of Physical Chemistry B* **2008**, *112*, 16326.
(22) Wallace, E. J.; D'Rozario, R. S.; Sanchez, B. M.; Sansom, M. S. *Nanoscale* **2010**, *2*, 967.
(23) Balamurugan, K.; Singam, E. A.; Subramanian, V. *The Journal of Physical Chemistry C* **2011**, *115*, 8886.
(24) Zuo, G.; Zhou, X.; Huang, Q.; Fang, H.; Zhou, R. *The Journal of Physical Chemistry C* **2011**, *115*, 23323.
(25) Shin, S. Y.; Kang, J. H.; Lee, M. K.; Kim, S. Y.; Kim, Y. M.; Hahm, K. S. *Biochem. Mol. Biol. Int.* **1998**, *44*, 1119.
(26) Oh, D.; Shin, S. Y.; Lee, S.; Kang, J. H.; Kim, S. D.; Ryu, P. D.; Hahm, K.-S.; Kim, Y. *Biochemistry* **2000**, *39*, 11855.
(27) Bechinger, B. *Biochimica et Biophysica Acta (BBA) - Biomembranes* **1999**, *1462*, 157.
(28) Humphrey, W.; Dalke, A.; Schulten, K. *Journal of Molecular Graphics* **1996**, *14*, 33.
(29) Berendsen, H. J. C.; Grigera, J. R.; Straatsma, T. P. *Journal of Physical Chemistry* **1987**, *91*, 6269.
(30) Walther, J. H.; Jaffe, R.; Halicioglu, T.; Koumoutsakos, P. *The Journal of Physical Chemistry B* **2001**, *105*, 9980.

(31) Werder, T.; Walther, J. H.; Jaffe, R.; Halicioglu, T.; Koumoutsakos, P. *The Journal of Physical Chemistry B* **2003**, *107*, 1345.
(32) van der Spoel, D.; Lindahl, E.; Hess, B.; Kutzner, C.; van Buuren, A. R.; Apol, E.; Meulenhoff, P. J.; Tieleman, D. P.; Sijbers, A. L. T. M.; Feenstra, K. A.; van Drunen, R.; Berendsen, H. J. C. *Gromacs User Manual version 4.0*, **2005**.
(33) Hess, B.; Bekker, H.; Berendsen, H. J. C.; Fraaije, J. G. E. M. *Journal of Computational Chemistry* **1997**, *18*, 1463.
(34) Berendsen, H. J. C.; Postma, J. P. M.; Vangunsteren, W. F.; Dinola, A.; Haak, J. R. *Journal of Chemical Physics* **1984**, *81*, 3684.
(35) Darden, T.; York, D.; Pedersen, L. *Journal of Chemical Physics* **1993**, *98*, 10089.
(36) Kabsch, W.; Sander, C. *Biopolymers* **1983**, *22*, 2577.

CHAPTER 8:

SUMMARY AND OUTLOOK

CHAPTER 8

In this thesis, I have studied the interaction of CNTs with polymers, phospholipid bilayer and with the hybrid Cecropin A – Magainin 2 peptide at different levels of scale using MD simulations.

In the first part of the thesis, atomistic MD simulations (AMD) have been carried out to investigate the mechanism of CNT coating by linear ether-based polymeric surfactants. This study was motivated by the interest to use polymeric material to disperse CNT and coat their surface with biocompatible materials. In particular, we have studied the physical absorption mechanisms around the SWCNT by DME and DMP molecules, PEO and PPO pentamers, as well as, the Pluronics® L64 triblock copolymer. The same study has been further extended at coarse-grained level of scale for longer polymer chains. In particular, adsorptions of Pluronics® F108 and F127 chains onto the surface of the bundles were carried out using the MD-SCF method. The results from the simulations are in qualitative agreement with the available experimental data. It was shown that the interactions between the triblock copolymer chains and the surface of the single nanotube and bundles are driven by the different hydrophobic nature of the polymer blocks. Namely, the more hydrophobic PPO polymer (or block) tend to coat the apolar surface of the nanotube, whereas, the more hydrophilic PEO polymers and block interact more weakly. In the CG simulations, the numbers of aggregated F127 and F108 chains on the surface of the bundle are found to be in a good accordance with experimental data.

CNTs have shown an ability to cross biological membranes. This opens new opportunities to use them for targeted drug delivery. For this reason, it is crucial to understand the mechanism of CNT translocation through lipid bilayers, which will simplify their biomedical applications and further manipulations. Experimental researchers have proposed several pathways of CNT internalizations. The possible pathways of internalization, according to experimental data, are phagocytosis or endocytosis and spontaneous diffusion through the membrane. However, this peculiar concept is still under investigation. In order to understand these principles, first, it would be efficient to explore the interactions of CNTs with pure lipid bilayer. Detailed study of the bundle insertion inside the DPPC lipid bilayer has been performed by hybrid MD-SCF technique. In particular, the impact of the orientation and the aspect ratio on the perturbation of

lipid bilayer has been investigated. The results have shown the distortion of the bilayer in all studied cases. However, the stronger perturbations of the lipids have place in the case of perpendicularly oriented bundles. In addition, poration of the bilayer and diffusion of the water molecules through the pore has been observed during the internalization of perpendicularly oriented bundle of 20 nm.

As further work in this direction, it would be interesting also to study how the CNT bundles coated by the Pluronics interact with the membrane. One can explore whether such a complex like CNT+Pluronics is stable, while interacting with lipid membrane or not. Since pure lipid bilayer is an idealized model of cellular membrane, further studies would be efficient to be applied to interactions of CNT bundles with membranes, considering the presence of components like transmembrane proteins, glycoproteins as well as channel proteins.

Finally, the last part of my thesis is dedicated to atomistic MD simulation studies of the hybrid antimicrobial CA-MA peptide. This particular peptide has shown an ability to lyse bacterial cells and act as anticancer drug as well. For this purpose the MD simulation studies have been carried out for the single and four CA-MA peptides under different physiological conditions. In particular, the effects of ionic strength, temperature and concentration have been investigated. The results of the study have shown that the peptide loses its initial α-helix structure in solution, which is in a good agreement with experimental results. In the presence of higher salt concentration, the peptide partially maintains its α-helix structure. However, as the temperature increase to 37 ^{o}C (physiological human body temperature), the complete loss of α-helical content has been observed. The increase of peptide concentration favored peptide aggregation that it was found to play a stabilizing role on the secondary structure of the peptide.

Further studies can be extended to study the mechanism of stabilization and formation in membrane mimicking environments (in the presence of trifluoroethanol) and at lipid bilayer interfaces.

As mentioned above, CA-MA hybrid peptide is a significant antibacterial agent and can be used against bacterial contaminations of materials. For this reason it is useful to understand the

interaction of this peptide with solid (apolar) surfaces that can mimic synthetic materials as polymer textile fibrils. For this reason, atomistic MD simulation studies have been performed to understand interactions of four CA-MA peptides with carbon based nanomaterials, such as CNT and graphene sheet. Adsorption of the peptide has been observed for both surfaces with preferential binding of the aromatic residues with the nanomaterial surfaces. It was also found that these interactions speed up the loss of α-helix structure in the peptides, compared to the previous simulation in pure aqueous solutions. The rate of the loss of α-helix structure has been shown to be slightly faster for the case of interaction with flat graphene surface rather than with CNT. In addition, the spontaneous diffusion inside the CNT has been observed for one of the peptides. This particular phenomenon will be interesting for further investigations using MD simulation at different level of scale on drug or other small molecule encapsulations inside nanotube as a model for drug delivery system in biological membrane. In addition, it would be interesting to study how the coated peptide can help to disperse the CNT bundles. Finally, it would be interesting as further work to analyze the difference in penetration kinetics of the peptide coated CNT from the bare CNT.

In conclusion, in this thesis we have studied for the first time and at different level of scale the structure and modus binding of different type of surfactants (ether-based polymers and peptides) in solution with carbon based nanomaterials. The comparison with experimental data has qualitatively validated the models and provided the detail at atomic level of the structure of these systems and the mechanism of binding and diffusion on lipid bilayers. The initial study of this thesis opens the possibility to use the same model for further extension to better understand the nature of these phenomena.

CURRICULUM VITAE

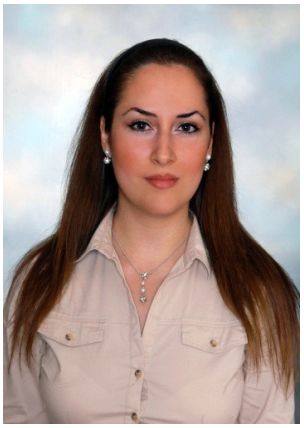

PERSONAL DETAILS

Name: ***Edita Sarukhanyan***

Date of Birth: 27th March, 1984

Nationality: Georgian

Language Skills: Russian, English, Armenian, Georgian and Italian

EDUCATION

11/2009 to date: Universiy of Salerno, Italy and Jacobs University Bremen, Germany

Ph.D student of Joint International Ph.D program with the major in *Computational Chemistry*

02/2007-02/2009: Tbilisi State University, Georgia

Master of Science in Physics with the major in *Applied Biophysics*

09/2001-06/2005: Tbilisi State University, Georgia

Bachelor of Science in Physics with the major in *Biopolymer Physics and Physical Basics of Medical Diagnostics*

PUBLICATIONS

1. ***Edita Sarukhanyan****, Antonio De Nicola, Danilo Roccatano, Toshihiro Kawakatsu, Giuseppe Milano.* Spontaneous Insertion of Carbon Nanotube Bundles Inside Biomembranes: A Hybrid Particle-Field Coarse-Grained Molecular Dynamics. **(manuscript under preparation)**

2. ***Edita Sarukhanyan****, Giuseppe Milano, Danilo Roccatano*. Atomistic Simulations of Cecropin A – Magainin 2 Hybrid Peptide in Water Solutions. **(manuscript under preparation)**

CURRICULUM VITAE

CONFERENCES AND PRESENTATIONS

1. **Edita Sarukhanyan**, Giuseppe Milano and Danilo Roccatano, "Atomistic Simulations of Carbon Nanotubes in Aqueous Mixtures of Surfactants", Poster Presentation, Molecular Life (MOLIFE) Center Jacobs University Bremen, **Bad Bavensen, Germany**, March 2013

2. **Edita Sarukhanyan**, Giuseppe Milano and Danilo Roccatano, "Atomistic Simulations of Carbon Nanotubes in Aqueous Mixtures of Surfactants", Poster Presentation, Treffen der Norddeutschen Biophysicker, **Borstel, Germany**, January 2013

3. **Edita Sarukhanyan**, Danilo Roccatano and Giuseppe Milano, "Coarse-Grain Simulation Studies of Spontaneous Insertion of Double-walled Carbon Nanotube Bundles Inside DPPC Lipid Bilayer", Oral Presentation, Workshop on research at interface between biomedicine and nanoscience, University of Salerno, **Salerno, Italy**, June 2012

4. **Edita Sarukhanyan**, Giuseppe Milano and Danilo Roccatano, "Atomistic Simulations of Carbon Nanotubes in Aqueous Mixtures of Surfactants", Poster Presentation, NanoFun Center and NanoMol Graduate Program Retreat, Jacobs University Bremen, **Germany,** May 2012

5. Attended the CCP5/CECAM "Methods in molecular Simulation Summer School 2010" at Queen's University Belfast, **Belfast, U.K,** July, 18^{th}-27^{th}

6. Attended the course *"Design of Biological Molecules"* by **Prof. Danilo Roccatano**, Jacobs University Bremen, **Bremen, Germany**, *September-November, 2012*

7. Attended the course *"Nanosciencs and Nanotechnology"* by **Prof. Maria Iavarone**, Oral Presentation on topic "Influence of the Preparation Conditions on PLGA Nanoparticles Thermal Stability" University of Salerno, **Salerno, Italy**, *November-December, 2009*